

# Direct Cooled Laminated Windings

## Radially Displaced Laminated Winding Segments



---

**Avo Reinap**

Division of Industrial Electrical Engineering and Automation  
Faculty of Engineering, Lund University

## Direct Cooled Laminated Windings

This is a summarizing report that collects the experiences on the development of electrical machines with direct air cooled laminated windings. This work, a part of project called Super Cool, is carried out with the support of Energimyndigheten and this support is gratefully acknowledged.

Shortly, Super Cool focuses on innovative directly air-cooled machine windings that allow making electrical machines either more powerful or compact. The reachable high power density and compactness are due to winding layout with superior thermal management that removes the excessive power losses directly from where they are generated. High peak current density ( $30 \text{ A/mm}^2$ ) and specific heating power ( $10 \text{ kW/dm}^3$ ) in the winding conductor can be balanced by forced air velocity ( $20\text{-}25 \text{ m/s}$ ) and the hot-spot temperature of the windings is kept under the temperature limits ( $150\text{-}180^\circ\text{C}$ ). The research bases on direct air-cooled laminated windings. Two different types of laminated windings: axial sections and angular segments are evaluated during the course of project. Practical evaluations have shown the limitations of thin ( $0.5\text{-}0.8 \text{ mm}$ ) lamination and thin cooling duct ( $0.3 \text{ mm}$ ) configuration where the machining and mounting tolerances practically closing out the forced cooling. On the contrary, wide lamination ( $1.5 \text{ mm}$ ) and wide cooling duct ( $1.0 \text{ mm}$ ) configuration causes unnecessarily huge deviation on conductor cross-sectional areas and available cooling areas that results easily overheated regions in the machine windings.

Writing this report is inspired by technical discussions and negotiations during the course of the design specification and realization from early 2015 to late 2015. Sincere gratitude is hereby expressed to all those who contributed to this work among them Mats Andersson, Ryszard Wierzbicki, Svante Bouvin, Kenneth Frogner, Fredrik Lundström, Mats Alaküla, Conny Högmark, Lennart Edström, Åke Nyström and some others who have not been listed above. Sincerely, thanks to the patience and immeasurable efforts by the team from division of production and material engineering there are a lot of practical experiences on defining manufacturable designs, finding rational production methods, producing and completing components, and not least the working prototype that is the main subject of this document.

## Content

Direct Cooled Laminated Windings.....	1
Content .....	2
1 Overview of winding layouts and machine designs.....	4
1.1 Hub motor with Axially Stacked Laminated Winding Sections .....	5
1.2 Traction machine with axially stacked laminated winding sections .....	5
1.3 Traction machine with angularly placed laminated winding segments.....	7
1.4 Outlines.....	8
2 Direct cooling .....	9
2.1 Thermal design .....	9
2.2 Flow characterization.....	10
2.3 Heat transfer coefficient.....	10
2.4 Pressure drop along the channels .....	11
2.5 Cooling power.....	12
2.6 Finite element analysis of conjugate heat transfer .....	12
2.7 Guidelines for machine design.....	14
3 Test machine .....	17
3.1 Machine design .....	17
3.2 Machine construction .....	21
3.3 Design for manufacturability.....	22
3.4 Practical limitations .....	24
4 Power losses in the stator.....	25
4.1 Magnetic power losses in the stator core.....	25
4.2 Induced losses in the winding due to the field rotation.....	31
4.3 Induced losses due to self induction .....	33
4.4 Other production specific power losses .....	34
5 Prototyping of a stator with laminated winding segments .....	37
5.1 Assembling chronology .....	37
5.2 Radially oriented laminated winding segments .....	38
5.3 Stator core segments .....	41
5.4 Assembling of stator segments .....	45
5.5 Assembling of stator .....	46
6 Prototyping diagnostics .....	49
6.1 Winding impedance.....	49
6.2 Insulation strength .....	53
6.3 Thermal load test.....	53
6.4 Mountability .....	57
6.5 Roto-pulse .....	57

7	Machine tests.....	59
7.1	Machine test set-up .....	59
7.2	No-load open circuit tests.....	60
7.3	On-load tests .....	61
7.4	Short-circuit tests.....	64
8	Summary .....	68
	References.....	69

# 1 Overview of winding layouts and machine designs

The starting point of the directly air-cooled laminated winding can be stated back to October 2010 with Conny Högmarks invention to use conducting sheets for cutting and forming high precision machine windings.

The research on directly air cooled laminated windings is initiated by the work that is presented by Conny Högmark in Coils, Windings, Insulation and Electrical Manufacturing Exhibitions and Conference (CWIEME) in Berlin 2012 [1]. The highlights of the article are the **manufacturing** methods, practical evaluation of **insulation**, and the **cooling** capability that the laminated wave-winding can provide.

Since 2012 a number of projects shared the ideas of directly air-cooled laminated windings and in return increased the competence on modeling, design, production and evaluation of electrical machines with these unconventional and innovative windings. Practically the originality of these types of windings is based on a diverse of manufacturing sequences where a conducting sheet of aluminum or copper is formed and shaped to a desired shape of the winding with predefined distance between the conductor strips or layers. This space between the conductors is very important as it is used for the coolant flow that instantly dissipates the heating power from where it is generated. The **laminated windings**, in this review, are taking advantage of constant strip thickness. They are based on a wave shaped conducting strip that is rolled up to a winding **section** (Figure 1.1 right) or folded and bended into a winding **segment** (Figure 1.1 left). The manufacturing process can take advantage of reordering the processes of folding, bending, cutting and so on.

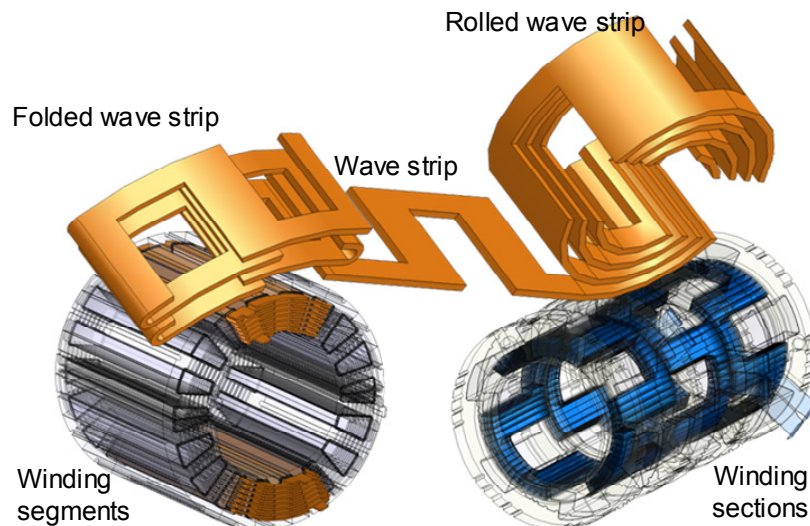


Figure 1.1 Formation of laminated windings from a wave-shaped conducting strip and the corresponding electrical machines with whole-length angular winding segments (left) and whole-perimeter axial winding sections (right).

A list of different target prototype is presented in Table 1.1 with the exception of RWD traction that ended with the calculation method and simulation results, all target machines are completed with working prototypes.

Table 1.1 Component reduction from the conventional gear unit in order to integrate the electrical machine into it

Target machine	Winding size	Material & Winding type	Arrangement
	Ri/Ro-H(He) [mm]		Np/Nt-thickness(space)
BAS	58/69-25(9)	Al and Cu sections	20/12-0.5(0.3)
Hub motor	66/79-28(3.5)	Al sections	22/17-0.5(0.3)
ExSAM traction	63/76-100(22)	Al sections	6/12-0.8(0.3)
RWD traction	70/92-46.6	Al sections	8/13-1.5(0.2)
Test machine	73.5/107.5-236(14)	Cu segments	16/14-1.5(1.0)

Parameters (Table 1.1) indicate inner and outer radius ( $R_o/R_i$ ) and total and end turn ( $H, H_e$ ) length of winding. The number of poles ( $N_p$ ) defines the winding, while number of turns ( $N_t$ ), thickness of conductor strip (**thickness**) and the space between the conductors (**space**) specifies the winding.

### 1.1 Hub motor with Axially Stacked Laminated Winding Sections

The hub motor is outcome of DAMIA-2 as a series of in-wheel motors. This 22-pole motor is a potential prototype machine where the angular laminated winding segments can be evaluated. One production example of this machine with axial laminated winding section is presented in Figure 1.2.

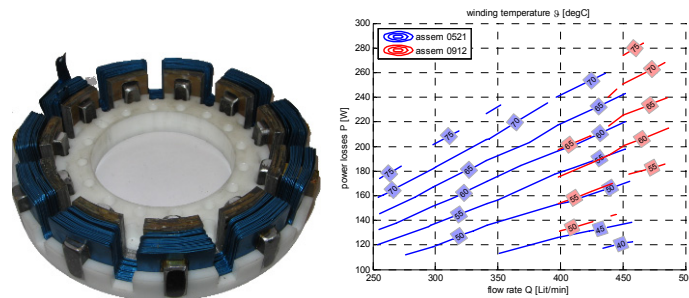


Figure 1.2 A open phase segment with anodized axial laminated winding segment and the experimental results from thermal loading.

The main conclusion from super cool project interest point of view is: the limitations of thin (0.5 mm) lamination and thin cooling duct (0.3 mm) configuration is limited by the machining and mounting tolerances that practically closing out the forced cooling and limit the thermal performance of directly air cooled laminated winding. Figure 1.2 shows two measurements after assembling of the same stator segment, which indicates the mounting challenges. The prototype underline the difficulty of maintaining the desired air gap between the conductor layers in the real world machine, as can be seen directly in the photo in Figure 1.2.

The size of the machine is considered to be suitable for experimental evaluation of winding models and arrangements. The starting point for model development is short-circuited copper-ring with variable parameters such as the thickness and the distance from the surface mounted magnets. The reference geometry of 22-pole and 2 magnets per pole rotor is shown in Figure 1.3. The air-gap flux density of 0.5 T is selected to define the current sheet instead of magnets (inner radius 84.9 mm and thickness 5 mm) and obtain the braking torque speed characteristics for different copper-ring parameters (Figure 1.3 right). The further specification of stator teeth and winding specification defines the exact layout.

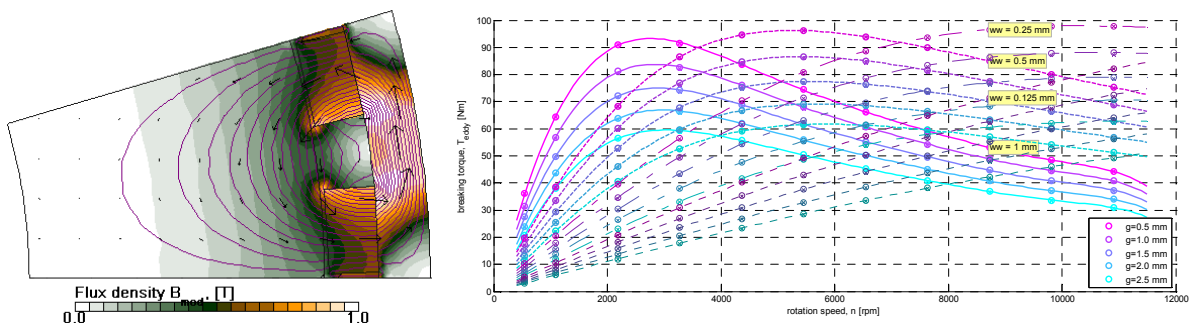


Figure 1.3 Half pole pair of hub rotor (left) and the braking torque speed characteristics for different copper-ring parameters (right).

### 1.2 Traction machine with axially stacked laminated winding sections

The manufacturing and evaluation experience of the machine prototype called ExSAM-3 (an intended 160 kW peak power traction machine with axially distributed windings) has shown the importance of an appropriate design of the insulation system, the relevance of the air guidance in the cooling system design including the supply and the analysis of the stator assembling process in the machine design stage.

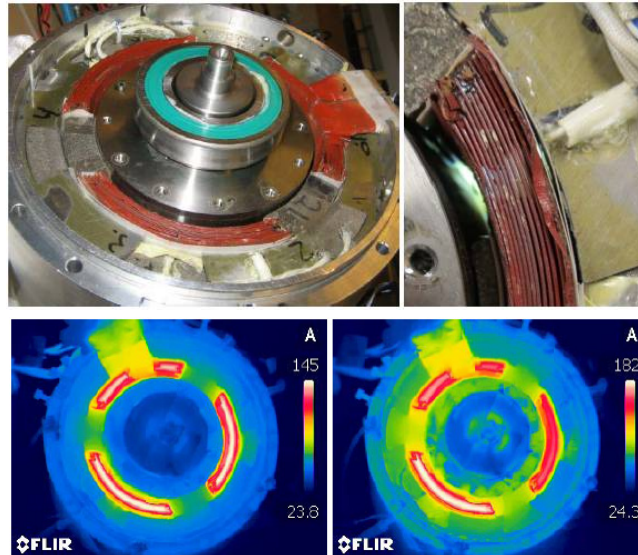


Figure 1.4 ExSAM-3 prototype. Above: Views of one axial end of one phase section. Below: Heat camera views of the same end with naturally cooled and force cooled machine

The results of the thermal analysis of the ExSAM-3 machine are presented in a paper at the Electric Drives Production Conference (EDPC) 2014. This paper [6] focuses on the issues related to direct air cooled laminated wave-winding and is carried out on a single phase section as a special prototype apart from the 3-phase machine.

The main conclusion from super cool project interest point of view is similar to previous machine: the tolerances of the thin (0.5 mm) lamination and thin cooling duct (0.3 mm) configuration is challenged by the machining and mounting tolerances that practically closing out the forced cooling and limit the thermal performance of directly air cooled laminated winding. Furthermore, high flow speed and high heat transfer is expected in the cooling ducts, this means that any change of flow distribution due flow leakage results the outcome of the actual cooling capability.

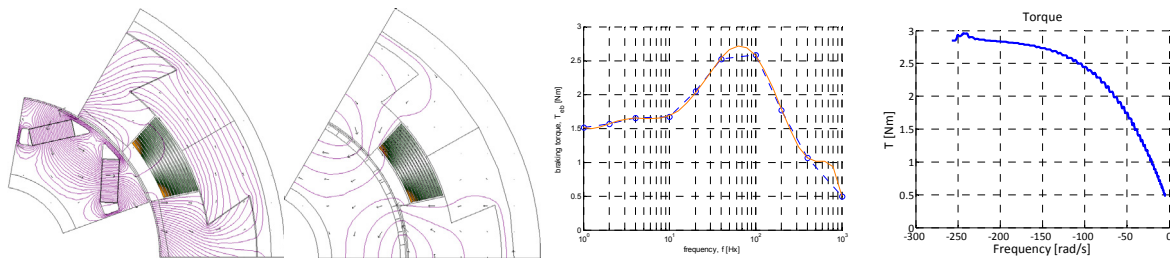


Figure 1.5 From the left; FE model with alternating magnets, FE model with rotating magnetic field (100Hz), calculated and measured torque speed characteristics for the idling machine.

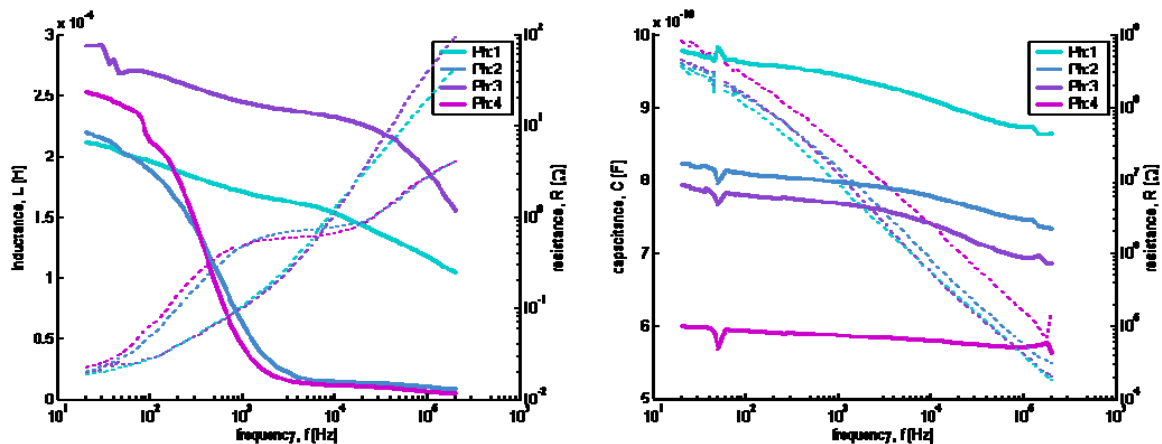


Figure 1.6 Differential mode RL impedance of the mounted machines (left) and common mode RC impedance (right)

The experimental work and post analysis on power losses and parameters of this machine are squeezed together in Figure 1.5 and Figure 1.6. First the 2D FE analysis of alternating magnets and rotating magnet fields are shown beside the predicted and measured torque speed characteristics for the idling machine. Second the impedances of the machine winding and winding to ground are presented. There is one complete three phase machine and another single phase unit (ph:4).

### 1.3 Traction machine with angularly placed laminated winding segments

The manufacturing and evaluation experience of the machine prototype called Test machine (an intended 60 kW peak power traction machine with angularly distributed windings) has shown the importance of an appropriate selection of production methods to accomplish the desired shape for the AC machine winding that influences the design of the insulation system and successful assembling process [8]. A complete set of machine windings is built and tested unless a half of the coils are used in the prototype machine (Figure 1.7) since the other half of the coils deviated too much from intended tolerances. A number of experiments are made to reinforce the cooling of the overheated sections of the winding segments at peak operation of 300A and 500L/min per segment.

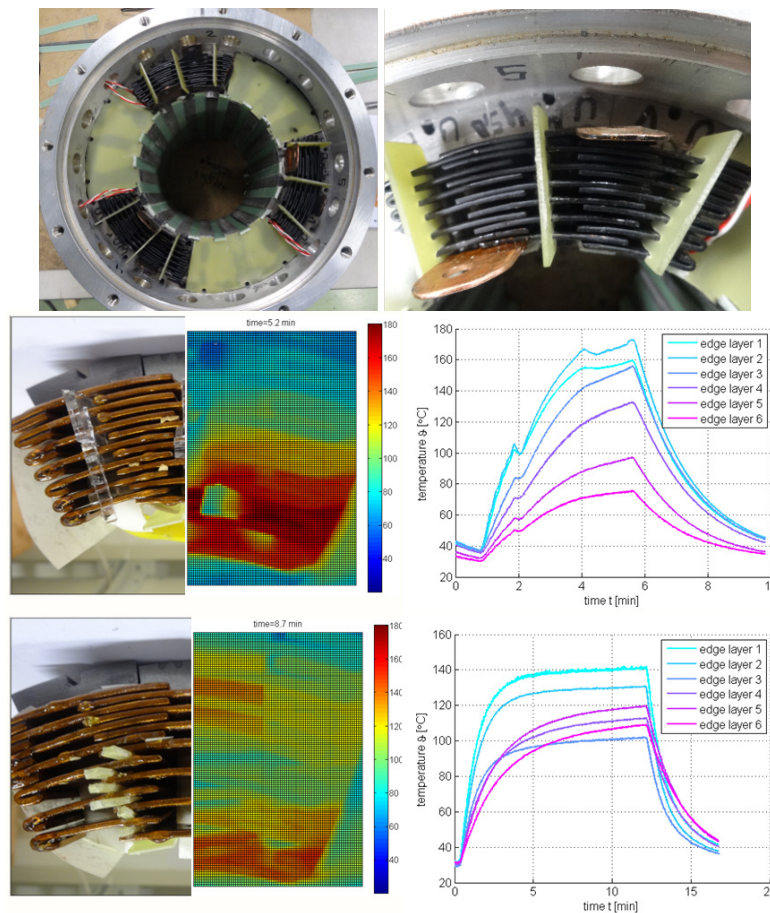


Figure 1.7 A views of the assembled machine and the experimental results from thermal loading

The results of different winding segment topologies, power losses, theoretical cooling capability and production of radially laminated winding segments are presented in a paper at the Electric drives production Conference (EDPC) 2015 [8].

The main conclusion from the Super cool project interest point of view is: the wide lamination (1.5 mm) and wide cooling duct (1.0 mm) configuration causes a remarkable deviation on conductor cross-sectional areas and available cooling areas that results easily overheated regions in the machine windings near the air gap. This is due to the outer layers having the lowest current density and the largest cooling area and the inner or near to gap layers having the highest current density and smallest cooling area. This limits the expected thermal performance of the machine. Furthermore the concern on proximity and eddy current losses causes further vulnerability of the thermally overloaded regions. In the lower part of Figure 1.7 the distribution of cooling duct thickness is intentionally made uneven resulting in a much better cooling behavior.



The experimental work and post analysis on power losses and parameters of this machine are presented in this document.

## 1.4 Outlines

In continuation the unconventional electrical machine with direct air cooled windings – radially oriented laminated winding segments are examined more in details. In general the benefits of the laminated windings are easy to produce and extreme thermal loading capability due to direct cooling. The machine design is basically relies on the benefits and replaces the windings of a conventional surface mounted permanent magnet synchronous machine that is used for traction application. The course of the work is summarized as following:

1. Core segmentation is used in order to assemble the windings and create a number of stator segments or modules – instead of single tooth concept a **modular teeth concept** is created
2. Initially the magnetic **core is improved** compared to reference machine – more magnetic core and less saturation for peak current operation. More exactly yoke is chosen to be wider and tooth width remains the same.
3. At first **radial laminated segments** is not specified as an easily realizable laminated winding but it is considered to maintain **high efficiency** due to lower internal AC losses over the operation frequency range compared to other winding arrangements.
4. The main design limitation is actually the incomplete exploration on production techniques and practical outcomes of produced winding segments – **manufacturability for design**.
5. The **production uncertainty** causes reservations for larger production tolerances. Moreover the tooth width is reduced 12-13% for unfailing winding production and in addition 5% reduction for successful assembling of the stator.
6. The imprecision and lack of experience are related to **folding and bending processes** involved in the winding production. This result 100% increase of the angular space between the winding segments.
7. **Prototyping diagnostics** is introduced in order to validate the manufactured or assembled products in relation to component functionality and reliability. A series of E, M and H-tests are used for validation during component finalization and machine assembling.
8. The stator is built and machine is **experimentally validated**. The assembled machine compromises the manufacturability speed to completeness or perfectness – half of the winding segments are used and 9-14% air leakage is allowed through the air-gap
9. The practical evaluation and post analysis has created a lot of **results** that are presented and discussed in different sections rather than collected into a single chapter.

A number of topologies for a single phase axially stacked laminated winding section are presented in [2] and the design for different machines is presented in [3] and [5]. The design and prototyping of an angularly displaced laminated winding segment is presented in [8] and the manufacturing and evaluation of a complete machine is the main subject to this document. The experience in [1] axial winding section is used to generate single phase topologies, 2D and 3D FEA for electromagnetics, practical evaluation of machine elements and compare designs [2]. The practical experience on design of the three phase traction machine (ExSAM-3) is presented in [3] and prototyping and thermal performance in [6]. Most of the design and prototyping experience is used as an input for selecting proper analysis models for design and finding suitable approaches for manufacturing. An exhaustive analysis on analytic/empiric heat transfer models and modeling results are presented in [4]. The development of these models and connection into 3D-FE models are presented in [7][6] and further developed in this document when comparing empiric results to the simple CFD models. This document provides more outputs on FEA based power loss modeling of laminated windings that are extended from slots [8] to stator segments and complete machine including alternating and rotating field effects. For the sake of calculation speed and accuracy, these models are built in 2D and not in 3D. This document presents the outcomes extended power loss modeling in the stator core.

## 2 Direct cooling

The heating power for the windings is associated with Joule losses where the replacement of current  $I$  [A] with current density  $J$  [A/mm<sup>2</sup>] and resistance  $R$  [Ω] with resistivity  $\rho$  [Ωm] gives specific heating power  $p$  [W/m<sup>3</sup>] in an electric conductor that cross-sectional area is  $A_{ec}$  [m<sup>2</sup>] and total length is  $l_{ec}$  [m].

$$P_{cond} = I^2 R(\vartheta) = (JA)^2 \rho(\vartheta) \cdot \frac{l}{A} = J^2 \rho(\vartheta) V_{cond} \rightarrow p_{cond} = J^2 \rho(\vartheta) \quad 2.1$$

The cooling power is connected to advection: fluid transport and its specific heat capacity. By considering a cooling channel that cross-sectional area is  $A_{cc}$  [m<sup>2</sup>] and total length is  $l_{cc}$  [m] then the flow rate  $Q$  [m<sup>3</sup>/s] can be replaced by flow speed  $v$  [m/s] in order to define the specific cooling power over the length of the channel when the temperature difference across the channel is  $\Delta\vartheta$  [K] and the fluid is characterized by density  $\rho$  [kg/m<sup>3</sup>] and heat capacity  $c_p$  [J/kgK].

$$P_{cool} = Q \rho c_p \Delta\vartheta = \frac{v}{A_{cc}} \rho c_p \Delta\vartheta \rightarrow p_{cool} = \frac{1}{l_{cc}} v \rho c_p \Delta\vartheta \quad 2.2$$

The heating and cooling is related to (current) flow density and (coolant) flow intensity. Usually the electric current flow along the winding conductor is in series and coolant flow through the winding channels is parallel. Therefore an additional circuit modeling is needed to define the flow in a number of parallel cooling channels or ducts. Electric conductivity specifies heating power of the winding for a given current and heat capacity defines the cooling power for a selected flow rate. As an outcome the thermal conditions along the cooling channel and across the channel is driving the thermal design and geometrical layout of the winding.

### 2.1 Thermal design

The thermal design, topology selection and winding dimensioning is based on theory on forced convection cooling in a parallel-plate channels and non-circular cooling ducts. For the case of simplicity first the outlet and inlet temperatures are selected. The rational choice of the flow rate determines not only the cooling power but also the heat transfer coefficient from the wall to fluid and the temperature drop across the boundary layer and the pressure drop along the channel. Therefore the selection of the flow speed  $v$  [m/s] and the height of the channels  $d$  [mm] establish the important link between heat transfer and fluid dynamics that is used in the thermal design. There are two important charts, which are derived on basis of empiric equations and correlation functions

1. heat transfer coefficient as a function of channel height and flow speed  $h=f(d,v)$
2. pressure drop per length of unit as a function of channel height and flow speed  $p=f(d,v)$

The selection of inlet  $\vartheta_{in}$  and outlet  $\vartheta_{out}$  temperatures are driven by the hot spot temperature limit for the winding  $\vartheta_{win}$ . The dimensions for the height of the cooling channel and the thickness of the conductor is selected according to the rational and realizable choice of geometry, coolant fluid and fluid dynamics. Figure 2.1 visualizes a half height of duct and a half thickness of the conductor, dimensions, flow development and coolant capacity to dissipate heat (on the right figure).

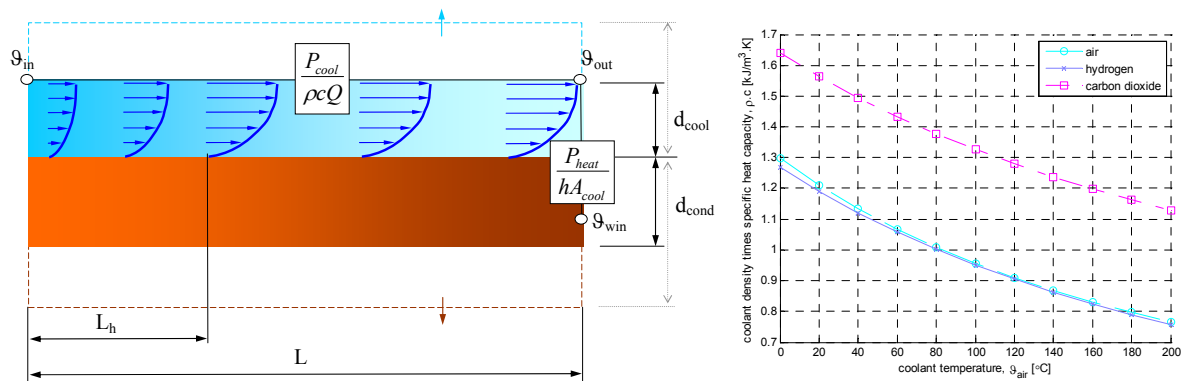


Figure 2.1 Schematic presentation of half channel and conductor with entrance region  $L_h$  and full length  $L$ . The schematics include the thermal node points and the definition of the thermal conductance in between. Figure on the right shows the product of specific heat capacity and density for 3 different gas coolants as a function of coolant temperatures.

Calculation methods [9][10] are used to determine flow and characterize heat transfer at constant heat flux conditions and pressure drop. The limitations are the flow determination – laminar, and geometry interpretation – smooth surfaces and cooling ducts are rather narrow and wide (parallel plates) than rectangular or curvilinear. Specification of cooling media compared to air is shown in Table 2.1.

Table 2.1 Specification of cooling medium

Coolant	Air		Hydrogen		Carbon dioxide		Water		Transformer oil	
	20	120	20	120	20	120	20	120	20	120
Temperature, °C	20	120	20	120	20	120	20	120	20	120
Specific heat capacity, kJ/kgK	1.005	1.014	14.20	14.49	0.854	0.938	4.187	4.250	1.710	2.114
Mass density, kg/m <sup>3</sup>	1.204	0.898	0.084	0.063	1.830	1.364	999.6	946.2	879.1	816.5
Thermal conductivity, W/mK	0.026	0.033	0.178	0.227	0.016	0.024	0.594	0.686	0.111	0.102
Dynamic viscosity, Pa·s	1.8e-5	2.3e-5	0.8e-5	1.1e-5	1.4e-5	1.9e-5	1e-3	0.2e-3	0.052	

The following calculations are specified for 70°C air ( $\vartheta_{in}=20^\circ\text{C}$  and  $\vartheta_{out}=120^\circ\text{C}$ ) where mass density is 1.0335 kg/m<sup>3</sup> and specific heat capacity 1.0095 kJ/kgK.

## 2.2 Flow characterization

The flow characterization in the cooling channel is defined by flow development, entrance length, boundary layer and so on that influence the main parameters such as heat transfer and pressure drop in the cooling channel. Flow development can be characterized as laminar, unstable or transitional or turbulent. Reynolds number,  $Re = \text{ratio} = \text{inertia force} / \text{viscous force}$ , characterizes the flow and Mach number illustrates the compressibility of the flow. Figure 2.2 shows the flow rate for the selected input parameters such as the channel height  $d$  and the velocity in the channel  $v$ . This figure demonstrates also Reynolds number for the same input (Figure 2.2 right).  $Re = 2300$  is often used as a value where the character of laminar flow is changed to turbulence flow and this experimental value is based on research on circular smooth tubes. For sake of machine design it is stated that the wide region of interest can be governed with the analytic and empiric equations that is derived (only) for the laminar flow.

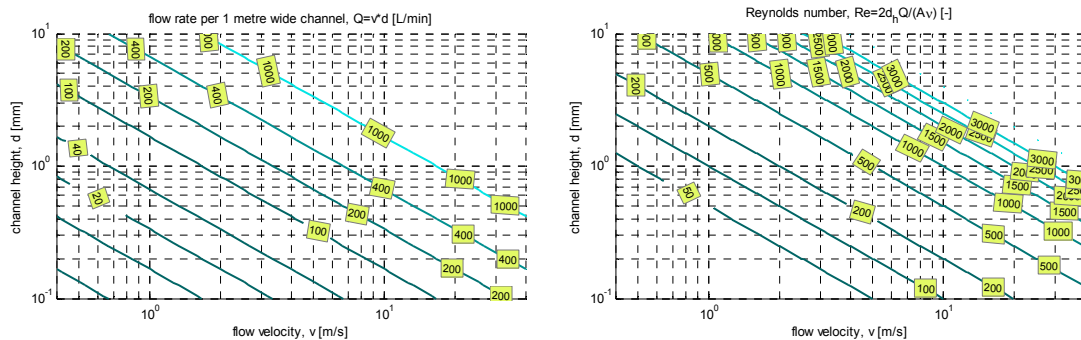


Figure 2.2 Flow rate and Reynolds number as a function of cooling channel width and flow velocity.

## 2.3 Heat transfer coefficient

The character of flow is described by Reynolds number, the ability to transfer the heat by Nusselt number and the coolant is described by Prandtl number. The hydraulic diameter is related to the geometric layout of the cooling channel and this is taken twice of the distance between the parallel plates. Nusselt number characterizes the ratio of convective to conductive heat transfer from the wall to the fluid. This number is calculated from semi-empirical correlation of a simple geometry that considers the thermally developing and hydrodynamically developed laminar flow

$$Nu = \begin{cases} 2.7646\xi^{\frac{1}{3}} & \text{if } \xi < 0.03 \\ 6.49 + 0.0722\xi^{-1} & \text{if } \xi \geq 0.03 \end{cases} \quad 2.3$$

The thermal entrance region is characterized by the following dimensionless distance

$$\xi = \frac{x}{D_h \text{RePr}} \quad 2.4$$

The results (Figure 2.3) are presented only for the laminar flow even character of the flow should change according to Reynolds number ( $Re > 2300$ ). As a reference, Nusselt number for a fully developed flow between the parallel plates at constant heat flux conditions on the walls is 8.235. The heat transfer coefficient is calculated from the averaged Nusselt number (2.3) and presented in Figure 2.4. As the entrance length due to fluid development (2.4) influences the heat transfer in the entrance region, there are two contour maps shown for 1 meter and 0.1 meter long channel. As a final point, the heat transfer coefficient is used to estimate the temperature drop across the wall boundary, which is from the wall to the fluid for the amount of cooling power.

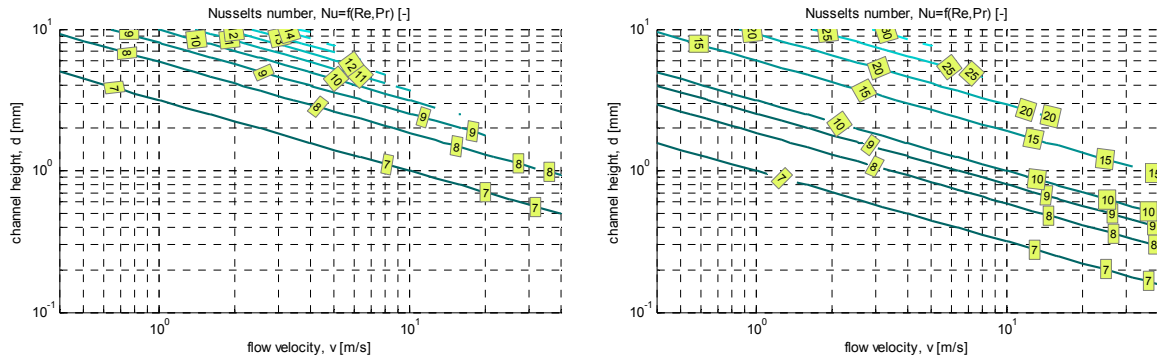


Figure 2.3 Nusselt number as a function of flow rate and cooling channel height for 1 meter (left) and 0.1 meter (right) long channel

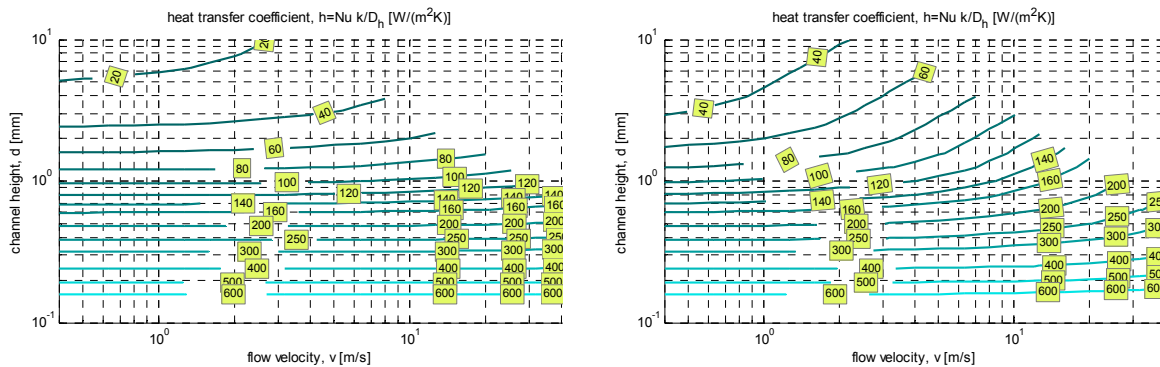


Figure 2.4 Convection as a function of flow rate and cooling channel height for 1 meter (left) and 0.1 meter (right) long channel

### 2.4 Pressure drop along the channels

The pressure drop along 1 meter long cooling duct is shown in Figure 2.5. Thus 0.1 m channel has 10% of the pressure drop. The pressure drop is defined by Darcy friction factor, the channel height  $d$  and the velocity in the channel  $v$ . The solution of Navier-Stokes equation describes the developed flow between the parallel plates

$$u(y) = \frac{1}{2\mu} \frac{dp}{dx} (y^2 - h^2) \tag{2.5}$$

The pressure drop of a fully developed flow is found from the equilibrium between pressure forces and friction forces that over the length of the channel becomes

$$\Delta P = f \frac{L}{h} \frac{\rho U^2}{2} \tag{2.6}$$

Where the friction factor a very wide rectangular cooling duct is

$$f = \frac{96}{Re} \tag{2.7}$$

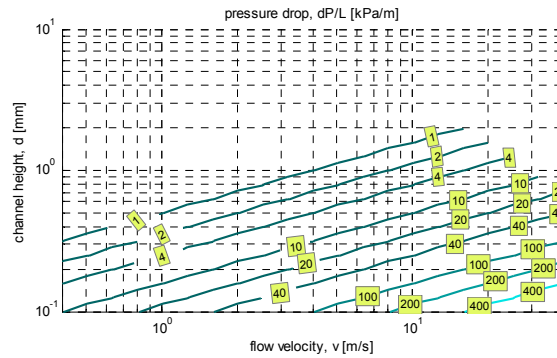


Figure 2.5 Pressure drop as a function of flow rate and cooling channel height

## 2.5 Cooling power

Two aspects of the cooling power are shown in Figure 2.6: the ability to dissipate heating power for preselected temperature difference and the power consumption to transport the air through the cooling ducts. The power requirement to dissipate heating power is shown as a function of cooling channel height  $d$  and air flow velocity  $v$ .

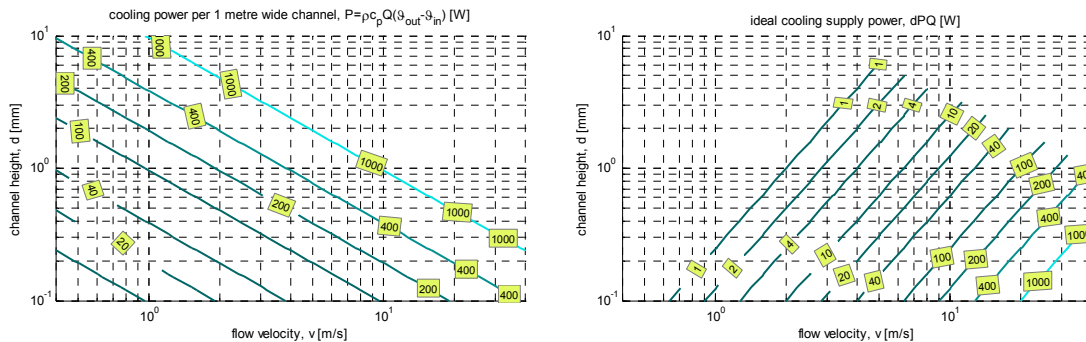


Figure 2.6 Ability to dissipate heat (left) applied power to dissipate the heat (right)

These two graphs are used to determine the cooling efficiency: the ratio of the applied power to the dissipated power.

## 2.6 Finite element analysis of conjugate heat transfer

2D FE models is used in parallel and as a continuation to empiric models and correlation functions in order to deepen the fluid dynamics and heat transfer analysis towards to the distribution of heating sources and cooling sinks and extend it further to 3D FE. Comsol multiphysics laminar flow model for conjugate heat transfer is used in 2D FEA with simpler geometry. The connected mathematic models for multiphysics is simplified or divided between two different fields: CFD in cooling ducts and FEA heat sources and heat transfer in solids with appropriate boundary conditions.

An overview chart of diverse directly air-cooled laminated windings, which are the main subject on super cool project, is shown in Figure 2.7. This image shows the situation for four different lengths of cooling channels where the width between the current conducting laminates is gradually increased in order to control the temperature increase for the same cooling intensity. The thermal operation point is selected according to peak power loss density of  $8 \text{ W/cm}^3$  ( $= 20 \text{ A/mm}^2 \text{ rms @ } 20 \text{ n}\Omega\text{m}$  or  $14.14 \text{ A/mm}^2 \text{ rms @ } 40 \text{ n}\Omega\text{m}$ ) and the average speed of the air-flow is  $12 \text{ m/s}$ . The cooling conditions allows rather similar pressure drop along the channel ( $200 \text{ Pa}$  per contour line). At the same time the cooling density in  $\text{W/cm}^3$  decreases with the wider channel and fill factor of the winding is getting poorer.

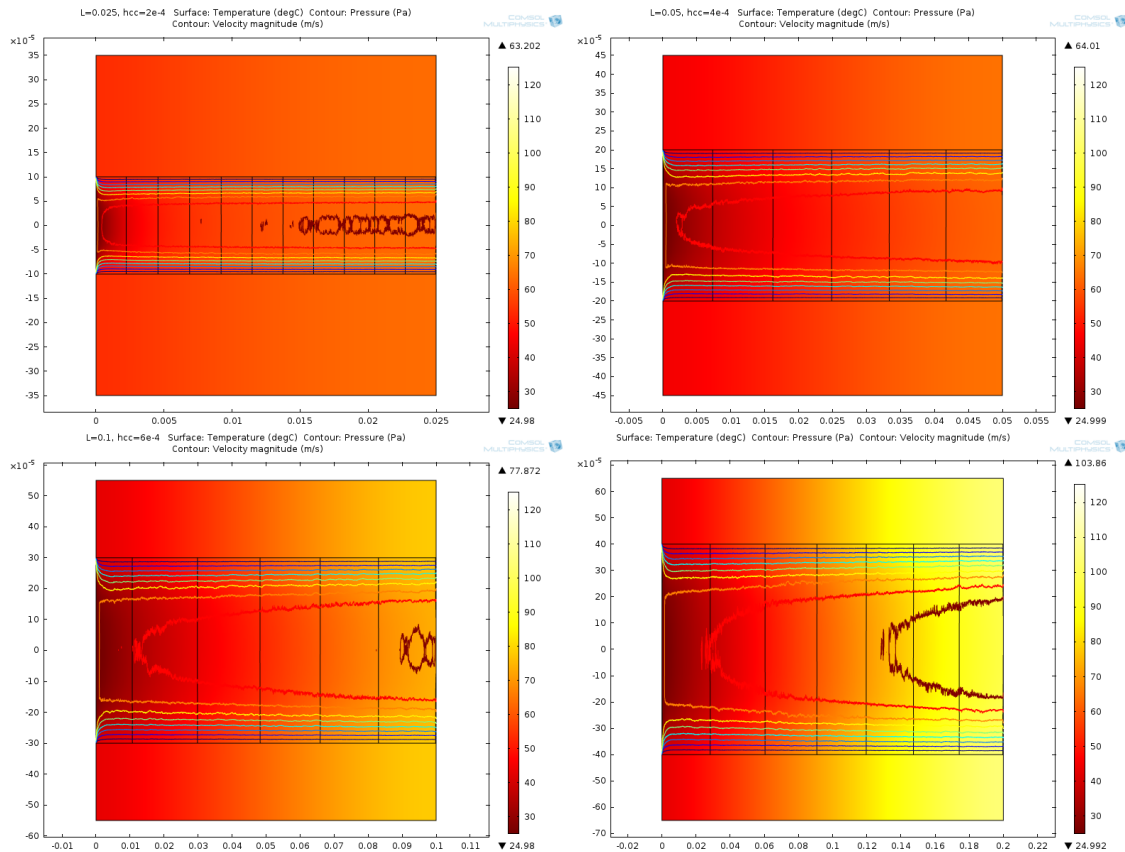


Figure 2.7 Temperature distribution in a direct air-cooled system with cooling channel in the middle and heating strips – half thickness, below and above. Cooling channel dimensions: 1) up-left 25 mm long 0.2 wide, 2) up-right 50 mm long 0.4 wide, 2) down-left 100 mm long 0.6 wide, 2) up-right 200 mm long 0.8 wide.

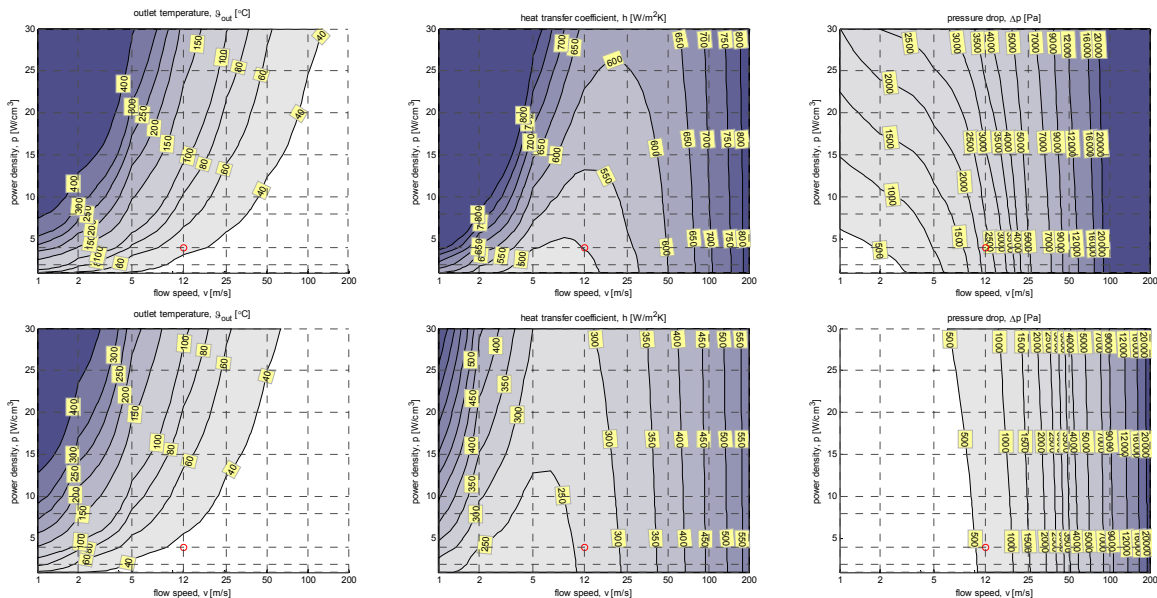


Figure 2.8 Outlet temperature (left), heat transfer coefficient (middle) and pressure drop (right) for 0.2 mm channel (top row) and 0.4 mm channel (bottom row)

Figure 2.8 demonstrates the typical output graphs from the conjugate heat transfer finite element analysis. Geometrically the 2D FE model is oversimplified. There are no entrance or outlet regions rather than just a full length channel with suitable boundary conditions such as inlet flow and temperature, no-slip and outlet pressure. The coolant is described as incompressible non isothermal flow, where the properties such as density are affected by temperatures. The volumetric discretisation with finite element limits the suitability to calculate more complex turbulent flows. Therefore laminar flows are the initial focus with tetrahedral mesh. FE or more specific CFD determines the need for a suitable numeric analysis tool,

ability to describe physical phenomenon, express appropriate equations, and finally provide discretisation for numeric field analysis. Over simplified models are suitable for design in order to grasp quickly the correct design directions.

## 2.7 Guidelines for machine design

The main goal for the machine design is to evaluate conceivable ideas, realizable production steps and product layout proposals and provide functional and manufacturable product – an electric machine. The design can be partly optimal but it should prevent overvaluation and oversight – a mistake resulting from inattention.

Figure 2.9 shows a design flow chart for evaluation and development of ideas, which is continued with component or a constructional element and product development. The starting loop is a **drafting** that basically evaluates how a component in an electric machine such as a direct cooled winding is to be constructed and how this contributes to the energy conversion i.e. if the component is **functional** and **rational**. This evaluation loop requires topology generation as an input and leads to the visible solutions. This is not just dimensionless sketching as it determines the first layout for the stator (or rotor) slot or tooth. This layout is a groundwork for functionality evaluation, which is based on a set of analytic models, empiric expressions or/and experience. This layout is also the starting point for construction study where the manufacturers experience is used to validate the practical realization and assembling possibilities for the component(s).

The second loop contains practically a number of sub optimization loops where the best materials and dimensions for the drafting layout are chosen for the **improved functionality** and more rational **manufacturability**. The importance of these calculation loops (of a number of simplified 2D finite element (FE) models) is to determine not only the strengths but also weaknesses of concepts and topologies. The simplicity of the 2D FE models is achieved by

- the reduced geometric size: a slot, a cooling channel etc
- simpler formulation of physical problems like incompressible isothermal laminar flow
- Minimal amount of finite elements or definition of surface impedances for high frequency models
- Reduced and rational definition on material dependencies and connected fields

The attractive outcome from the geometric modeling is used as the foundation on the early estimation on machine performance and manufacturability analysis. The performance estimation is basically the completion of the C-coals such as characterization of the concepts and topologies. There is no additional flow chart for production analysis and that is why the selection of an optimal layout or promising concept is considered subjective here.

The visible solutions with promising characteristics become as inputs to 3D structure modeling. In this case the 3D structure is either defined in CAD software with the production orientation or in FE software with simpler control for field computation. The later is for the sake of meshing and obtaining quick and valuable results. The structure modeling focuses basically only on a single component in a system and studies different types of loads. The focus in this chart lies only on resistive heating and direct cooling of the laminated windings.

In continuation the assembling of the stator and whole machine gains importance. There is CAD for prototyping in parallel to performance evaluation models. The calculation models can be rather general 3D FE to analyze the outcomes of integration or rather specific with the focus on special issues relating to assembling and tolerances.

The primary design goal is an evaluation and a comparison between different topologies for direct cooled windings. The secondary goals are related to the specifications for the electric machine with the selected type of winding. As a matter of fact the upper half of the design process, which is shown in Figure 2.9, is reported in [8]. The results from the 2D geometric and 3D structure modeling visualize the possibilities for the functionality and manufacturability in the machine design.

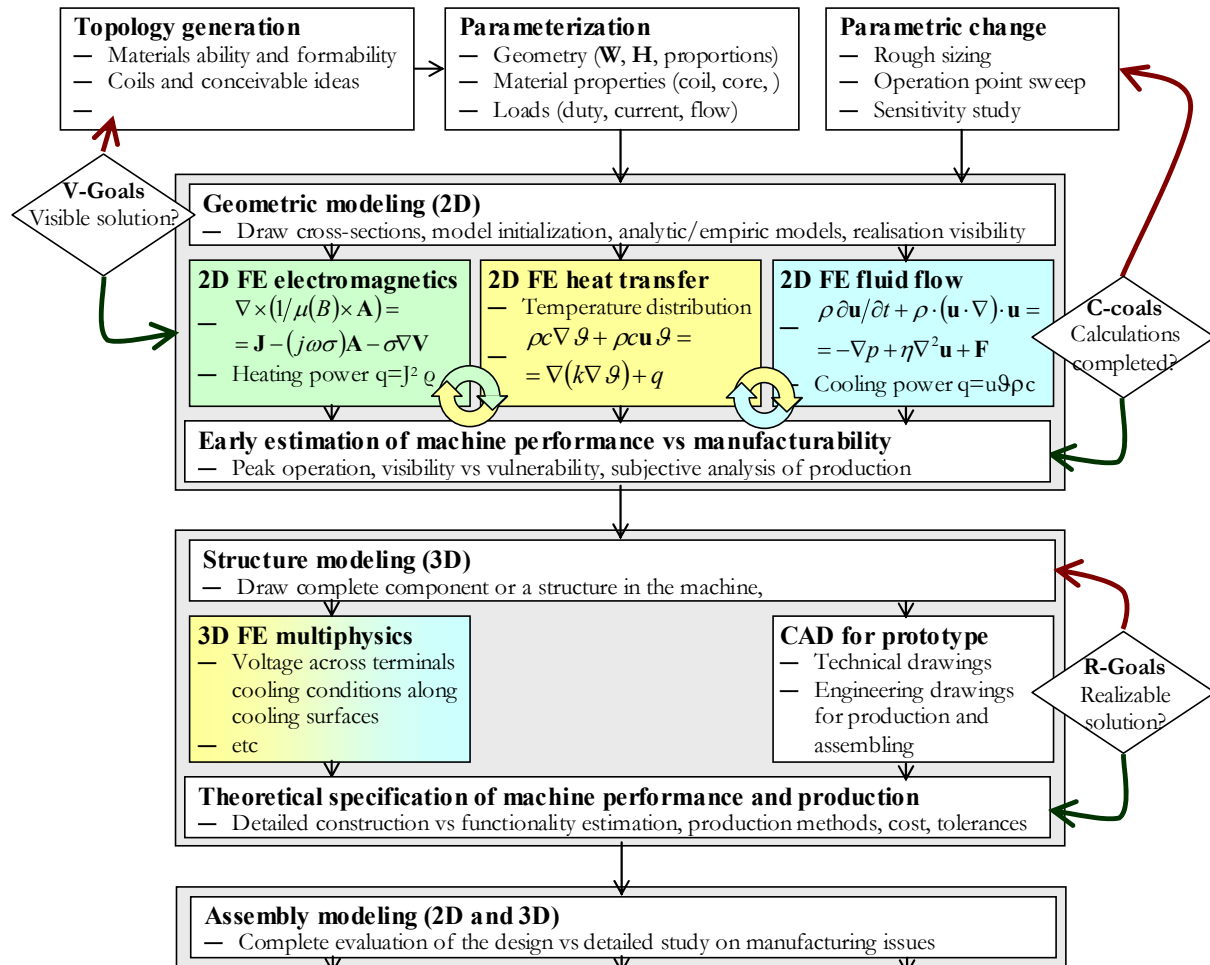


Figure 2.9 Design flow chart for evaluation and development of ideas continued with product development

Figure 2.10 shows the geometrical input of the cross-section on the directly cooled windings for 22-pole hub motor (1.1), 6-pole traction machine (1.2) and 16-pole traction machine (1.3). The color code shows the power loss difference for each circular layer or turn of the laminated winding. Table 2.2 demonstrates some winding data of the different machines and their different configurations. The axial length of the prototype machines and their potential alternatives is nearly 25, 50, 100, 200, which is the doubled length of the previous. The axial length of the prototype machines and their potential alternatives is nearly 25, 50, 100, 200, which is the doubled length of the previous (Figure 2.7).

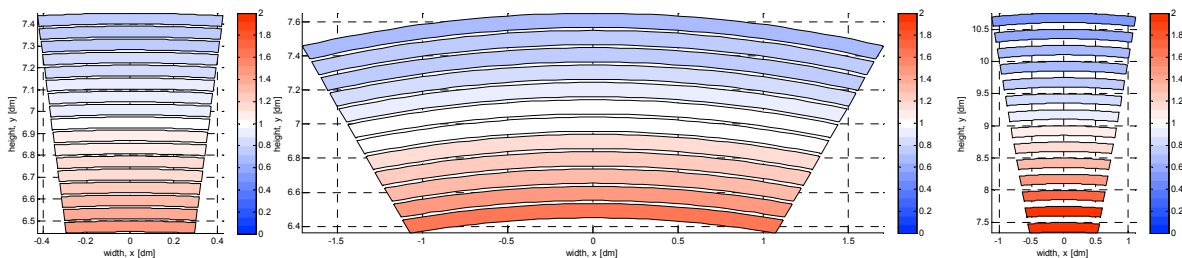


Figure 2.10 Relative conductor cross-section area in power of two specifies the largest difference of 1.38, 1.47 and 1.80. This number shows about how many times the power losses in the winding radially innermost becomes higher compared to the average cross-sectional area.

Table 2.2 Specification of prototype machines and their alternatives

Machine	Hub motor		Traction IPMSM		Traction SPMSM	
Number of slots-poles	22-22	24-22	6-6	12-6	18-16	15-16
Thickness of conductor/height of duct, mm	0.5/0.3	0.5/0.3	0.5/0.3	0.5/0.3	1.5/1.0	1.5/1.0
Axial length, mm	28	50	100	100	236	236
Inlet area per slot, mm <sup>2</sup>	14.4	11.6	55.6	27.2	222.7	308.6
Inlet area difference per slot, max/min	1.35	1.40	1.49	1.49	1.94	1.77



The same number of turns is used for the alternative designs of the prototyped machines (Table 2.2 Figure 2.10). Fill factor of insulated slot is theoretically  $0.5/(0.5+0.3)=62.5\%$  and  $1.5/(1.5+1.0)=60\%$ . The layout in Figure 2.10 is the initial point for the further analysis of distribution of heating sources vs cooling sinks, estimation of actual flow distribution and rough pneumatic impedance network.

### 3 Test machine

The test machine is inspired by an existing machine with **modular** distributed concentrated **windings**. The new machine takes advantages of existing rotor and magnetic design. Intentionally a dissimilar rotor construction is shown in this document. Basically the goal for the machine design is to specify the new type of windings - **directly air-cooled** laminated fractional pitch windings and assembling this type of windings. As this single piece winding cannot be mounted into the core the core needs to be mounted into the winding. Conventionally the magnetic core is used to accommodate the main insulations and windings. At this time the construction is exactly in opposite as the **winding slots** are used to hold the main insulation and the pieces of the magnetic core. The **core segments**, which consist of single tooth and half of a yoke in both direction, is entered into the winding slot that contains the insulation liner. Ideally the edges of yoke align and arcs of the segment yokes build up a perfect circle. Figure 3.1 on the left shows a few different realizable layouts for stator modules. The specific concerns with these arrangements are the rational manufacturing of components, assembling, functionality and reliability.

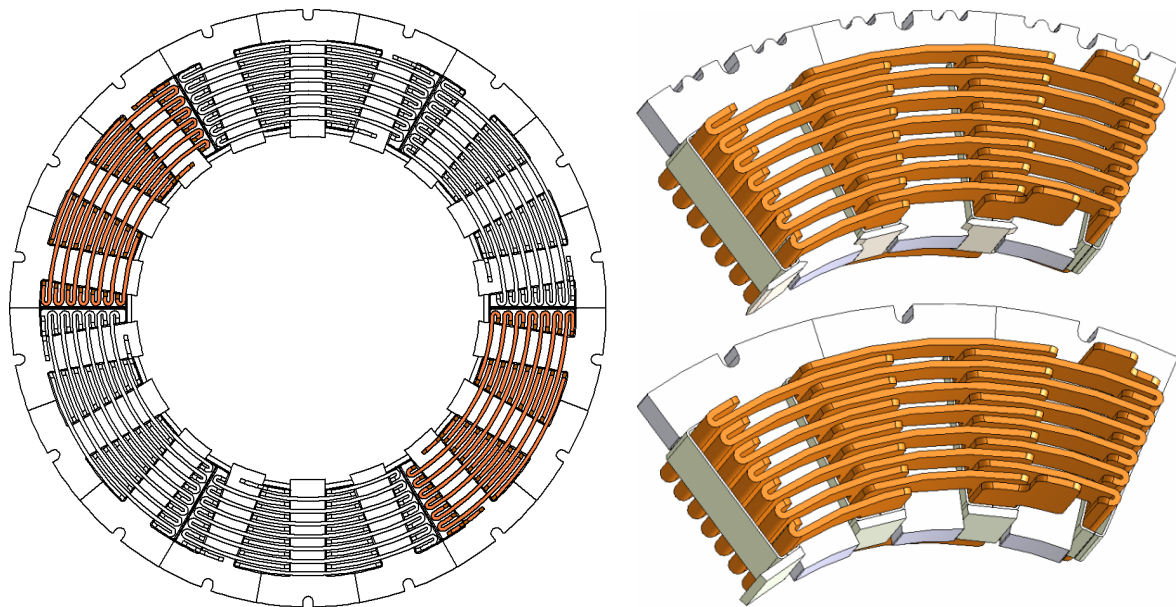


Figure 3.1 Stator consisting of 6 stator segments where phase winding is built up of two consequent modules (left). The stator segment consists of one winding segments and 3 core segments (right). There can be a number of solutions for assembling but here are shown two versions: welded core segments with a groove for slot locker (right up) or clued core with a tight slot wedge (right down)

#### 3.1 Machine design

This section does not consider either the exhaustive design process, which is presented in Figure 2.9, or the complete outcomes of analyses, syntheses, optimization with fine discussion and argumentation. Moreover this section does not carry any discussion on laminated winding types and layouts for modular segments as the comparison of radially displaced laminated windings to laterally displaced windings is already documented in [8]. What this section presents is the **peak operation** for an ideal expected geometry of the stator with perfect thermal connection between the solids and ideal forced cooling conditions on the internal surfaces of the laminated winding. The modeled outcomes focus on

- Peak current: **300 A rms**, **424 A peak**
- Speed above the nominal: **1500 rpm** that defines frequency **200 Hz** and core power loss density **0.12-0.2 kW/dm<sup>3</sup>** if the expected flux density peak is **1.6 T**
- Conductor power loss density is calculated for DC current (density) and conductor resistivity of **24.5nΩm**
- Forced cooling of the laminated winding is defined **160 W/m<sup>2</sup>K** and referred to **1 mm** channel with the average speed between **15-25 m/s**. Heat transfer coefficient **100 W/m<sup>2</sup>K** is shown for comparison.

- Outlet temperature is selected to be  $120^{\circ}\text{C}$  and this selection basically defines the flow rate for the given inlet temperature of coolant and the heating power that has to be dissipated.
- As the machine has power losses in the stator core and in the windings it has also additional cooling in the air-gap that is defined  $20\text{ W/m}^2\text{K}$  @  $100^{\circ}\text{C}$  and natural cooling from the radial surface of the stator housing  $10\text{ W/m}^2\text{K}$  @  $40^{\circ}\text{C}$

Peak current density is shown at right lower coil in left Figure 3.2 and rms value next to it. Regions with **considerable heat sources** are easy to distinguish due to high value of current density. Figure 3.3 shows the magnetic flux density for the peak (left) and nominal (right) operation when only the (excitation) torque producing current component is applied. Figure 3.4 shows the flux density distribution at short circuit condition when the demagnetizing current is applied (left) and the magnetic loading at no-load condition.

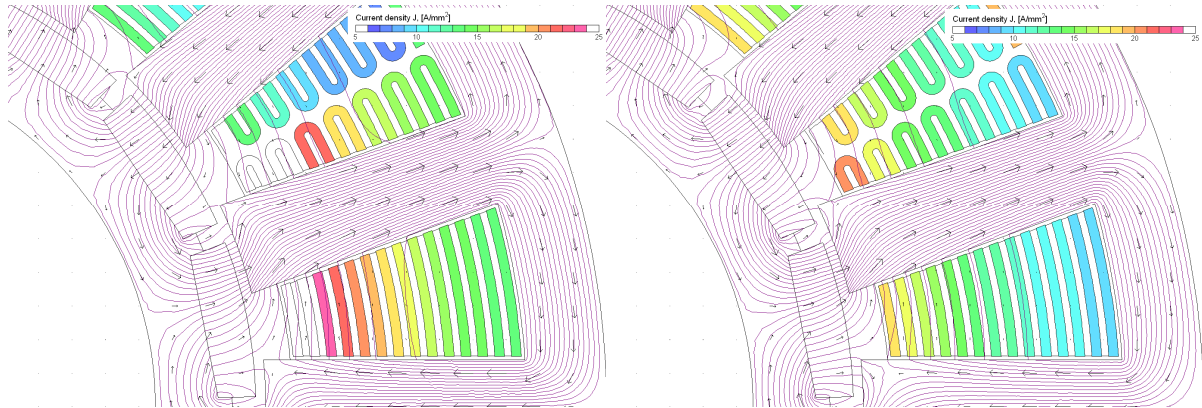


Figure 3.2 Current density distribution at peak load of 300 Arms as a instantaneous values including the peak values (left) and effective values over the period excluding the proximity and eddy current effects (right)

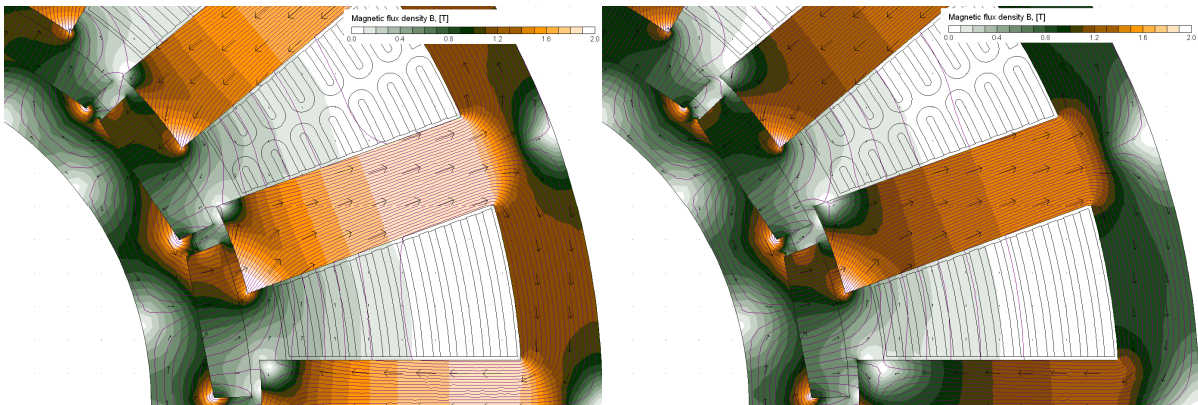


Figure 3.3 Flux density distribution at peak load of 300 Arms (left) and at 150 Arms (right)

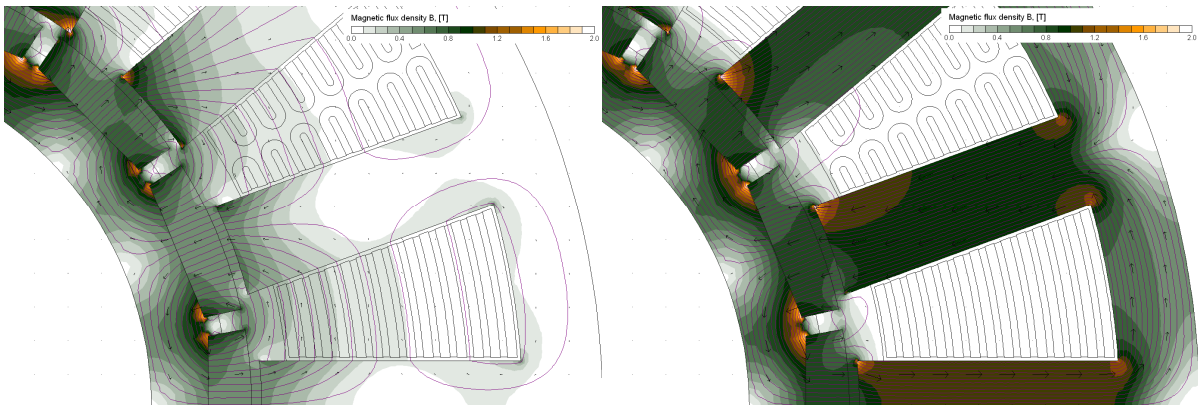


Figure 3.4 Flux density distribution at short circuit point with demagnetizing current of 150 Arms (left) and at no-load (right)

The current density peak value and the specific heat source without considering the AC losses are:

- regular winding layer closest to the air-gap  $18.9\text{A}/\text{mm}^2$  and  $8.8\text{W}/\text{cm}^3$
- edge winding layer closest to the air-gap  $20.1\text{A}/\text{mm}^2$  and  $9.9\text{W}/\text{cm}^3$
- terminal winding layer closest to the stator yoke  $19.7\text{A}/\text{mm}^2$  and  $9.5\text{W}/\text{cm}^3$

Figure 3.5 shows the **temperature distribution** at peak operation for two different heat transfer coefficient and at the same outlet temperature. Figure 3.6 demonstrates the **heat flows** through the structure from the volumetric heat sources to the **available cooling** surfaces. This 2D image does not include any direct thermal conduction path between the winding layers via the end turns. Therefore heat flows from the heated regions to the cooled regions are clearly visible.

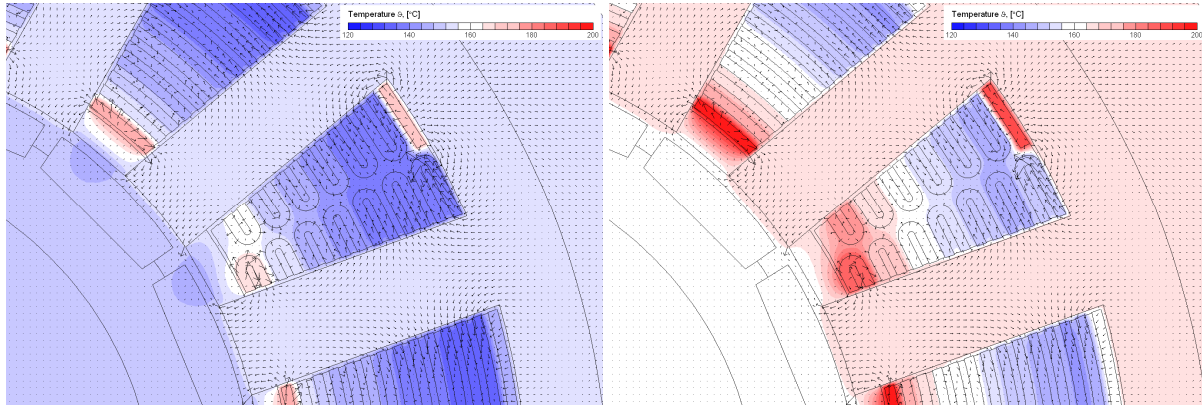


Figure 3.5 Temperature distribution at  $160\text{ W}/\text{m}^2\text{K}$  (left) and  $100\text{ W}/\text{m}^2\text{K}$  (right) forced convection on all cooling surfaces in the outlet side when outlet temperature is  $120^\circ\text{C}$

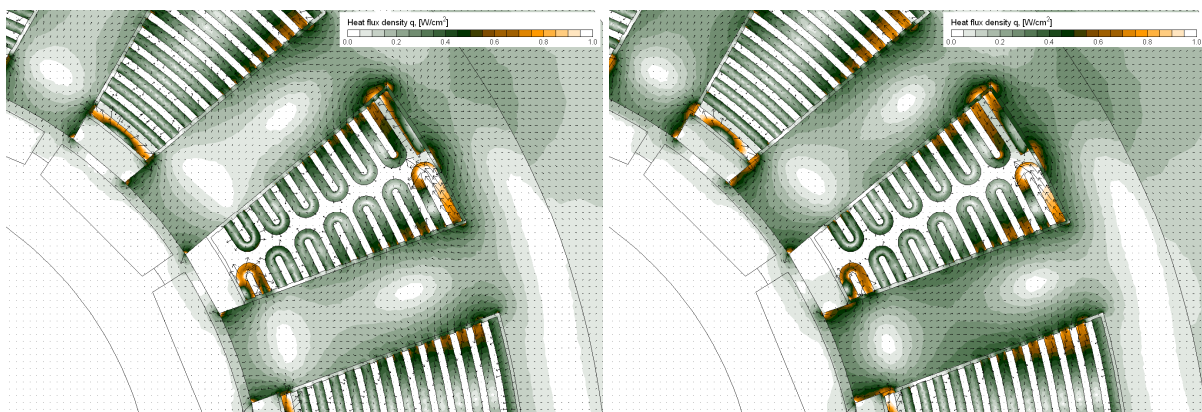


Figure 3.6 Heat flux density distribution at  $160\text{ W}/\text{m}^2\text{K}$  (left) and  $100\text{ W}/\text{m}^2\text{K}$  (right) forced convection on all cooling surfaces

Figure 3.7 shows the electromagnetic torque and flux linkage components for the machine with 3 winding segments out of 6. This reduction is made for the sake of simpler comparison to the prototyped machine.

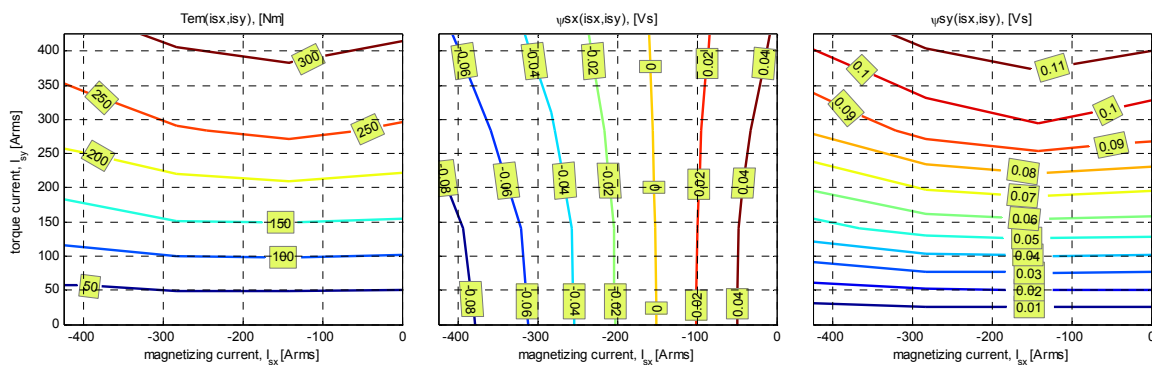


Figure 3.7 Average torque per revolution (left), phase peak value of magnetising flux (middle) and phase peak value of armature reaction (middle) as a function of current components (shown as rms values).

The 3D FE outcome of component analysis is shown accordingly: current density distribution at **300 A** DC (Figure 3.8) and the corresponding power loss density (Figure 3.9) and the resulting temperature (Figure 3.10). The heat transfer coefficient of **200 W/m<sup>2</sup>K** is defined on all interior radial surfaces. Inlet temperature is defined **20°C** and outlet **120°C**. This temperature raise is defined as ambient or bulk temperature to the cooling condition. Resistive voltage drop across the winding terminals is **2V** that gives **6.7 mΩ** for the resistance.

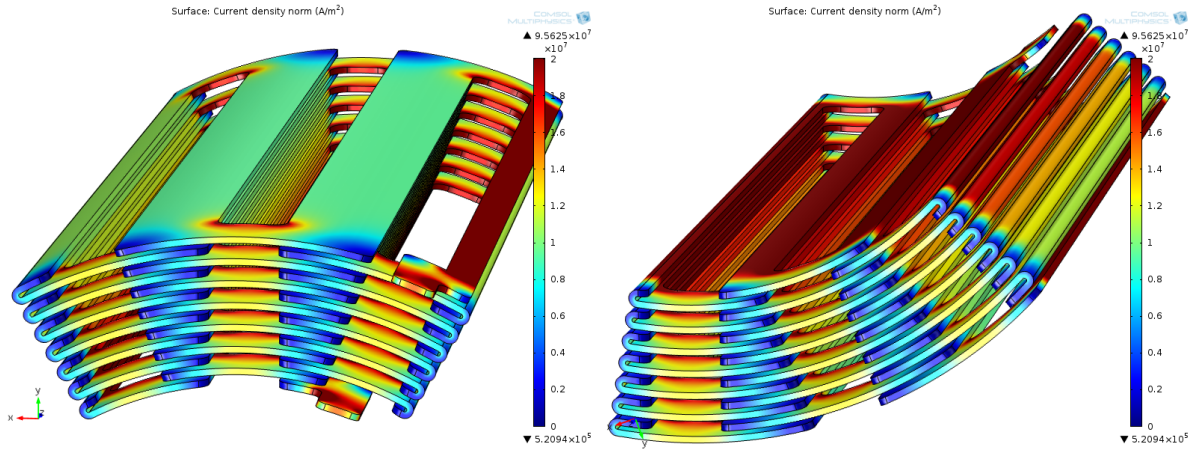


Figure 3.8 Current density distribution at 300 A DC

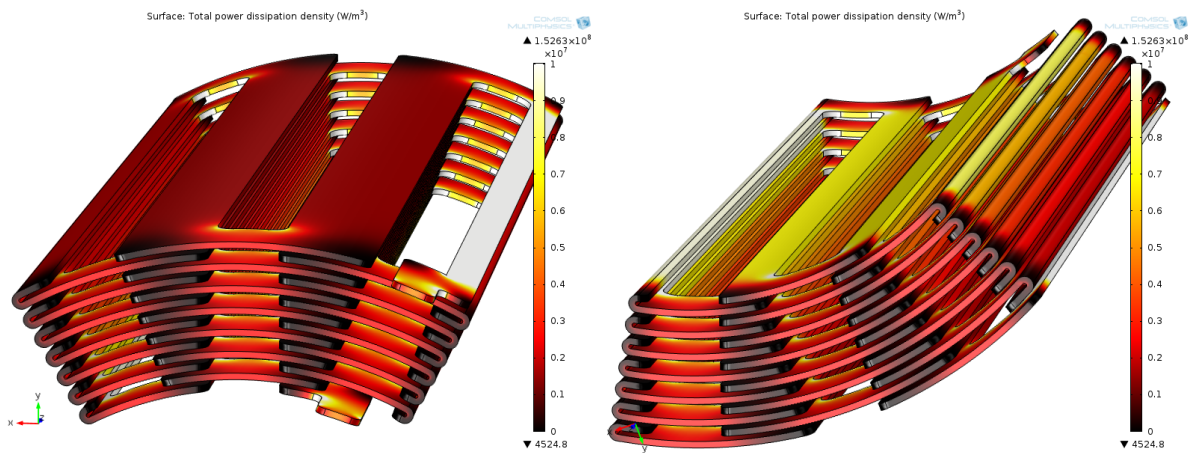


Figure 3.9 Power loss density distribution at 300 A DC

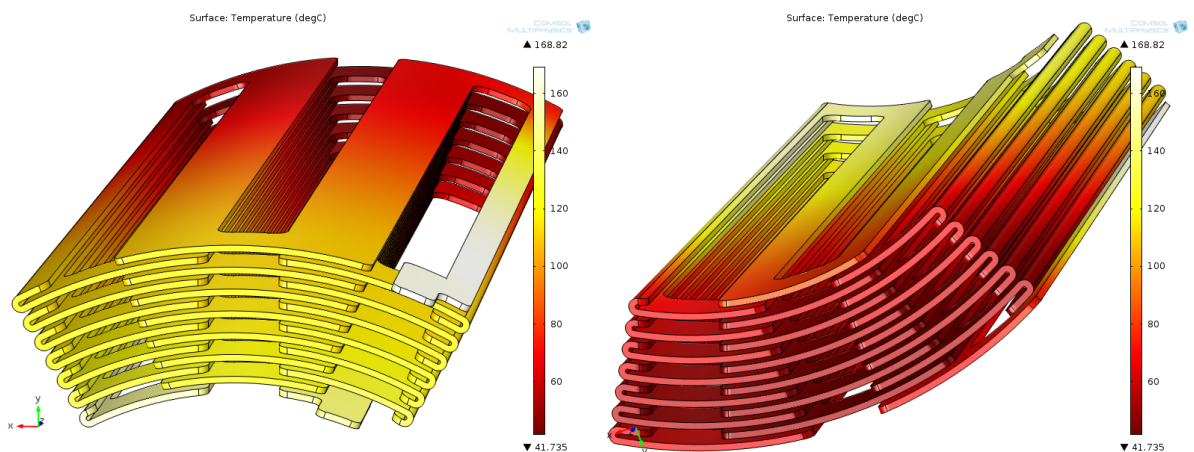


Figure 3.10 Temperature distribution at 300 A DC, convection 200 W/m<sup>2</sup>K and temperature raises from 20 to 120 °C along the winding

### 3.2 Machine construction

The exploded view of the machine construction is shown in Figure 3.11 and the stator cross section of assembly in Figure 3.12. The previously described topology and functionality faces now the resolve of production and assembling **specifications**. Once the stator segments are completed and aligned they are shrink-fitted into a case or housing that made of aluminum. The endplates have two bearing holes and extended surface for a plastic cylinder that closes the air exchange between the stator and rotor so that the coolant air passes through the winding only. Spring washer is used behind the bearing on non drive end (NDE) side. The electrical termination is defined also on NDE-side. As the electrical termination needs space and it might disturb the inlet flow into each slot and cooling duct it is suggested that the inlet side takes place on drive end (DE) side where the mechanical interface of the electrical machine is situated.

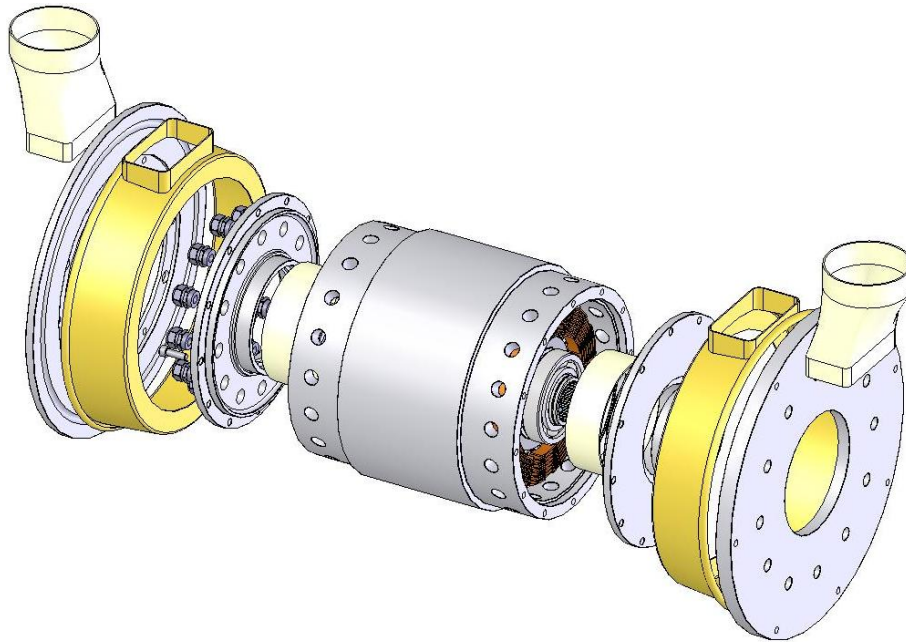


Figure 3.11 Exploded view of machine parts

The **cooling distribution** system is dimensioned according to the cross-sectional flow area and availability of standard components. The cross-sectional flow area in the winding, which is perpendicular to the flow direction, is  $693 \text{ mm}^2$  per winding segment. One of the most critical components in the flow distribution system is the shielding cylinder that is mechanically supported from the endplate and has to close the possible air leakage through the air-gap. Practically this non magnetic and electric material should have a good temperature capability and geometrical stability.

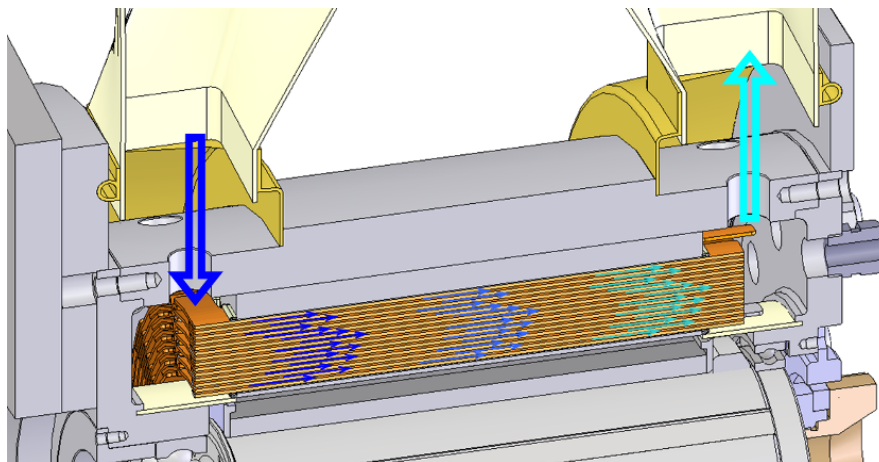


Figure 3.12 Cross-sectional view of the assembled stator and the coolant flow from the drive end towards non drive end

The crucial part of the machine construction is the manufacturability and ability to assemble the stator winding segments.

### 3.3 Design for manufacturability

The **winding segment** calls first for the turn to turn insulation and then for the main insulation before the **core segment** is inserted into the winding segment (Figure 3.13). The main insulation is placed just in prior to sliding in the core pieces. The edges of the insulation is rolled for increasing the creepage distance, this also assures that the core segment is placed axially in the middle for the required flashover distance. This **mounting and production strategy**, expected tolerances of constructional elements and selection of insulation material specifies the design for manufacturability in details for the **stator segment**. At the same time this specification does not assure that the design is easily produced.

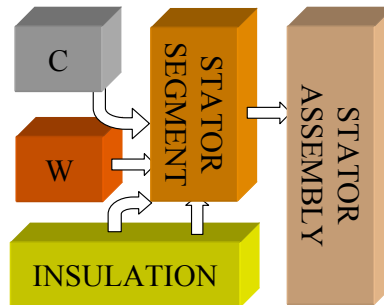


Figure 3.13 Principal sketch of the manufacturing process of the stator segments in prior to stator assembly

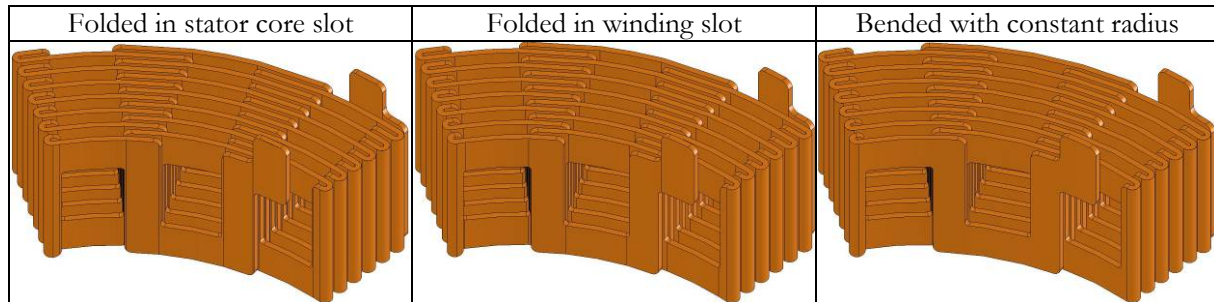
The course of **design agreement** takes a number of iteration involving even conceptual changes (Table 3.1). Once the conceptual layout is confirmed and the main dimensions are fixed the adjustments for rational production starts.

Table 3.1 Design development in prior to design freeze

Figure of a design development	Description
	<p>Stator core composed of free teeth mounted into a yoke ring and fixed with tension pins. This proposal (03FEB) is the first attempt to move towards the concept freeze with detailed design for manufacturability. The apprehensive outcome from production and assembling analysis listed a number of threads and weaknesses on production of modular windings, assembling and stability of core pieces. This design is abandoned due to complexity.</p>
	<p>The new concept and design (13FEB) takes advantage of a single tooth and a simpler coil type with special arrangement. The concentric fanned coil has expectedly rather good cooling capability and rather homogeneous heat generation for DC current. The orientation of the conductor sheets in respect to magnetic field causes enormous eddy current losses already at low frequency. Therefore this design is abandoned due to low energy efficiency.</p>
	<p>The radially oriented winding segments are selected because of smaller ac losses in the conducting sheets over the operation range. This design freeze is used to specify the materials, manufacturing and assembling details. This design (15APR) takes advantage of tooth notch to lock the slot, small welding slag and larger cooling channels due to assembling integrity.</p>

The **manufacturing process** for the winding segment (described in [8]) can take advantage of a slotting or a stamping at the first stage (Table 3.2). Alternatively the process of machining the winding slots can be remained as the last step for manufacturing of the winding segments before the cleaning and establishing turn-to-turn insulation. As a matter of fact at the early stage of the design finalization and confirmation the process of bending and folding is considered apprehensive from high manufacturing tolerances point of view. Therefore the curvilinear bending is chosen where the milling process in the last stage assures the fine tolerances (Table 3.2 last column). Alternatively, the slotted strip of conductor can be folded up by taking advantage of piece wise linear surfaces (Table 3.2 two first columns). The realization speed of this procedure is basically stacked to the reliable folding models that match with the folding processes. Once the mathematical model describes exactly the outcome of the manufacturing the 360 degree folds and few degree folds it is easy to define the slotting contours.

Table 3.2 three different types of radially oriented winding segments.



If the manufacturing process for the winding segment is more or less assured the **finalization** of the dimensions and tolerances starts (Table 3.3).

Table 3.3 Design adjustment and description

Design adjustment	Description
	15.0 mm winding slots with tight edge turns 1.0 mm in between  The uncertainty of the 360 degrees folds, correct specification and use of fold lines are the reasons for larger lateral space between the winding segments. Instead of tight 1 mm (space for double insulation) 1 more millimeter is added for larger tolerances.
	15.0 mm winding slots with spacey edge turns 2.0 mm in between  Initially 0.5 mm insulation, which can consist of a number of layers, is specified tightly around the windings with the tight connection to core pieces. Practically the insulation can be thinner to tolerate the deviation of the produced details.
	16.0 mm winding slots with spacey edge turns 2.0 mm in between  Here is one more change introduced if the geometrical deviation is so large that the thinner insulation liner becomes too chancy concerning to mounting and insulation strength. In this stage it is rather confident that the fine radiuses for yoke and winding can be achieved.



The design models and drawings are considered as **ideal** – there are perfect alignments between adjacent geometries without any extra space in between. Therefore the functionality is calculated for the ideal (geometrical) condition and the deviation is included later for the sake of production diagnostics and manufacturability for design updates.

### **3.4 Practical limitations**

The practically assembled machine compromises the **production speed** to completeness or perfectness. The production uncertainty causes reservations for larger production tolerances. The imprecision and shortage of experiences are related to folding and bending processes, which are involved in the winding production. Therefore the tooth width is reduced from **16 mm** to **14 mm** for unfailing winding production. Furthermore the tooth width is reduced from **14 mm** to **13.25 mm** for lateral core segments in prior to assembling in order to practically mount the stator segments. As a matter of fact these are not the only changes that the manufacturability and the ability to mount the produced components are introducing.

Three stator segments are used out of six. This means that the machine has **21-turns** per phase instead of **42** and the single segment operates of full dc link voltage instead of half. Furthermore, there are no shielding cylinders used that separates the coolant air from rotor and leakage through the air-gap. Therefore **9-14%** air leakage is allowed through the **0.5-0.8 mm** air-gap. This is the manufacturability feedback to the design.

## 4 Power losses in the stator

The estimation of power losses focuses first of all on a number of **suitable** power loss **models** for design and machine analysis. Usually the complexities of power loss modeling are significantly reduced in the design stage for the sake of speed and rough material modeling that would otherwise increase the computational time and efforts. Basically the maximum flux density values are defined at fundamental frequency for a few core regions to define the power losses in these regions. Likewise the dc conductor losses are usually presented at the operation temperature.

This section presents the estimation of core losses according to the initial procedure and introduces a more sophisticated method implemented in Matlab-Femm analysis routine. There are no additional efforts on improved material characterization that accounts the additional (stray) power losses in the magnetic core depending on flux density locus, frequency or duty, processing and packing. Despite that the material distribution or more exactly the ideal design layout of the winding is considered when the induced losses are calculated for rotating magnetic field and self induction. Once again numeric filed computation 2D FEM is used to analyze the AC effects over a wide range of frequency – supplying, rotating and both of them.

### 4.1 Magnetic power losses in the stator core

The initial data for the power loss calculation in the stator core is the magnetic flux density at predefined operation point and location of the core (Figure 4.1) also the catalogue data of the materials (Figure 4.2). The flux density values are picked from a single point and present the specific region such as a tooth or yoke. The flux density value can be a scalar such as a peak value over the magnetization period or the magnetization waveform itself. The natural selection point for flux density in the stator yoke would be angularly in the middle of slot and radially in the middle of yoke. Likewise to the stator tooth (Figure 4.1).

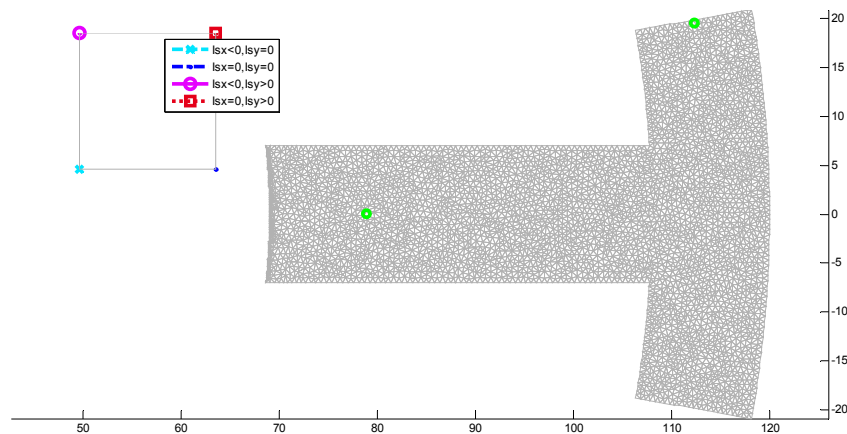


Figure 4.1 Definition of data and operation points

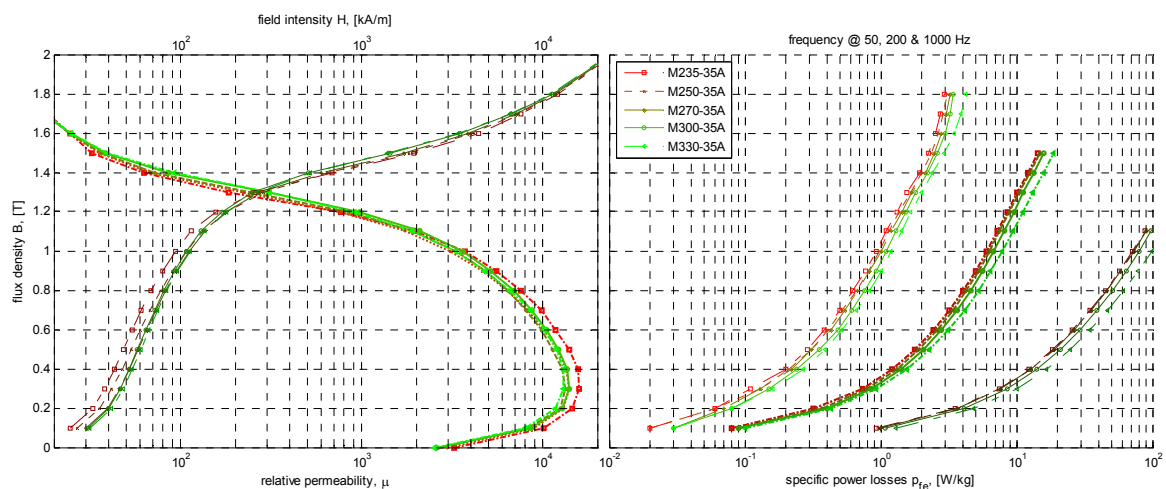


Figure 4.2 Material data for electromagnetic steels: magnetisation curves (dark thin lines) and relative permeability (light bold lines) on the left and specific core losses at 50, 200 and 1000 Hz on the right.

**Flux density and power loss maps**

For the sake of design speed the peak value of flux density is selected in the stator yoke and the teeth even though the directional components are available (Figure 4.3). By selecting the operation speed of the machine the fundamental frequency is defined and used for power loss estimation. Hereby *1500 rpm*, *3000 rpm* and *6000 rpm* are used as an example at the power loss estimation in the stator yoke and the teeth (Figure 4.4).

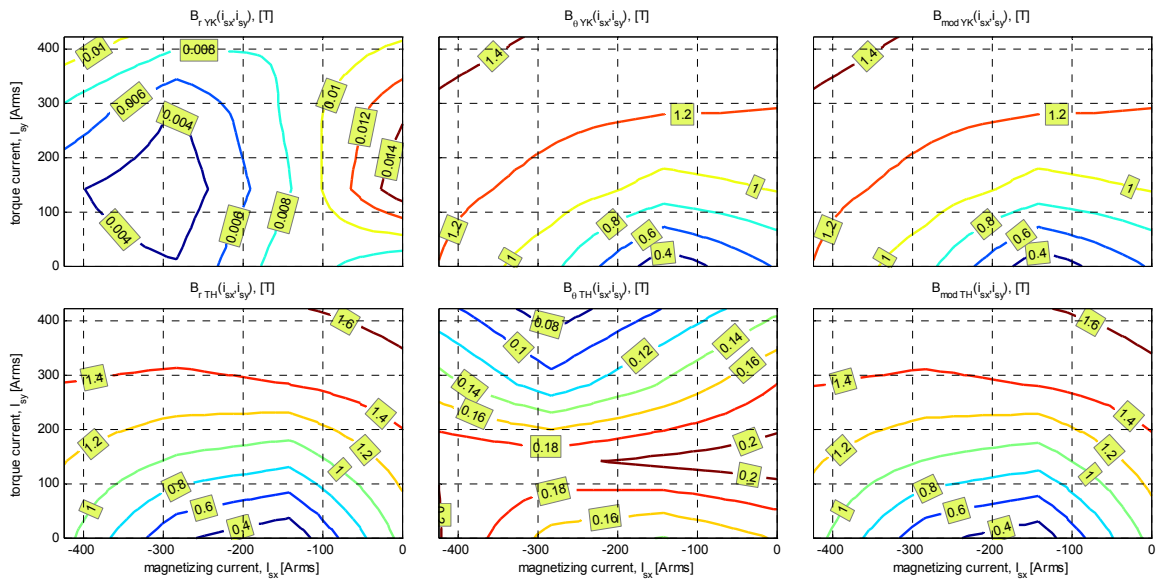


Figure 4.3 Maximum value of flux density component: radial (left), tangential (middle) and modulus (right) in the stator yoke (top) and stator teeth (bottom) as a function of current components (shown as rms values).

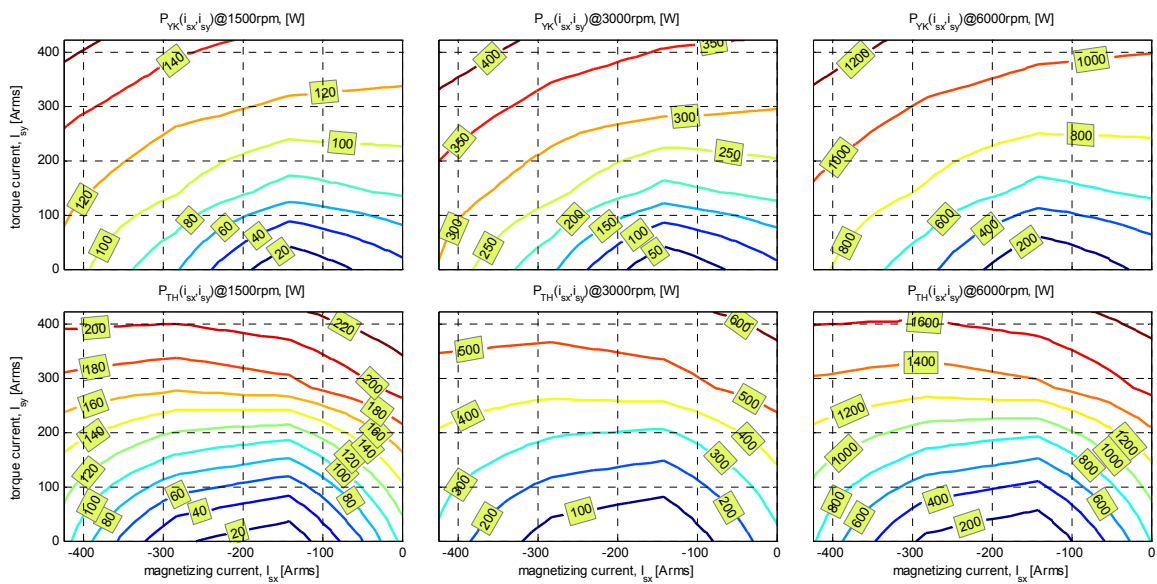


Figure 4.4 Estimated core losses at 1500 rpm (left), 3000 rpm (middle) and 6000 rpm (right) in the stator yoke (top) and stator teeth (bottom) as a function of current components (shown as rms values).

The belt volume of *12 mm* stator yoke is *1.68 dm<sup>3</sup>* and the total volume of stator teeth is *1.93 dm<sup>3</sup>* if the tooth width is *14 mm*. It is expected that the power losses are rather equal in the yoke and teeth over the nominal torque operation range. At the field weakening the power losses become more dominating in the yoke and the peak torque operation causes more power losses in the stator teeth than in the stator yoke. This simple mapping confirms also that *10%* change in geometry and flux density would cause *18%* less power losses for wider core and *19%* more power losses for narrower core.

### Flux density variation

The flux density variation is selected in the stator yoke and stator tooth (Figure 4.1) at four different operation points:

- $I_{sx}=-141.4$  Arms,  $I_{sy}=0$  Arms gives  $B_{\text{maxyoke}}=0.26\text{T}$  and  $B_{\text{maxteeth}}=0.28\text{T}$
- $I_{sx}=0$  Arms,  $I_{sy}=0$  Arms gives  $B_{\text{maxyoke}}=0.92\text{T}$  and  $B_{\text{maxteeth}}=0.87\text{T}$
- $I_{sx}=-141.4$  Arms,  $I_{sy}=141.4$  Arms gives  $B_{\text{maxyoke}}=0.62\text{T}$  and  $B_{\text{maxteeth}}=1.07\text{T}$
- $I_{sx}=0$  Arms,  $I_{sy}=141.4$  Arms gives  $B_{\text{maxyoke}}=1.01\text{T}$  and  $B_{\text{maxteeth}}=1.31\text{T}$

The flux density waveforms and components for the stator teeth and for stator yoke is shown in Figure 4.5 and Figure 4.6, respectively. Three of the operation points is actually tested for the prototype machine: idling point ( $I_{sx}=0, I_{sy}=0$ ), short circuit point ( $I_{sx}=-150$  Arms,  $I_{sy}=0$ ) and load point ( $I_{sx}=0, I_{sy}=150\text{Arms}$ ).

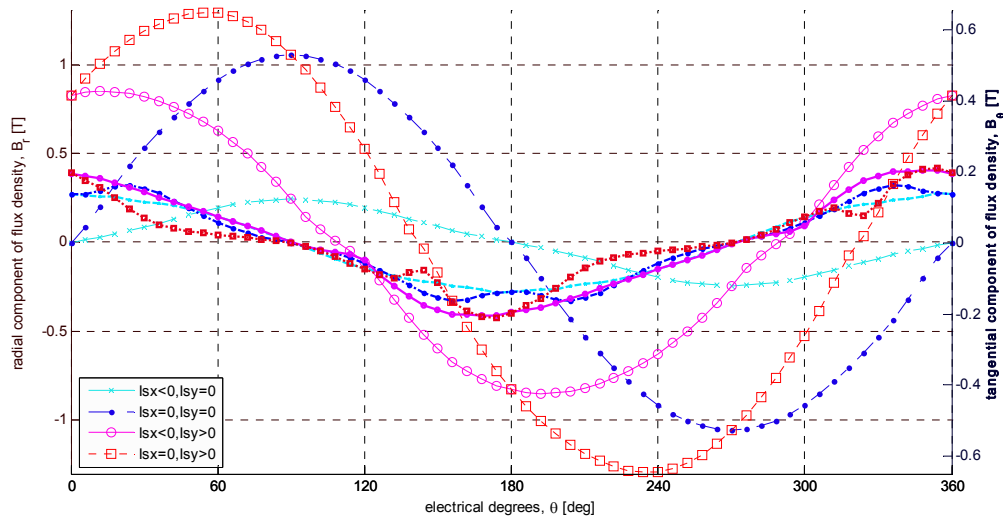


Figure 4.5 Flux density components and waveforms in stator tooth. Bold lines belong to bold vertical label.

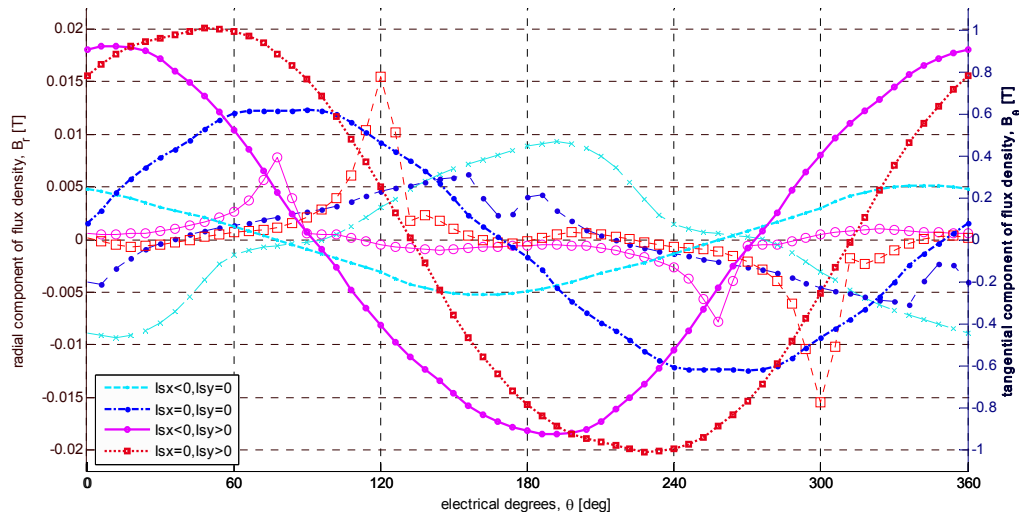


Figure 4.6 Flux density components and waveforms in stator yoke. Bold lines belong to bold vertical label.

The dominating component of density waveforms: radial component in the stator teeth and tangential component in the stator yoke are nearly sinusoidal with low harmonic content. Usually the radial and tangential flux density components are a quarter of period shifted and this determines the field rotation. If the corresponding waveforms are equal in magnitude the locus of field forms a circle, generally it is an ellipse. If the other component is considerably larger from the other then the field is purely alternating.

### Flux density pattern distribution

The main goal for this section is to investigate on how much the flux density variation differs from the ideal alternation at the fundamental frequency. Four predefined operation points are used as the result of flux density distribution analysis.

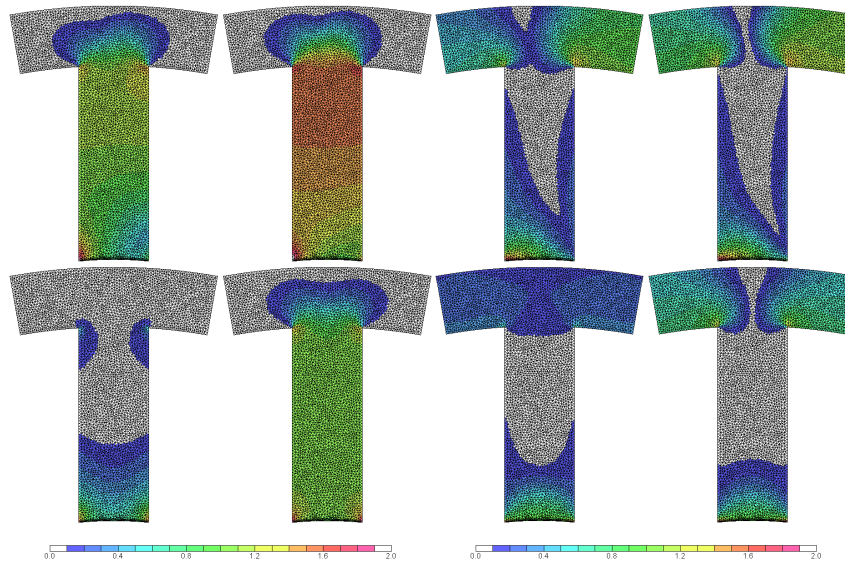


Figure 4.7 Flux density radial and tangential components.

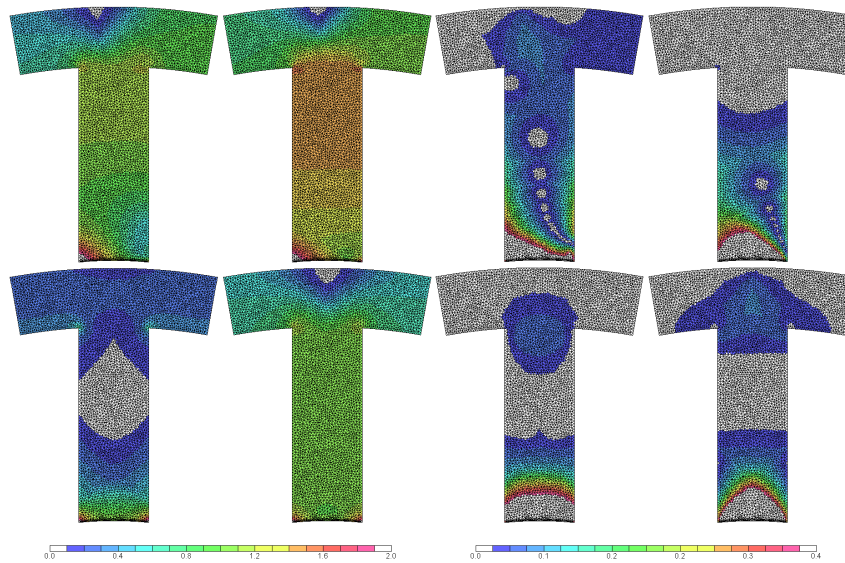


Figure 4.8 Major modulus (left) and minor modulus (right) of flux density

Figure 4.7 shows the peak value of the radial flux density component over the magnetization cycle (left) and the peak value of the tangential flux density component. These both components can be presented at the same rotor position due to armature reaction. If these two waveforms are displaced a quarter of magnetization cycle it would be easy to determine the locus of the flux density. The flux density locus is determined by following the variation of the flux density modulus. Figure 4.8 shows the maximum value of the flux density modulus over the magnetization cycle (left) and the minimum value of the flux density modulus (right). This information is used to define the major and minor axis of the flux density loci. A part of flux density variation the important factor is also the speed of the variation. Spectrum analysis is used to determine the harmonic content of the flux density distribution. Figure 4.9 shows the peak value of the fundamental flux density component over the magnetization cycle (left) and the peak value of the summed flux density harmonic content. Figure 4.10 shows the harmonic flux density distribution for the 3<sup>rd</sup>, the 5<sup>th</sup>, the 7<sup>th</sup> and the 9<sup>th</sup> harmonics.

SupCo

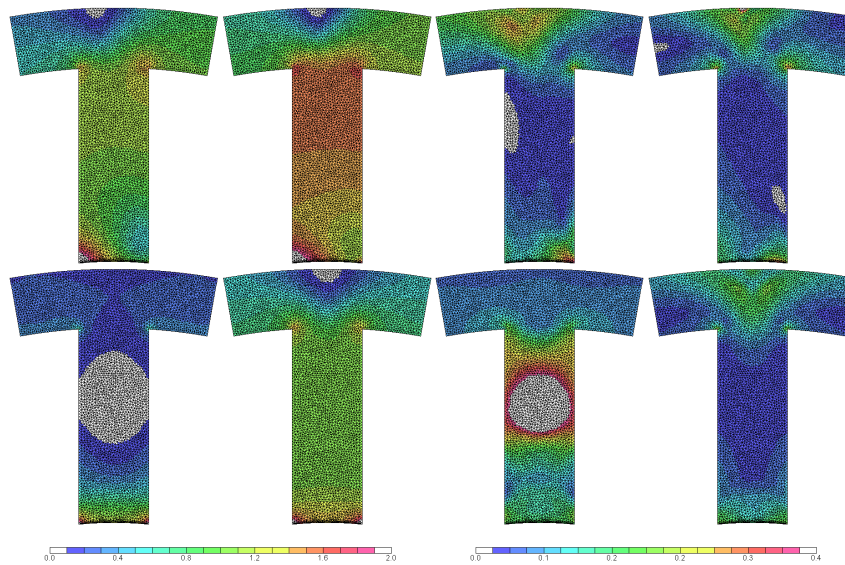


Figure 4.9 Fundamental component (left) and total harmonic distortion (right) of flux density

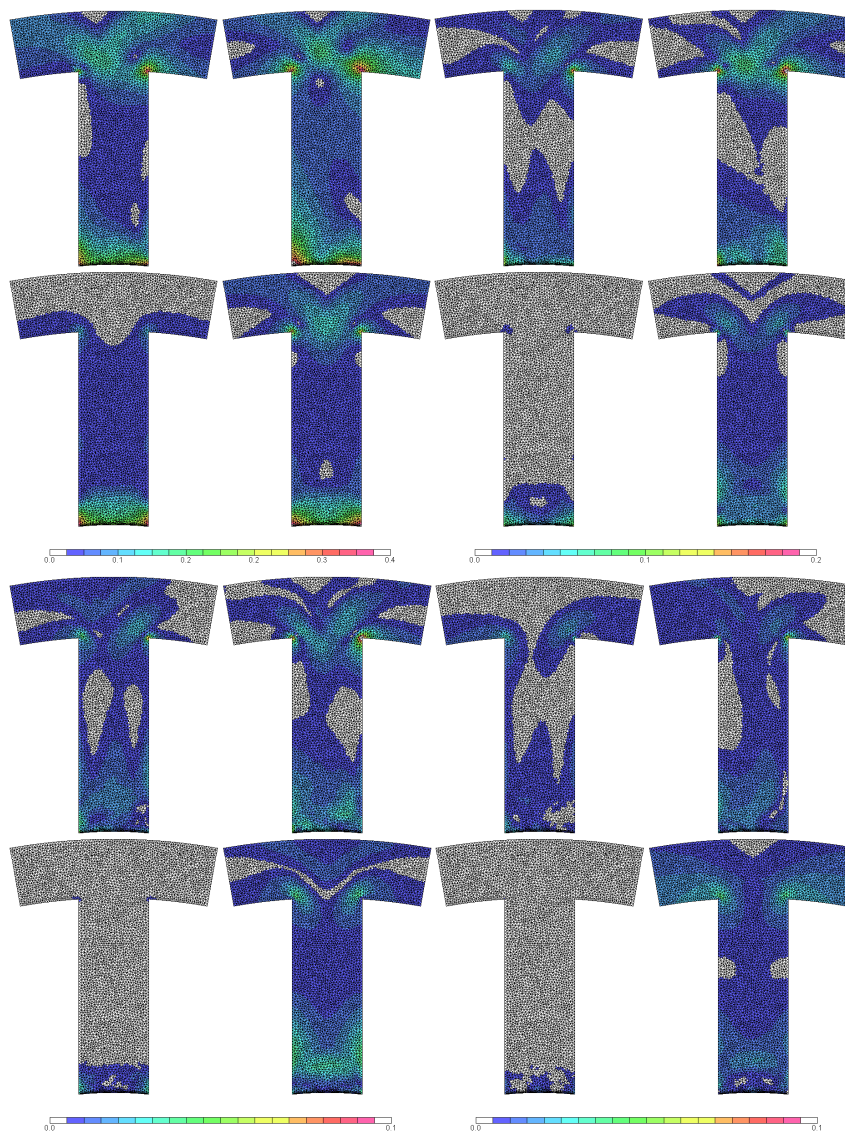


Figure 4.10 The 3<sup>rd</sup> harmonic (upper left), the 5<sup>th</sup> harmonic (upper right), the 7<sup>th</sup> harmonic (down left) and 9<sup>th</sup> harmonic (down right)

### Power loss models

The commonly used power loss model for magnetic cores is a sum of loss separation of the hysteresis losses, the eddy current losses and the anomalous or excess losses. The core loss coefficients are determined from the datasheets by using a curve fitting method so that the power loss function is rather connected to the measurement than theoretical expectations of classical eddy current losses or mathematical description of hysteresis. Anyhow, the measured power losses are the sum of different losses and the loss separation is the important part of the machine and design analysis.

$$p_{core} = k_h \hat{B}^n f + k_e (\hat{B}^n f)^2 + k_a (\hat{B}^n f)^{1.5} \quad 4.1$$

### Power losses in the stator core

The finite element wise power loss density in the stator segment is shown for the peak value of the modulus (Figure 4.11, left) at fundamental frequency and accumulated losses due to harmonic content at higher frequencies (Figure 4.11, right). The high harmonic losses are shown just to visualize the outcome of the method. It is expected that the derivative based loss prediction presents better the physical reality of the rapidly changing field. There are two selected references at the idling operation

- Speed 1500 rpm results fundamental 139.0 W and high harmonic 8.4W power loss that with 10% narrower tooth and 20% higher loss results  $P_{core}=176.8W$
- Speed 3000 rpm results fundamental 361.1 W and high harmonic 24.5W power loss that with 10% narrower tooth and 20% higher loss results  $P_{core}=385.6W$

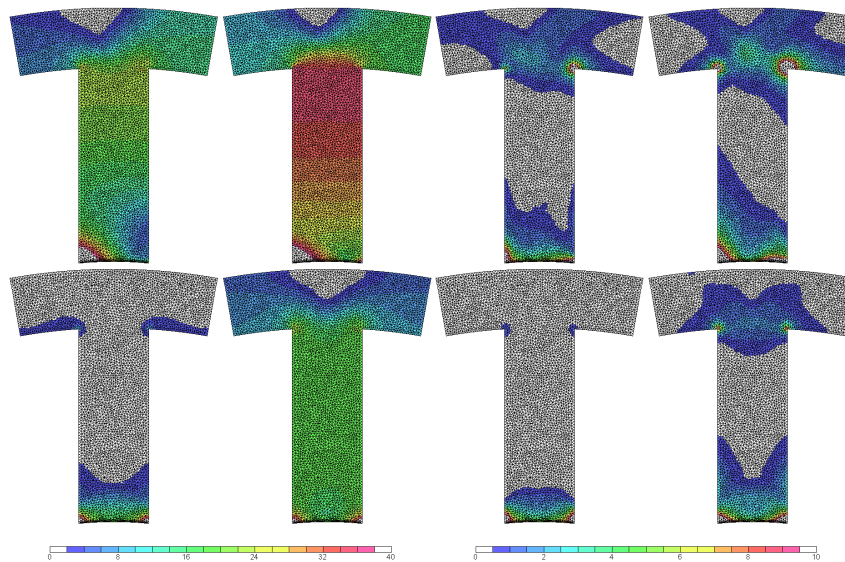


Figure 4.11 specific core losses [W/kg] at the predefined operation points

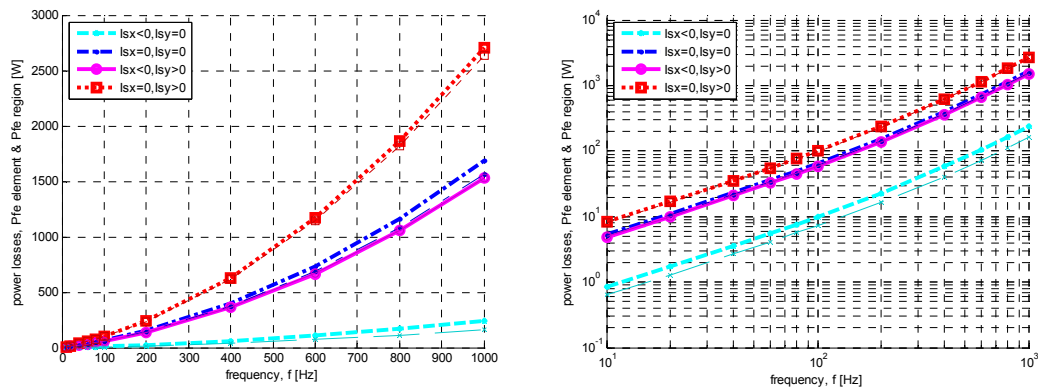


Figure 4.12 Estimated power losses in the stator core based on element wise calculation (light bold lines) and region wise calculation (dark narrow overlapped lines) as a function of frequency (75-7500 rpm) at 0 and 141.4 Arms.

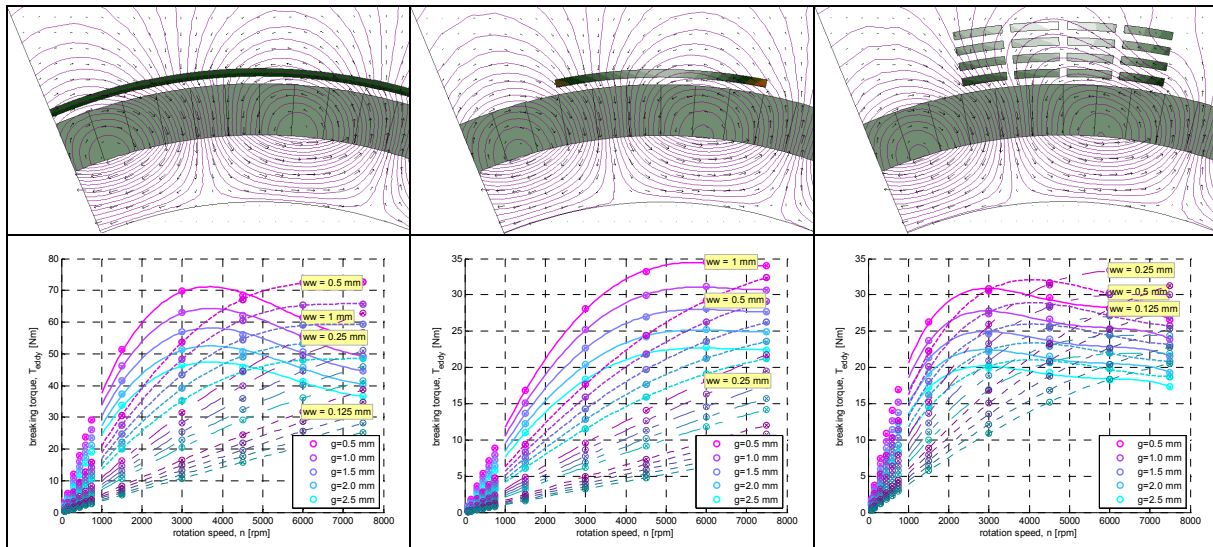
Figure 4.12 shows the core losses as the function of frequency for four different operation points. In this figure the finite element core losses are compared to the region wise loss estimation. The results are rather similar even though it is expected that the power losses are overestimated for the stator yoke and underestimated for the stator teeth when comparing the region loss estimation to element based loss estimation.

This is a rather usual phenomenon (known from scientific literature) that the estimated core losses based on test samples of Epstein frames or toroid is smaller than the estimated core losses for an actual rotating machine. Therefore, for the sake of loss separation, the different loss origins need to be determined. The power losses in the winding are analyzed next.

#### 4.2 Induced losses in the winding due to the field rotation

The initial breaking torque speed characteristics of the conductor sheets are used to estimate the influence of location and layout of the laminated windings in vicinity to the rotating magnetic field (Table 4.1).

Table 4.1 Pole pair model layout and the braking torque speed characteristics for different copper-ring parameters.



These torque speed characteristics (Table 4.1) remind the characteristics of the induction machine and it is seen roughly that the losses are proportional to speed (before knee) and the distance between the rotor and the conducting layer of the winding. This distance is  $6\text{ mm}$  for the prototyped machine. In addition the winding is partly shielded by the stator teeth and the winding is oriented so that it gives low AC losses in respect to the dominating leakage field in the stator core slot.

Instead of an actual rotor with surface mounted magnets a rotating excitation ring of electric currents is introduced. The thickness of current conducting sheet is the same as the height of the magnets and the magnitude of the distributed current vectors brings the magnetic induction of the air-gap at the same level as the actual model of the rotor with surface mounted permanent magnets. Following settings are used in the time harmonic magnetic problem

- The electric conductivity of the winding conductor  $57.14\text{ MS/m}$  ( $17.5\text{ n}\Omega\text{m}$ ) is defined at low temperature  $20^\circ\text{C}$  and moderate temperature  $40.82\text{ MS/m}$  ( $24.5\text{ n}\Omega\text{m}$ )  $120^\circ\text{C}$
- The magnetizing current density for the magnets is  $J_{\text{mm}}=130\text{ A/mm}^2$  that basically defines the first harmonic of the rotating magnetic field
- Stator currents are selected either 0 or 150 Arms. The field angle between the rotating field and the stator currents are selected to represent the demagnetizing short-circuit operation point.

Figure 4.13 and Figure 4.14 shows the current density distribution at the idling and short circuited machine, respectively, at  $1500$  and  $3000\text{ rpm}$ . The current density is represented for the windings where the electric resistivity is  $17.5\text{ n}\Omega\text{m}$  ( $@20^\circ\text{C}$ ). Table 4.2 summarizes the calculation results where the power losses of the conductors are shown according to location: gap vs. all layers and regular slots vs. edge slots, and resistivity of conductor:  $17.5\text{ n}\Omega\text{m}$  ( $@20^\circ\text{C}$ ) vs  $24.5\text{ n}\Omega\text{m}$  ( $@120^\circ\text{C}$ ).



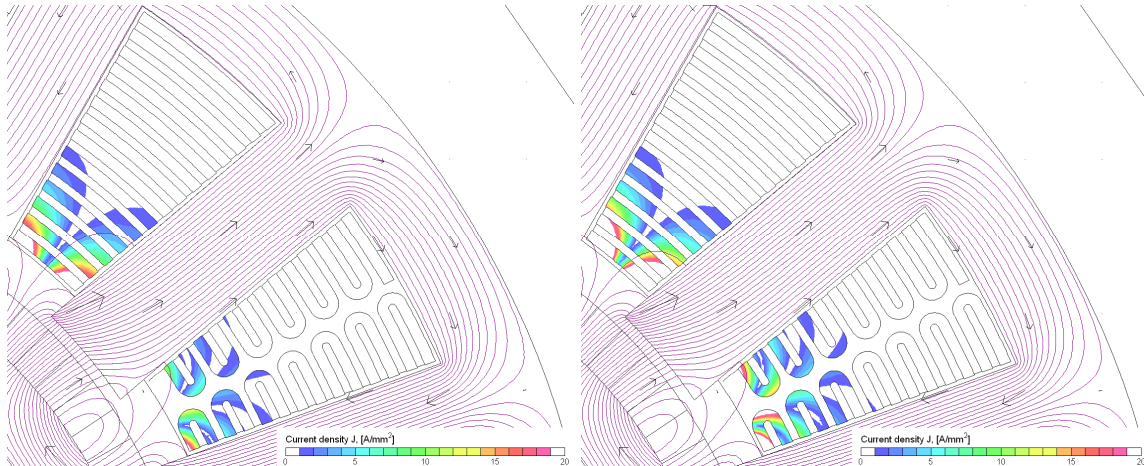


Figure 4.13 Current density distribution at 1500rpm 200Hz (left) and 3000 rpm 400Hz (right). The peak value of current density in the gap layer and in the regular slot is 36.1 and 67.8 A/mm<sup>2</sup>, respectively. The peak value of current density in the gap layer in the edge slot is 20.9 and 42.6 A/mm<sup>2</sup>, respectively.

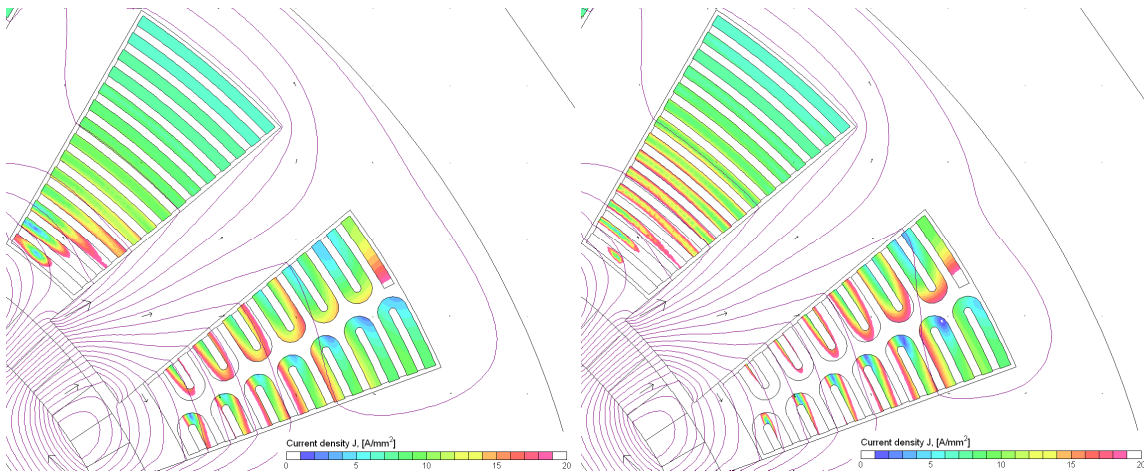


Figure 4.14 Current density distribution at 1500rpm 200Hz (left) and 3000 rpm 400Hz (right). The peak value of current density in the gap layer and in the regular slot is 51.4 and 78.5 A/mm<sup>2</sup>, respectively. The peak value of current density in the gap layer in the edge slot is 52.7 and 91.6 A/mm<sup>2</sup>, respectively.

Table 4.2 Induced power losses in the laminated windings at 1500 and 3000 rpm with 17.5 – 24.5nΩm

Conductor location	Losses in idling machine windings @ 200 & 400 Hz [W]		Losses in short circuited machine windings @ 200 & 400 Hz [W]	
	1500 rpm	3000 rpm	1500 rpm	3000 rpm
Regular slot gap layer	12.6 – 9.5	40.6 – 32.9	19.9 – 18.1	54.9 – 46.5
Regular slot all layers	17.5 – 13.4	53.2 – 44.6	75.5 – 87.7	141.2 – 140.3
Edge slot all layers	1.9 – 1.3	7.2 – 5.2	19.5 – 17.5	61.0 – 47.7
Edge slot all layers	2.7 – 1.9	10.4 – 7.6	114.9 – 118.6	289.9 – 248.3
Phase segment	37.7 – 28.7	116.8 – 96.8	265.9 – 294.0	572.3 – 528.9
All segments and phases	226.2 – 172.2	700.8 – 580.8	1595.4 – 1764.0	3433.8 – 3173.4

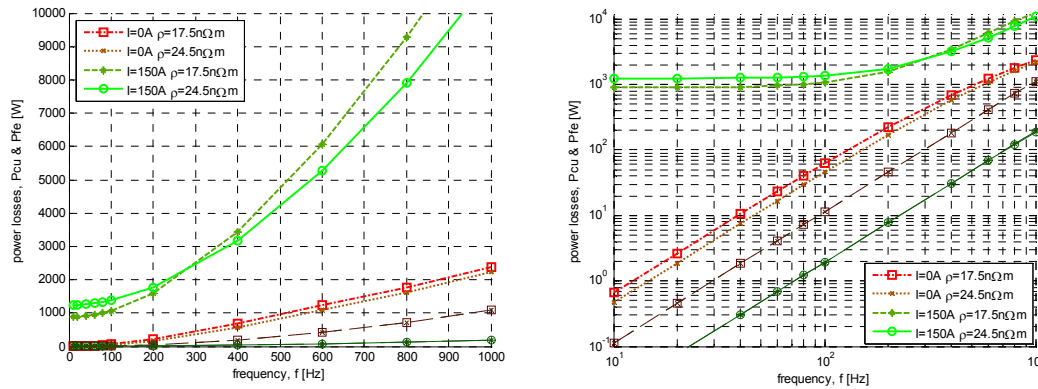


Figure 4.15 Induced power losses in the windings (light bold lines) and in the core (dark narrow overlapped lines) as a function of frequency (75-7500 rpm) at idling point ( $I=0A$ ) and short circuit point ( $I=150A$ ).

Figure 4.15 shows the same power loss characteristics at idling and short circuit conditions at different electric rotation frequency and resistivity values for the winding conductor. The core losses are also included on the graphs and contain only eddy current losses in the stator core.

### 4.3 Induced losses due to self induction

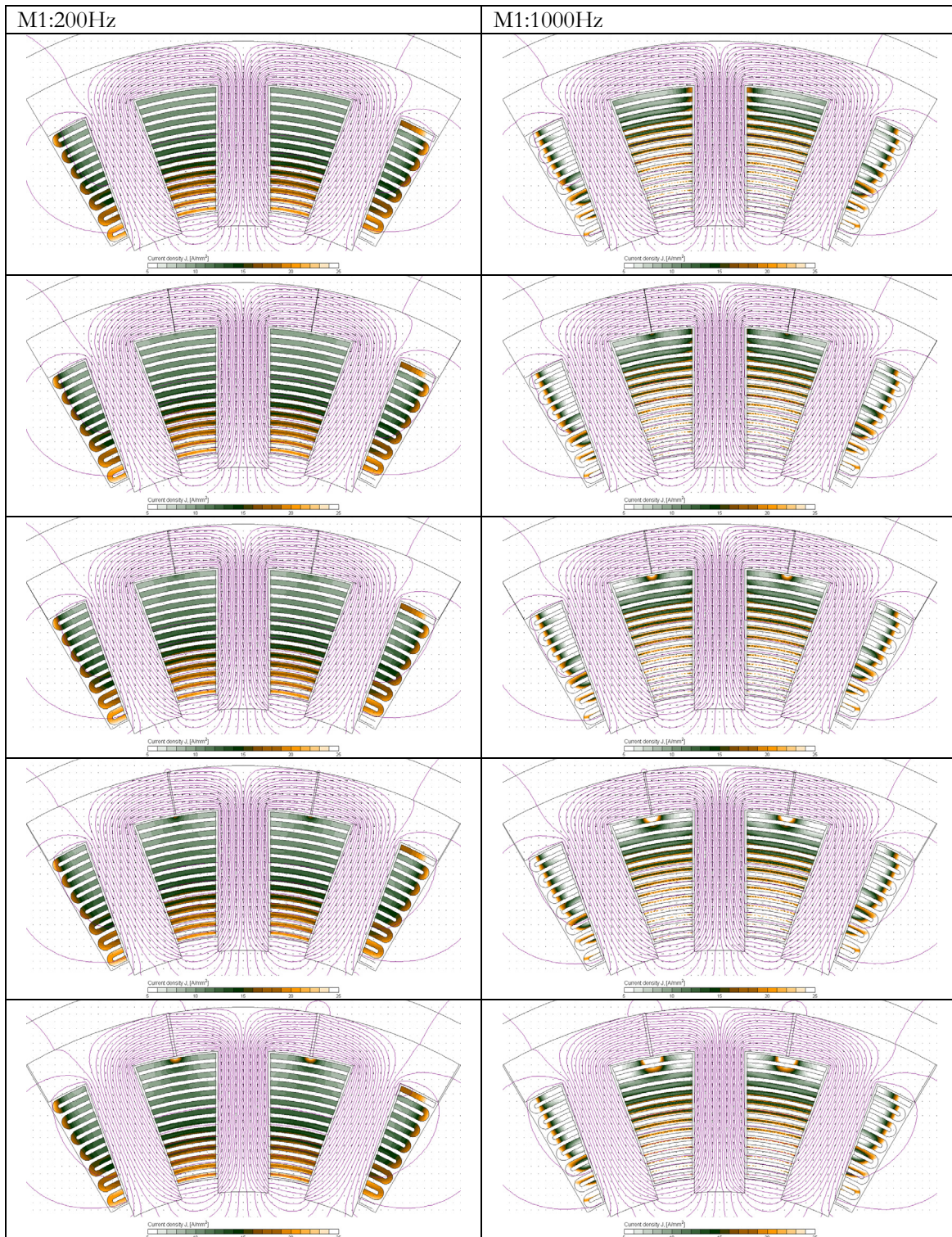
The time harmonic magnetic problem is developed from slot model in [8] towards stator segment model. The stator segment covers all the active length of the winding segment including edge turns but excludes end turns. The analysis focuses mainly on the calculation of winding parameters such as resistance and inductance, which is measured by impedance meter, rather than power losses like in [8]. The following calculations are processed

- Frequency sweep from 20 Hz to 200 kHz
- Current range from few milliamperes up to nominal current
- Changing material properties such as resistivity of the winding
- Including and excluding the resistivity of the housing cylinder (in aluminum)
- Analysis of yoke air-gap between the segments

The calculation results – current density distribution as a function of yoke gap and frequency is shown in Table 4.2 and the impedance characteristics after the measurements of the during the prototyping process Figure 6.11. The yoke gap is 0, 0.1, 0.2, 0.4 and 0.8 mm.

The calculation results show that conductivity of core is not really distinguishable from the RL measurements of the winding. This is the same for moderate current variation.

Table 4.3 Current density distribution of the winding due to self induction at different space between the core segments



#### 4.4 Other production specific power losses

The stacking of laminations causes small misalignment between the laminates and this is considered as a drawback. This becomes actual when a number of stator segments that has to be aligned so that a good mechanic and magnetic integrity is achieved. The mating surfaces can be machined so that a good tolerances and mate is achieved. This machining can introduce a new challenge by locally short circuiting the laminates. This case is analyzed in Figure 4.16.

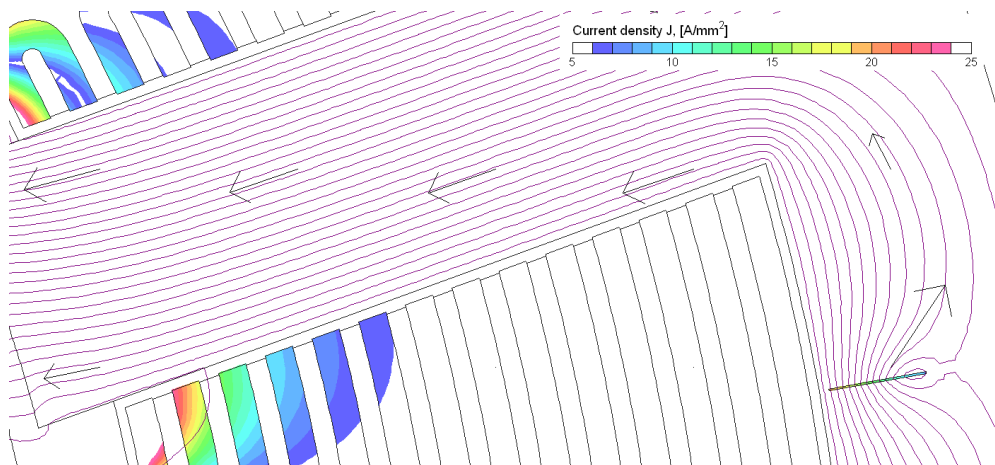


Figure 4.16 Current density distribution of an idling machine at 1500 rpm. 0.1x5 mm conducting layer is introduced in the stator yoke between the laminates.

The 2D FE quasistatic analysis at 200 Hz shows that the power losses in the short circuited 0.1x5 mm bar causes 2.34 W power loss that increases to 42 W when considering all connecting surfaces between the stator segments in yoke regions. The power losses of the single short-circuited bar through the lamination at 400 Hz increases to 7.18 W that in total becomes 129.2 W.

The development of the lamination alignment/unalignment analysis is started and not really completed for the profit of the machine analysis. There are flux density distribution (Figure 4.17) and current density distribution (Figure 4.18) of 7 aligned and unaligned 0.35 mm laminations that is used for the model development.

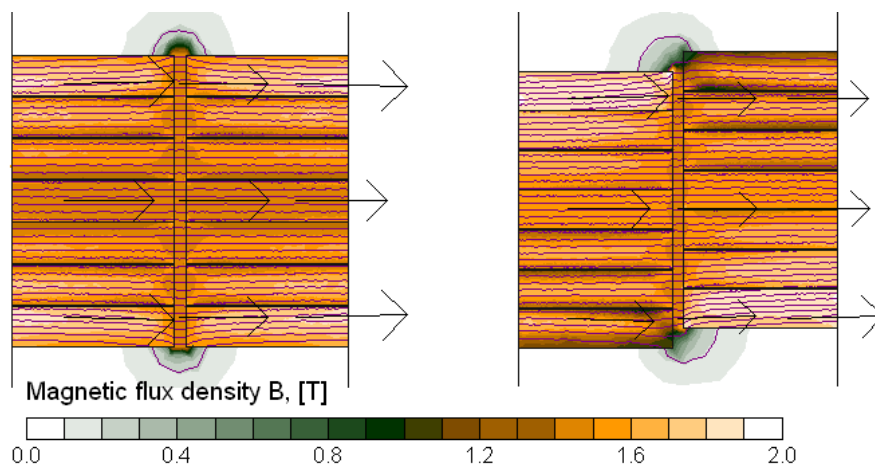


Figure 4.17 Flux density distribution of aligned and unaligned 0.35 mm laminations

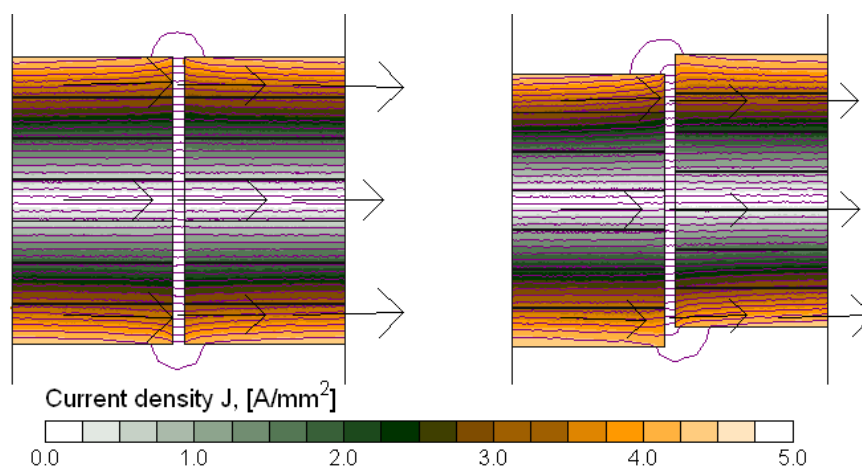


Figure 4.18 Current density distribution of aligned and unaligned 0.35 mm laminations

There are considerable amount of research related to production related core losses such as welding, lamination alignment, overheated regions due to laser cutting and so on. Due to time limitations this research is not continued here.

## 5 Prototyping of a stator with laminated winding segments

The project work is declared having two lines: design and production. Practically, these two separate lines are extremely tightly connected in [design for manufacturability](#) and [manufacturability for design](#). If the design carries the idea then the design for manufacturability assures that the idea is practically realizable likewise if the production has a competitive method the manufacturability for design guarantees that the production method has a chance to become a competitive product. The product of this project is not just a component such as a winding or a specific cooling arrangement it is a complete electrical machine with much higher internal power losses that has to be dissipated by the forced external cooling. Therefore, the project is not just an improvement of existing solution rather than innovating and exploring unconventional and alternative solutions.

The outcome of production models or the prototypes are basically the practical limitations related to manufacturing and assembling tolerances in conjunction with power losses, cooling intensity and dielectric strength. The lack tight links between design for manufacturability and manufacturability for design causes the discrepancy between the modeled expectations and measured reality. As an outcome most of the easily manageable laminated winding structures are excluded from the machine application due to the wide frequency range that could cause high power losses, low efficiency and excessive thermal loads.

### 5.1 Assembling chronology

Table 5.1 summarizes the assembling chronology with the links to the experimental work and the corresponding evaluation. Beyond doubt, there are more results and analysis of achievements that this document actually covers pr the table presents.

Table 5.1 Main milestones in an assembling process

Datum	Process description	results	evaluation
26.AUG	First assembling of a core C19, winding W5 and 0.2 mm liner		
28.AUG	Test assembling of stator teeth at BEVI		
01.SEP	Arrival of 18 stator teeth, check measurements	Table 5.5	
02.SEP	First assembling of a stator segment (S-W5)		
03.SEP	H-test of S-W5 at U=const AC voltage, initialization		
04.SEP	H-test of S-W5 at U=const DC voltage		
07.SEP	H-test of S-W5 at U=const		
08.SEP	Preassembling study, reducing sharpness of edges		
09.SEP	Coating (W1, W2, W3, W4), impedance measurement		Figure 6.3
10.SEP	Winding reparation (W5, W6)		
11-13.SEP	Assembling of stator segments, E-tests and M-tests	Figure 5.9	Figure 6.5
15.SEP	Reassembling analysis		Figure 6.4
16.SEP	H-test of all stator segments, I=const	Table 6.1	Table 6.2
17.SEP	Provisional assembling of stator, E- and M-tests	Figure 5.10	Figure 6.6
18.SEP	M-tests, disassembling of stator segments,		
19-21.SEP	Modifications on coils, recoating, reassembling of stator segments		
24-25.SEP	Core adjustments, pro-reassembling of stator, E- and M-tests	Table 5.7	Figure 6.7
01.OCT	Preparation for stator assembling		Figure 5.7
02.OCT	Trials for stator assembling at BEVI		
06. OCT	Final assembling of core segments with 3 windings at BEVI	Figure 5.10	
09.OCT	Completions for machine assembling at BEVI		Figure 6.8
10-11.OCT	Remounting of NDE, E-tests, delivery		Figure 6.9
12-21.OCT	Preparation for machine testing at test bench	Figure 7.1	
22-23.OCT	Measurement campaign with focus on electromagnetics		
05-09.NOV	Measurement campaign with focus on heat transfer		
16-18.NOV	Return, E- and M-tests, machine disassembling		Figure 6.10

## 5.2 Radially oriented laminated winding segments

Winding production steps, which are visualized and described shortly in [8], are listed below and some details focused in Table 5.2:

1. Cutting copper strips 236 x 1326 (theoretical length)
2. Specifying bend lines for folding
3. Pre-folding approximately 90-100 degrees angle
4. Post-folding – the winding layers are folded into contact to the support material, which is 1 mm thick aluminum sheet, that defines the thickness for the cooling duct
5. Bending – the curvilinear shape of the winding is given in the compression in between half hollow cylinder, which defines outer radius, and a solid inner cylinder, which defines inner radius.
6. Cutting slots
7. Cutting ends
8. Welding terminals
9. Smoothing, blasting, cleaning – abrasive blasting is used to smooth sharp edges and corners, and clean rough contaminated surfaces of the winding segments. The pressured stream of abrasives is even used to reinforce the structure of surfaces of the stacked cores where the milling process has caused the electric contact between adjacent lamination sheets.
10. establishing turn-to-turn insulation by coating with Ultmeg – 3 hours at 140°C

The winding segments are folded, bended, slotted and cut so that a conventional distributed concentrated winding with 7-turn coil around a tooth and 3 teeth in series is replaced 14 layer laminated winding with 1.5 turns per layer. There are following design concerns and production assessment listed below. Due to time limitations this research is not analyzed and discussed here.

- winding segment packing, tilting, deviation and tolerances. Theoretical expectation is compared to the practical outcomes (Figure 5.1). Improved image recognition and referencing becomes a powerful tool for product evaluation for design and manufacturing.

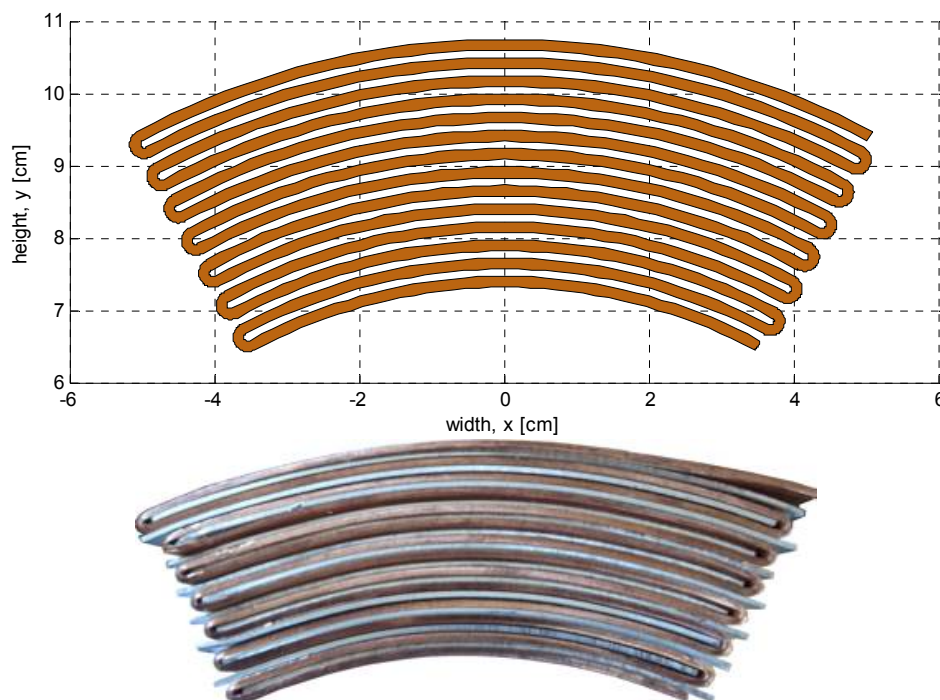


Figure 5.1 Theoretical layout (top) and practical outcome (bottom) of the folded and bended winding segment.

- Assembling winding segments (Figure 5.2) is an experimental work that focuses on the best fit of the geometrical deviations. The winding segments have at least 3 mm laterally in between, which is 1 mm more than expected.

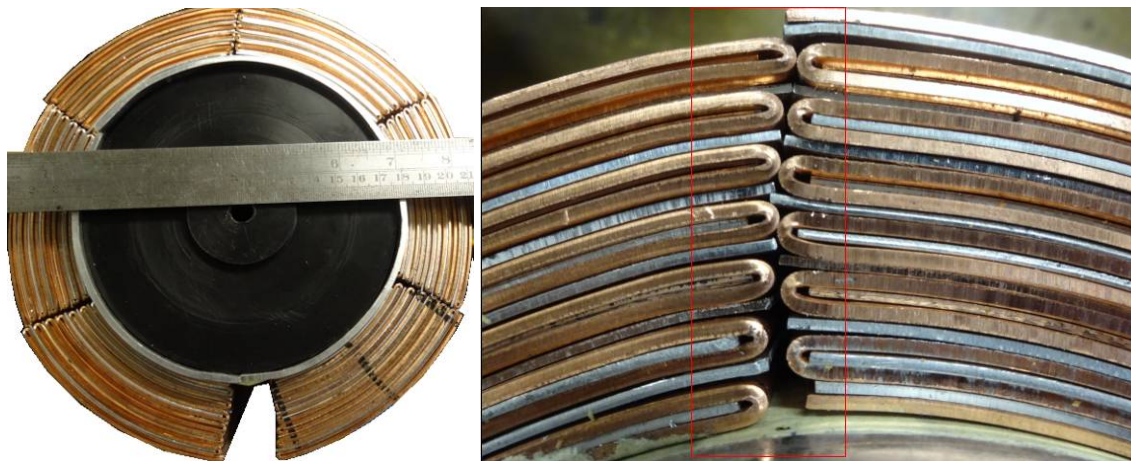


Figure 5.2 Test assembly of winding segments (left) and detailed view of the edge regions of two adjacent segments (right)

The geometric models are used in assembling analysis (Figure 5.8). Table 5.2 covers some of the production steps of the winding segments.

Table 5.2 Detailed views of the winding surface and corners

Description	Figure 1	Figure 2
Bended winding segment with 1 mm aluminum sheets in between. The edges of the winding segments are rather straight but they are tilted clock wise direction. Some more production information is given in [8].		
The slotting of the winding is rather time consuming manufacturing process for this prototype but it has high accuracy. The challenging problem is fixation and balance between the narrow edge turns. The slot width is 15.0 mm.		
The edge turns can occasionally cross-section area less than 10 mm <sup>2</sup> . The end turns is formed by removing the material from the end of the winding slots. This manufacturing process does not need high precision or accuracy.		
The smoothing process of the sharp winding edges is time consuming like all other manual operated processes. The enlarged image shows clearly that the edges have lack of coating. Figure 2 shows the same edge after smoothing.		



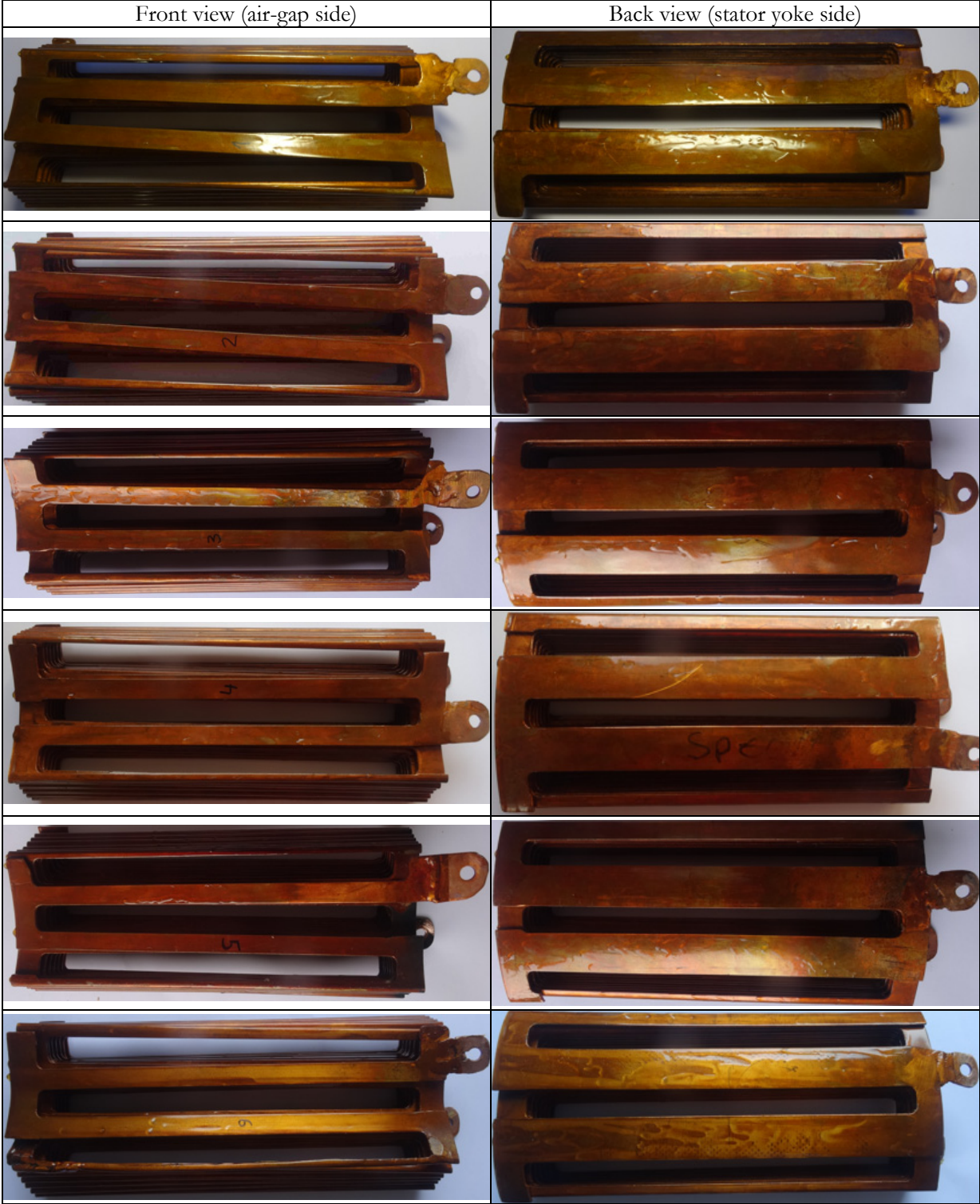
Table 5.3 presents the measurement results of the edge turns from terminal side toward not terminal side. Four different corners are measured at 3 different places for 3 different windings. Similar measurements are occasionally made for the other windings but they not included into this table.

*Table 5.3 width of inner and outer edge turn*

#C	NDE right inner corner			NDE right upper corner			NDE left inner corner			NDE left upper corner		
W1	3.50	2.40	2.85	12.30	11.75	12.05	5.80	5.70	5.65	6.75	6.60	7.15
W3	4.25	4.95	5.10	13.05	12.35	11.80	4.90	3.80	3.30	7.20	8.25	9.20
W6	3.55	3.40	4.10	12.70	12.25	12.00	6.35	6.80	7.10	6.80	6.60	6.60

Table 5.4 shows the front and back view of the winding segments before assembling the stator segments. The direction of view is defined from magnetic field point of view where the front is towards the air-gap and back is towards to stator yoke. Each row in this table corresponds to one winding from W1 to W6. Winding segment W4 has a turn around layout compared others, inner terminal of W5 is repaired and inner edge turn is reinforced in W6.

Table 5.4 Front and back views of winding segments



**5.3 Stator core segments**

The material for the stator core is selected among the commonly used 0.35 mm electromagnetic steels for traction machine applications. The selection criteria are price and availability.

Types of materials used for the prototype

- M250-35A/C5, 11100 pcs, stacked by welding (batch 1)
- M270-35A stacked by gluing (batch 2)

Figure 5.3 shows the parameterized CAD drawing for the segment that is used for both batches of the laminations for the stator core segments. The only difference in the layout is that the welding groove is not used for the second batch. Figure 5.4 is the image of the alignment and stacking rig that is used for both batches. Figure 5.5 shows the outcome of the first tooth from the first batch and Figure 5.6 shows the outcome of the first tooth from the second batch. The local thermo-mechanical loads due to welding have caused uncontrollable geometric change of the stacked structure. Due to the unaccepted assembling tolerances this stacking method by welding is replaced by gluing.

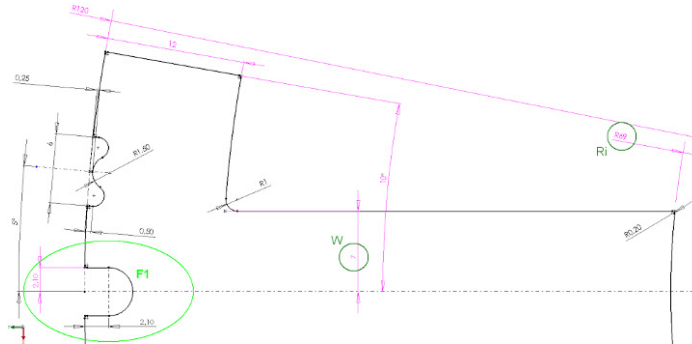


Figure 5.3 Dimensioning of the first T-lamination. The second T-lamination does not have channel for welding

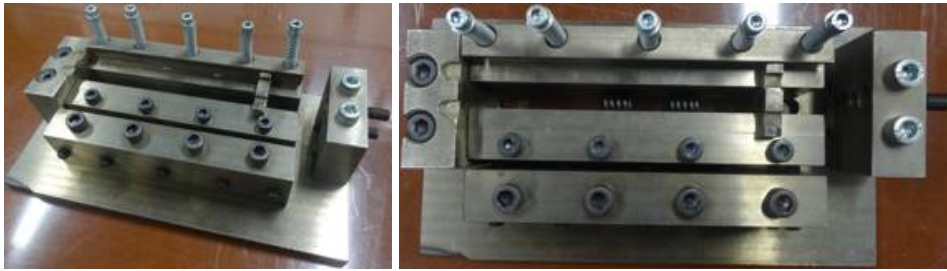


Figure 5.4 Stacking, alignment and engagement rig for stator segments

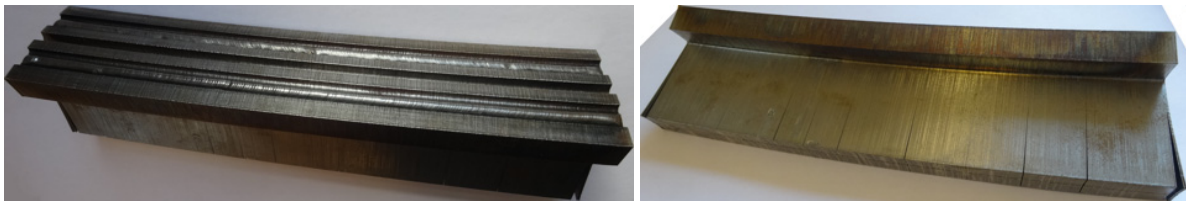


Figure 5.5 Welded stator segment

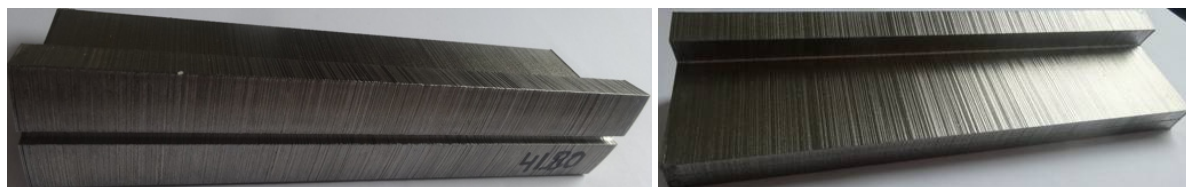


Figure 5.6 Glued stator segment

The theoretical width for the stator segment is 41.68 mm, which is the distance defined by 20 degrees angle at 120 mm radius. As a matter of fact 0.1 mm decrease in segment width results 0.3 mm reduction in radius. Table 5.5 presents some of the measured width of the produced and slipped (except #19) core segments. As it seen from the table the core segment width is smaller. Therefore the inner radius of the yoke and stator has a tendency to become smaller than specified but not smaller than allowed).

Table 5.5 Width of stator core segments

#C	1	2	3	4	5	6	7	8	9	10	11	12	13	14	15	16	17	18	19	
	41.57	41.57	41.67	41.61	41.57	41.65	41.60	41.57	41.62	41.69	41.63	41.61		41.61	41.59	41.59	41.61			41.80

The local short circuited surface regions are one of the research topics. The core surfaces are smoothed by slipping. This causes short circuits as the impedance meter shows considerably lower resistance for the slipped cores than to the unslipped core (Table 5.6). Additional measurements are recorded (Figure 5.7) where the core segments under the test are placed on top of the primary core with 8 winding turns. Geometrically the arrangements of these two core segments are in a similar way where the corners of the yokes are in contact with the sides of the tooth. There are 4 types of test core segments:

- The first produced (#19) tooth that is not smoothed or machined
- Smoothed yoke surfaces, which are done for improving connectivity and adjusting outer radius of the assembled core segments, cause locally short circuited laminations
- Machined tooth surfaces, which are done for improving assemble of the core segments with winding segments, cause globally short circuited sides of the tooth
- First machined then blasted tooth surfaces are done for reducing the global short circuited surfaces due to machining

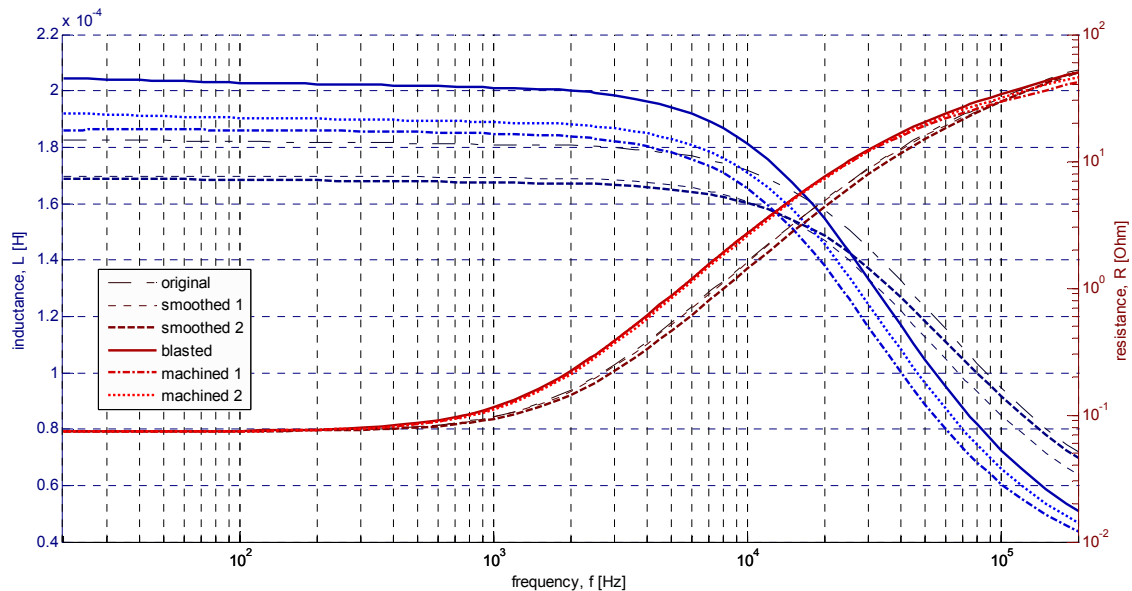


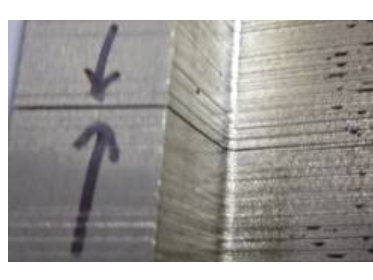
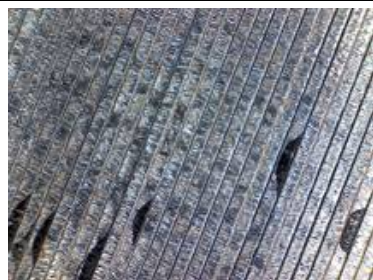




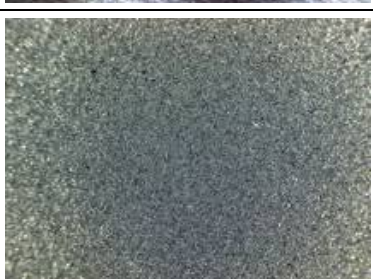
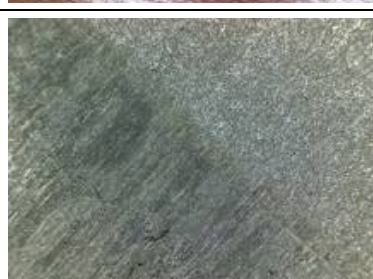


Figure 5.7 Impedance characteristics of the core segment after different manufacturing processes

The tooth surfaces are machined in order to proper assembling of the stator segment, which builds up a proper (outer) radius without yoke gaps. Initially the machining is applied to one tooth side only with the total cut depth of 0.2 mm. This core width reduction is partly applied to the inner surface of the yoke. This alteration is applied only on the (four) lateral core segments.

Table 5.6 Detailed views of the core surface

Description	Figure 1	Figure 2
<p>Two different batches of core segments:                      M270-35A (Fig 1)                      M250-35A (Fig 2)                      Figure focus on inner radius between yoke and tooth</p>		
<p>Improper gluing</p>		
<p>Close image of stator laminations</p>		
<p>Close image of stator (yoke) laminations where the surface is smoothed by slipping that has caused some local surface short-circuits between the laminations</p>		
<p>Close image of stator (tooth) laminations where the surface is smoothed by machining that has caused a global surface short-circuit between the laminations</p>		
<p>Close image of stator (yoke) laminations where the surface is smoothed by blasting that is used to reduce the global surface short-circuit between the laminations</p>		

#### 5.4 Assembling of stator segments

The assembling challenge is caused by the geometrical constrains that the outer radius of winding segment has tendency to be larger than specified and the inner radius of the yoke smaller than specified:  $R_{wo} \geq R_{yoke}$ . This discrepancy is due to lack of over bending that could count for the relaxation forces as well as slightly narrower core segments that shrink the radius for the assembled core. In specifications there is defined 0.5 mm space between the core segments and the winding segments. In practice there is no space for liner or the main insulation. For example, the core segments and winding segment comes into a visually perfect alignment. At the same time the ground or turn-to-turn insulation is not enough to guarantee the reliability of the main insulation. Insulation liner 0.18 mm Nomex 410 is used for the main insulation. Theoretically, 14 mm tooth width with 0.2 mm production tolerances (measured maximum 14.3) and 15.0 mm winding slot width with 0.2 mm production tolerances (measured minimum 14.8) leaves no space for the main insulation due to deviation from layer to layer. Practically, the lateral space between the winding and tooth is exact as the tooth is pressed into the slot with insulation without destroying the insulation. A dummy tooth is used to reinforce the insulation layer and guide the press fit of the core segments. The assembling of core segments is a forced slide in process that determines the angular position and radial position due to mate point between winding, insulation and core. Figure 5.8 shows the images from the geometric modeler where the ideal situation is compared with real conditions. Ideally the core segments are aligned so that the outer circumference builds up circle and there is a minimal air-gap between the core segments. Practically the lateral core segments of the stator segments are locked by the radial contact and their angular position is fixed by the tight connection. This results that air-gap between the core segments becomes around 0.5 mm and the outer radius becomes 1.5 mm larger. The middle core segment is located slightly lower compared to the lateral segments.

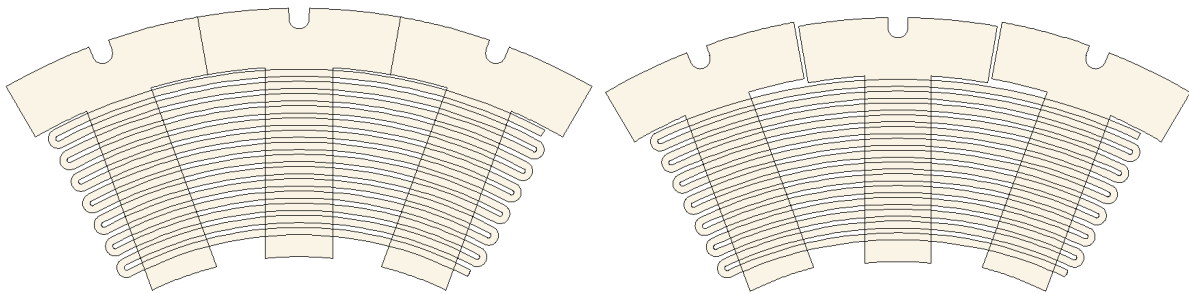


Figure 5.8 Ideal (left) and real (right) alignment of core segments in a winding segment

Figure 5.9 shows the assembled stator segments that are used in thermal tests and later in mechanical alignment tests (Table 5.7). Electrical tests are always followed the assembling experiments and discussed in chapter 6.

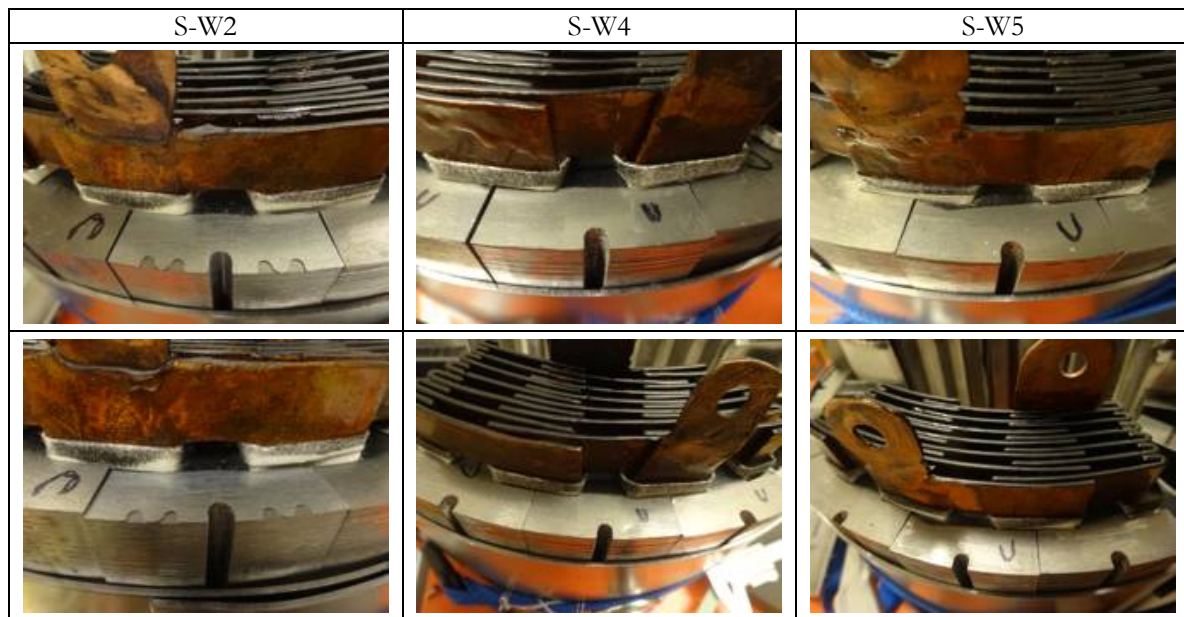


Figure 5.9 Assembled stator segments in prior to heat tests

The experimental assembling tests result some adjustments on the dimensions for winding outer layer, tooth width and yoke width. These changes are necessary in order to bring the core segments into the alignment so that they can be assembled into the housing cylinder. From the course of the machine design the tooth width is changed from 16 mm original, and 14 mm for easier production to 13.25 mm practical use. All this because the windings can be actually produced and assembled. The change of from 14 mm to 13.25 mm of the produced teeth is extended for 6 lateral stator segments.

Consequently, 3 windings out of 6 are used and 6 cores out of 18 are altered in order to maintain the assembling speed of the prototype machine. The housing cylinder, which have inner radius of 240 mm, increases about 1 mm during heating. The preassembled core-segments with winding suppose not exceed 240.5 mm for successful assembling.

Table 5.7 Detailed views of the assembling experiments



## 5.5 Assembling of stator

Figure 5.10 shows the first experimental and the final assembling of the stator segments. Figure 5.11 shows the stator before assembling the end shields and rotor and

Table 5.8 focuses on a few assembling steps during the final assembling.

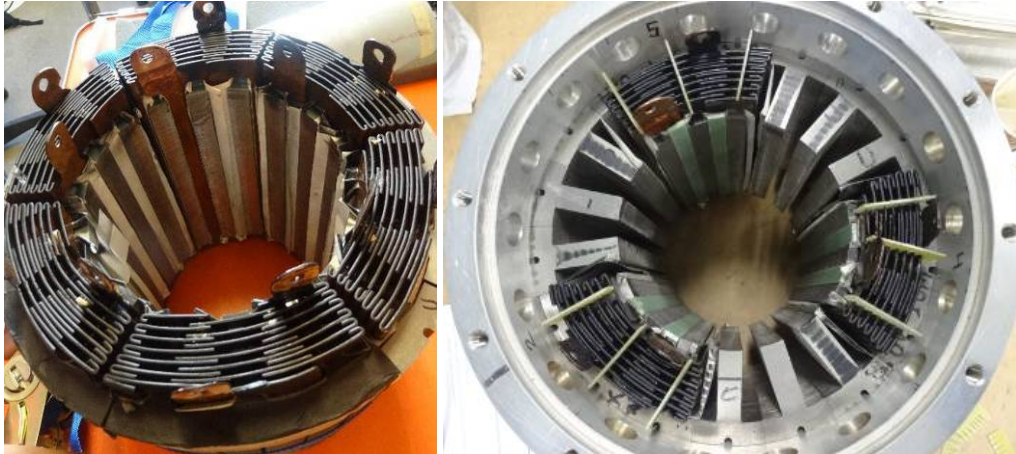


Figure 5.10 Stator assembly during the mounting tests (left) and after the final mounting (right)

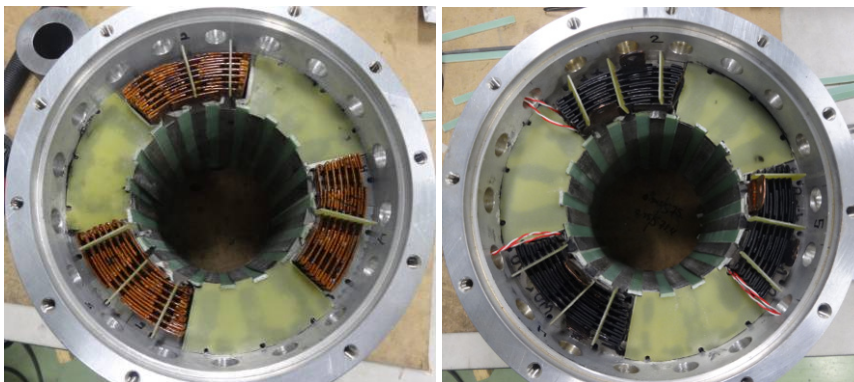


Figure 5.11 Drive end (DE) (left) and non drive end (NDE) of the prototype machine

Table 5.8 Detailed views of the assembled windings

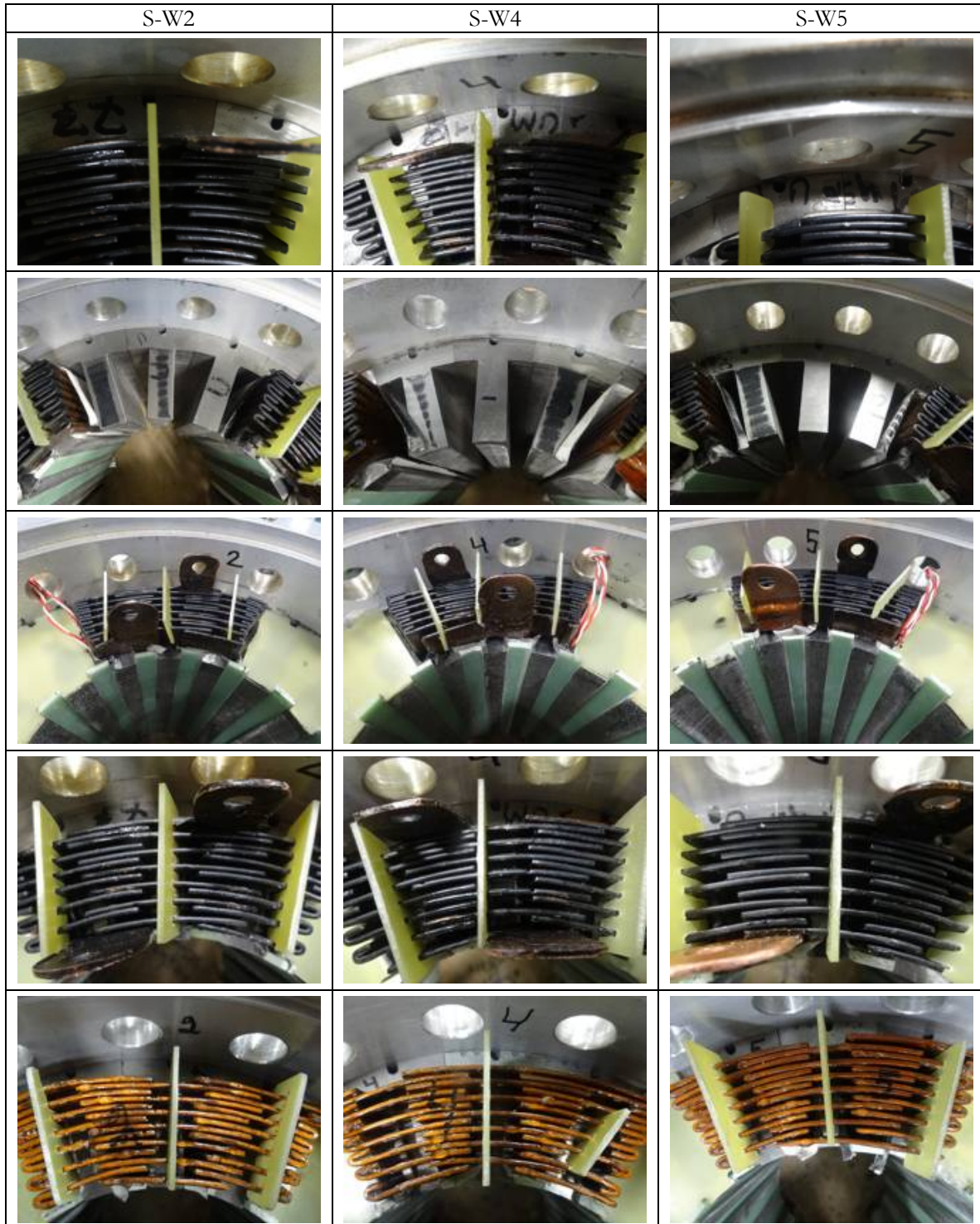


Table 5.8 shows the mounted stator segments (MS) with winding W2, W4 and W5 with the focus on:

1. the alignment and tiny gaps between the core segments,
2. the stator segments without the windings,



3. slot locks from the end-sides and the air-gap, wiring of temperature sensors
4. Coil displacement combs and the resulting cooling ducts at the terminal end and outlet side
5. Coil displacement combs and the resulting cooling ducts at the drive end and the inlet side

Some more observation and prototype data:

- Inner diameter of stator is 137.7 mm that is 0.15 mm less in radius than specified. At the same time the radius is 0.15 mm larger than in the original machine. The larger space is reserved for the production and assembling tolerances including the magnetic forces applied for the individual stator tooth that may cause larger discrepancy than it is initially expected. Additional observations, which are unfortunately exact measurements, are done for rolling rotor that have mechanic contact from one side and the double gap-length is measured from the other side.
- The inner diameter of the stator slot – yoke diameter is measured during the different manufacturing occasions, assembling tests and the final assembly, and the measured diameter is 215 and 216 mm, respectively.

## 6 Prototyping diagnostics

Design for manufacturability is basically a list of supporting guidelines for practical realization of the prototype. In the same way diagnostics for manufacturability supports the production, assembling and guaranties the functional quality for the prototype. The prototyping diagnostics is divided into three categories:

- E-tests: insulation check (Fluke 1587), RLC measurement (HM8118) and induced voltage during a rotation pulse (Textronics)
- M-tests: tolerance check of the components and subassemblies – mechanical adjustment for successful assembling
- H-tests: temperature records during heating and cooling tests – direct cooling of stator segments one by one

The E-tests that are regularly used during assembling are RLC and insulation measurements. The **main insulation** of the stator segments and complete stator is tested at the highest dc voltage  $1052\text{ V}$  that results insulation resistance  $2.2\text{ G}\Omega$  for the healthy winding (Figure 6.1). The test points are between phase and core and between phases. There are some occasional tests carried out at  $2.5\text{ kV}$  before and after assembling the stator segments into the stator housing. Usually the insulation check at  $1\text{ kV}$  is used regularly during the assembling the stator segments or experimenting on the final assembling of the segments into a complete stator. **LR and RC impedances** are measured over  $20\text{ Hz}-200\text{ kHz}$ . The winding impedance is measured at different points of assembling in order to quantify the changes and estimate the shortcoming. The special focus on the measurements is to detect any unaccepted changes or larger discrepancies between the windings, half or full assemblies of the stator segments. Furthermore, the course of the measurements facilitates the progress of validating the final assembly of the segments in the stator housing. Rotation pulse is an additional check for the completely assembled machine and this is used for evaluation of 3-phase emf, flux linkage and attenuation due to power losses and cogging.

The M-tests are used in parallel with E-tests during assembling. The main focus is on geometrically correct and healthy component or module that can be easily handled in the final stage of assembling – press fit due to thermal compression of the stator housing.

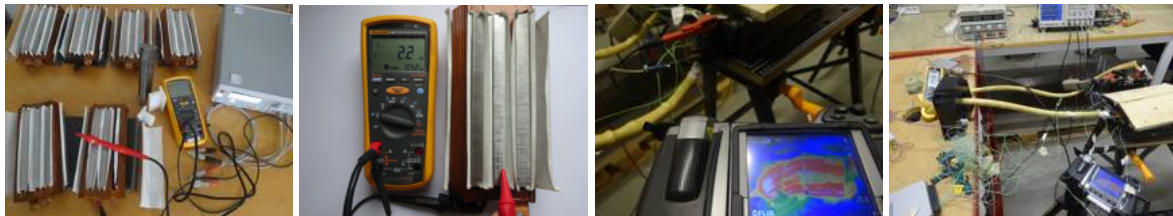


Figure 6.1 Inspection of stator segments by using RLC and insulation meter (left). Healthy insulation measurement (middle-left). Thermal image at the heat run (middle-right). Experimental setup for the thermal experiments (right).

### 6.1 Winding impedance

The winding (differential mode) impedance is referred as series RL circuit and measured with HM8118, The list of measurements follows the assembling process and includes the following:

- Horizontally placed and with large 15 cm space between the winding layers (Figure 6.2)
- Vertically placed winding with the defined distance ca 34 mm in total (Figure 6.3)
- Winding segment with the first stator segment mounted (Figure 6.4)
- Completed but mechanically not fine tuned stator segments (Figure 6.5)
- The first assembling tests of the stator segments (Figure 6.6)
- A number of follow up tests with mechanical refinement and larger compression (Figure 6.7)
- Ready made stator (Figure 6.8)
- Assembled machine before the machine tests (Figure 6.9)
- Assembled machine after the machine tests (Figure 6.10)

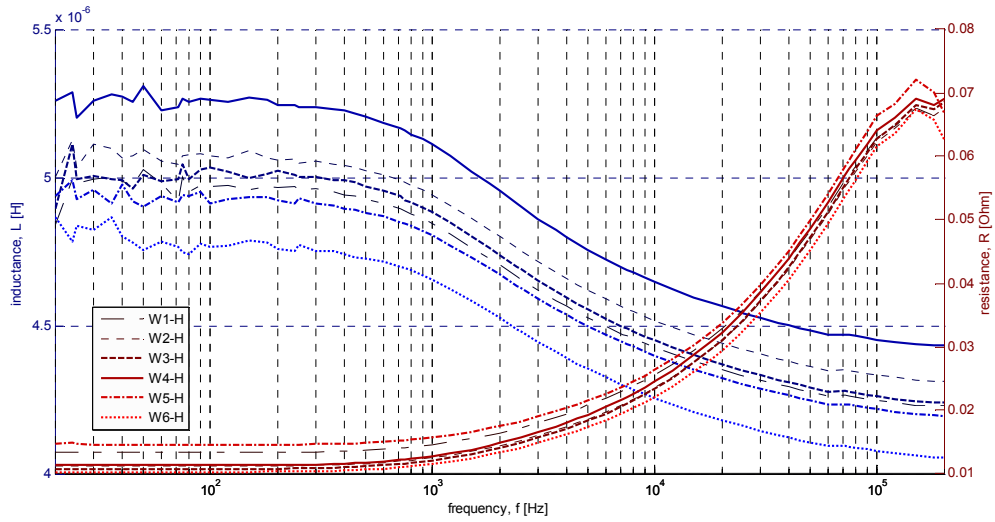


Figure 6.2 Resistance and inductance of horizontally placed spacey winding segments

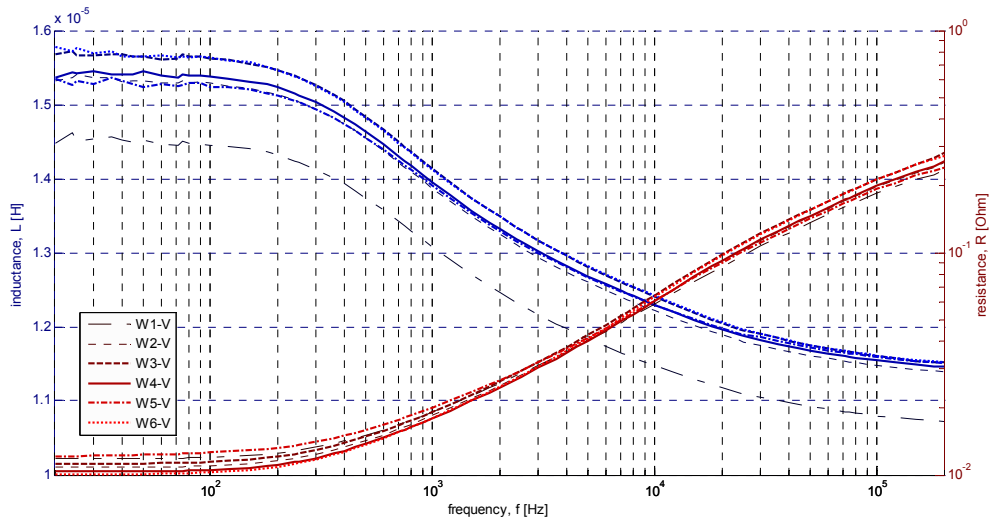


Figure 6.3 Resistance and inductance of vertically placed compact winding segments

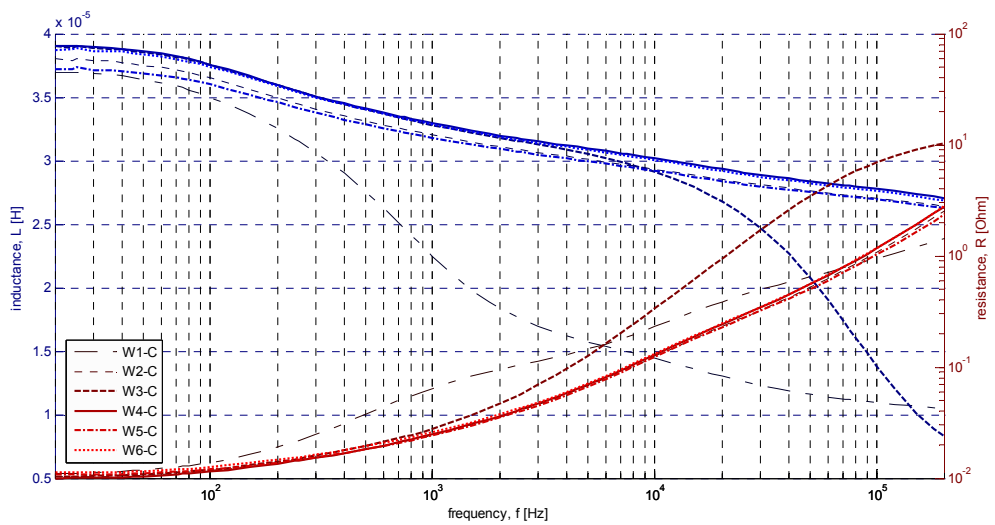


Figure 6.4 Resistance and inductance of winding segments with a single stator segment mounted

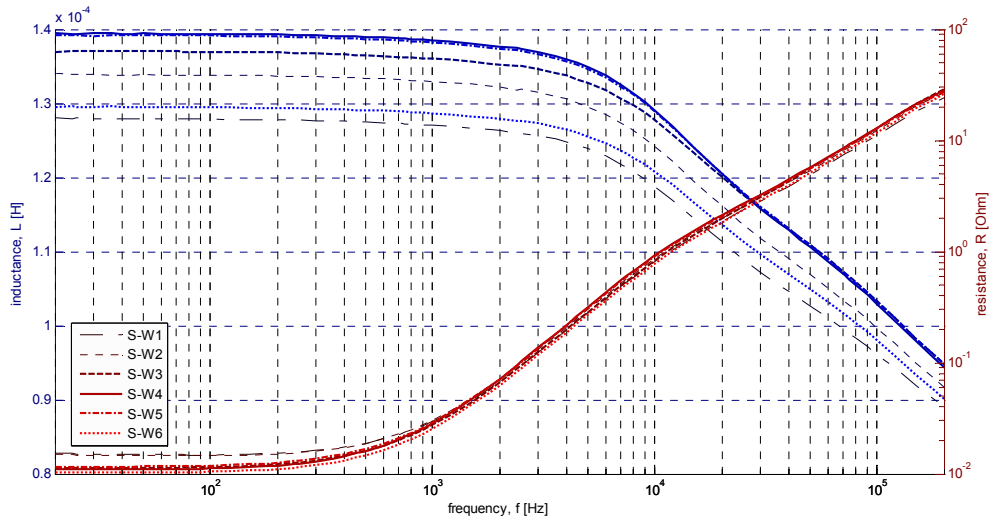


Figure 6.5 Resistance and inductance of winding segments with main insulation and core segments as independent units

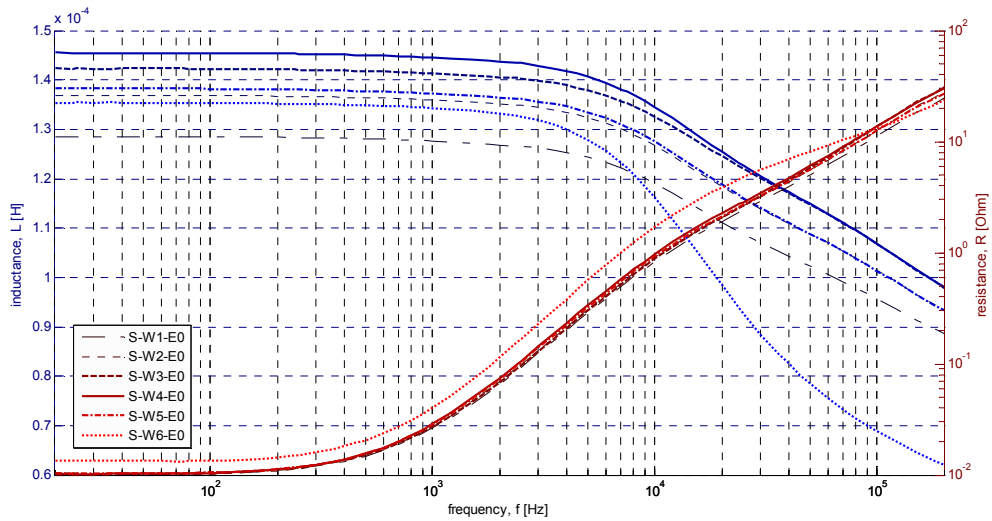


Figure 6.6 Resistance and inductance of winding segments with main insulation and core segments aligned up and compressed

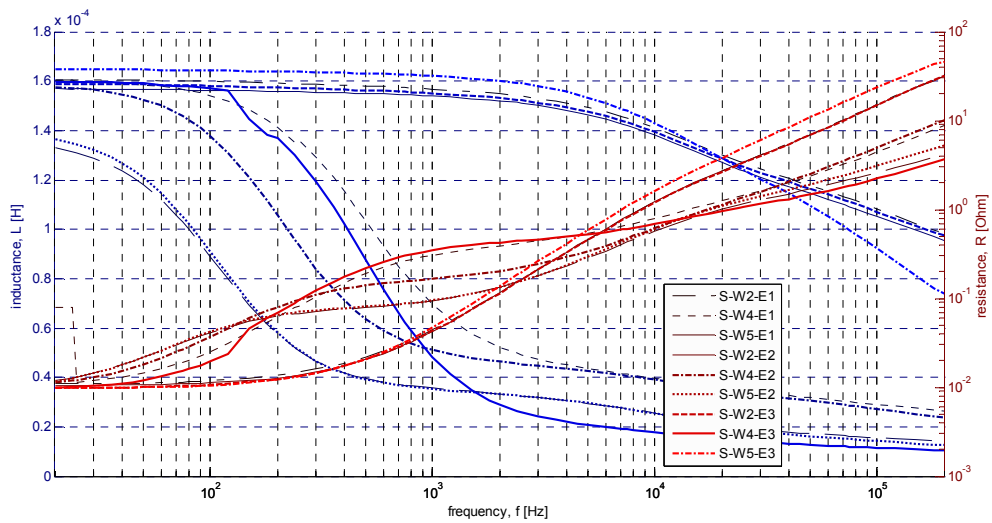


Figure 6.7 Resistance and inductance of selected winding segments with main insulation and core segments aligned up and compressed

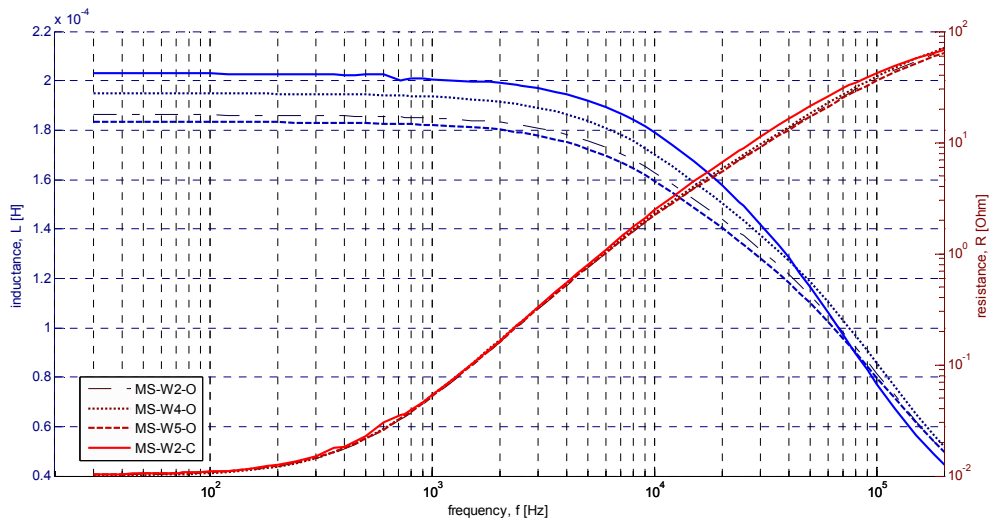


Figure 6.8 Resistance and inductance of selected winding segments inside the mounted stator

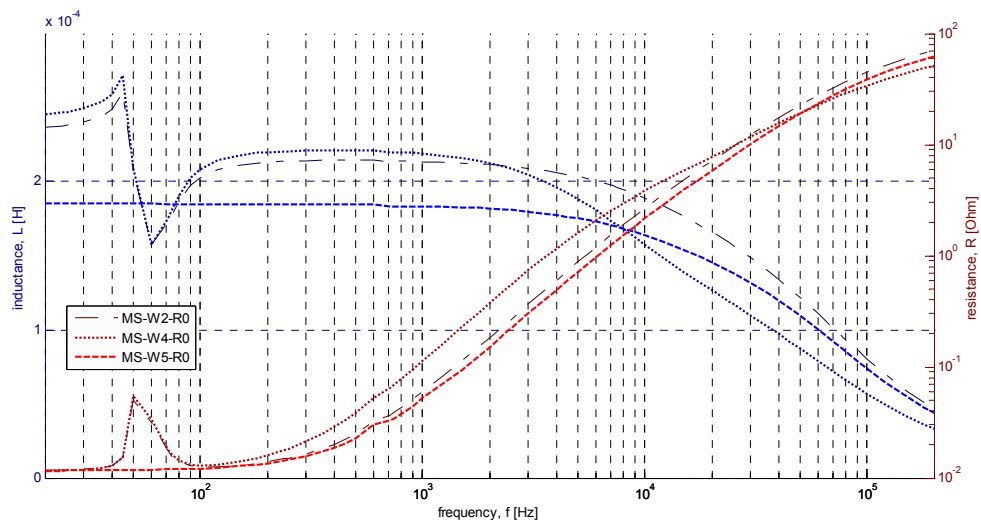


Figure 6.9 Resistance and inductance of selected winding segments inside the mounted stator with mounted rotor

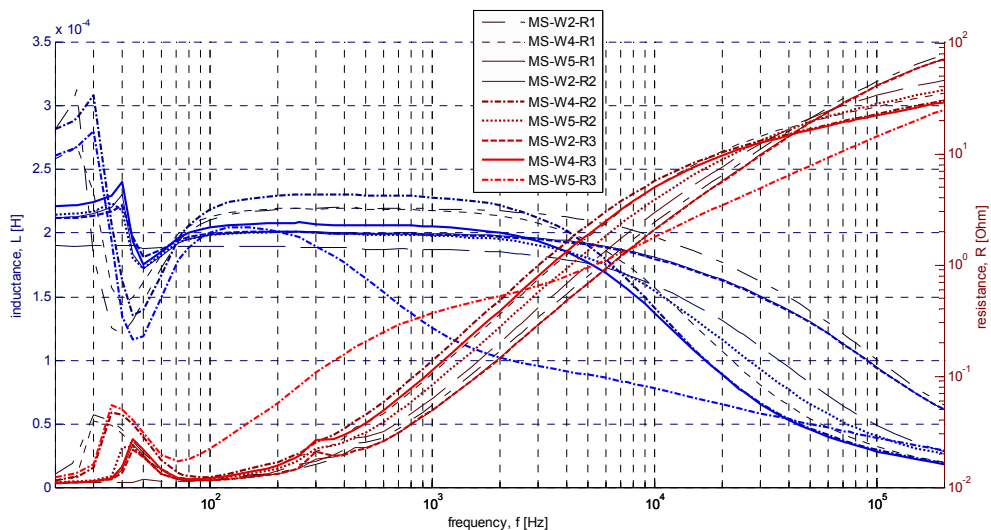


Figure 6.10 Resistance and inductance of the windings for three different rotor positions after the machine tests are finished

The winding impedance is followed after the main steps of manufacturing and assembling in order to detect unordinary characteristics or larger discrepancies between the winding segments. The measured winding impedance is comparable to the calculated one (Figure 6.11). The results agree pretty well up to 10kHz when the measured impedance turns has a higher decrease in inductance and increase in resistance.

The end turns are not included and this can explain the small difference between inductance and resistance at low frequency region.

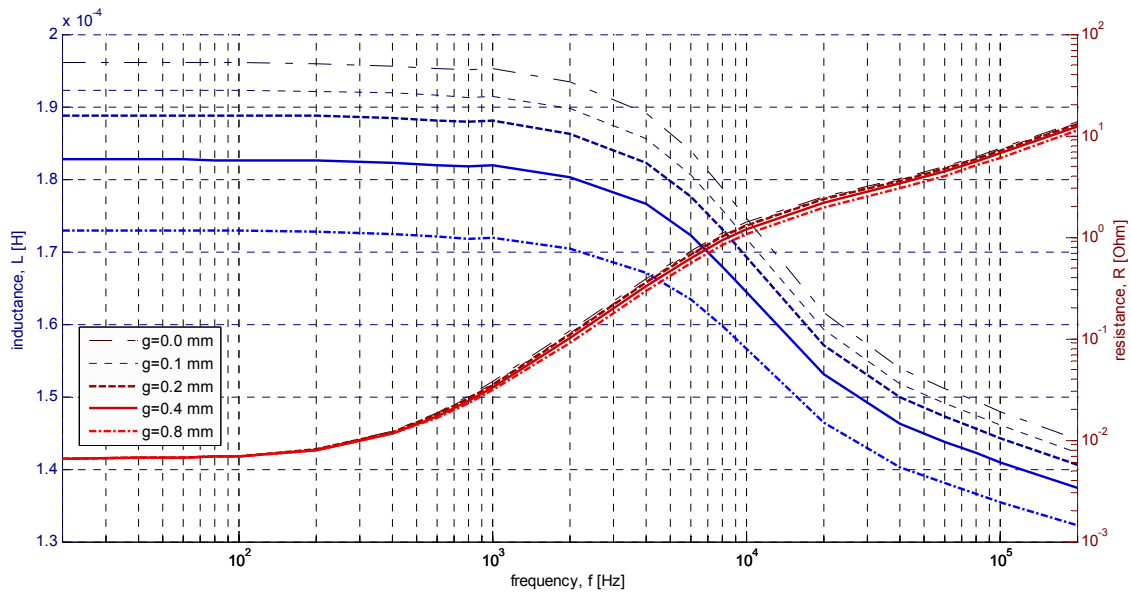


Figure 6.11 Calculated resistance and inductance (Table 4.2) as a function of lateral air-gap between the core segments

The winding to ground (common mode) impedance is referred as parallel RC circuit and shown in Figure 6.12.

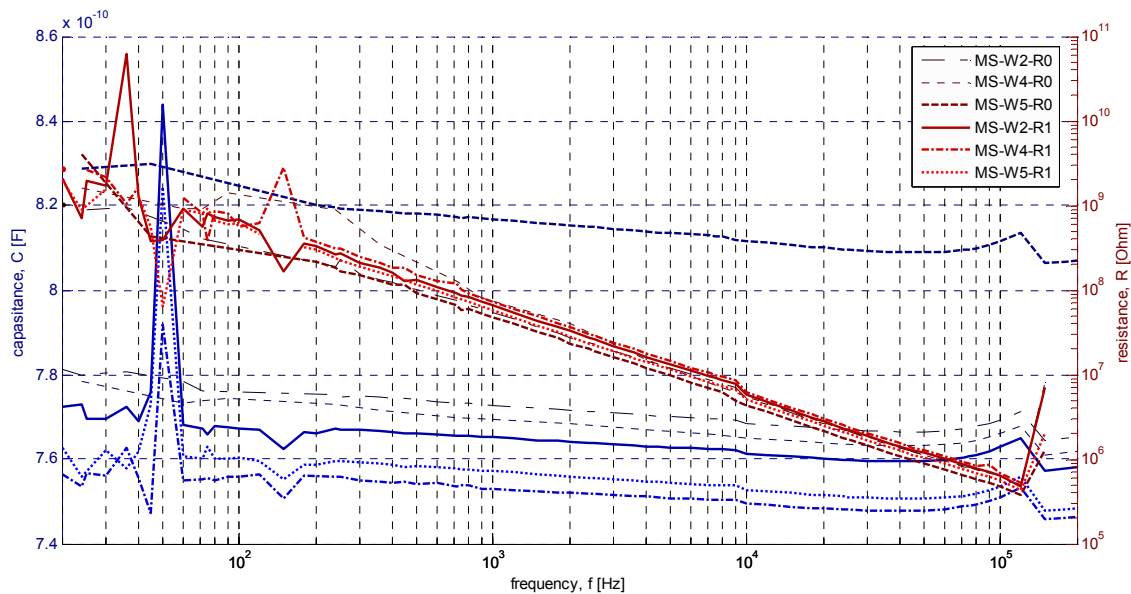


Figure 6.12 Winding to ground capacitance and resistance before (R0) and after (R1) the machine tests.

## 6.2 Insulation strength

Insulation strength is regularly tested with insulation tester Fluke 1587 and the insulation faults are fixed directly once they are detected. Even a small hole in slot insulation can be detected in this way.

## 6.3 Thermal load test

The thermal load tests are carried out at the following order W5-W2-W1-W6-W4-W3. Since the stator segment that accommodates winding segment W5 is assembled first, this winding is tested more than any other segments. Different spacing for the winding layers is tested for segment W5 and the best implemented for the others. The outlet and inlet of the stator segments is shown in Table 6.1 and thermal records in Table 6.2.

Table 6.1 Outlet-side and inlet side of the stator segments







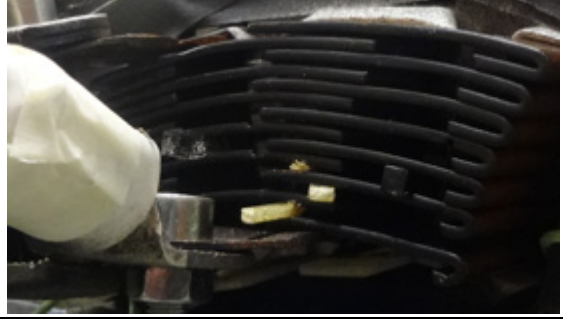

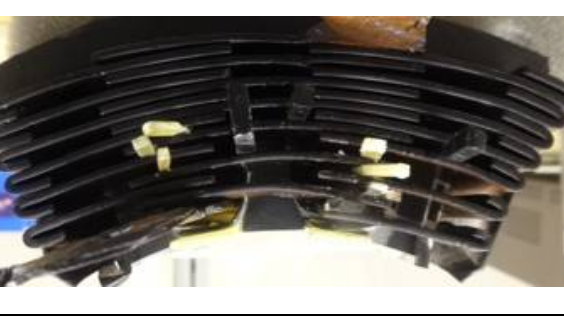
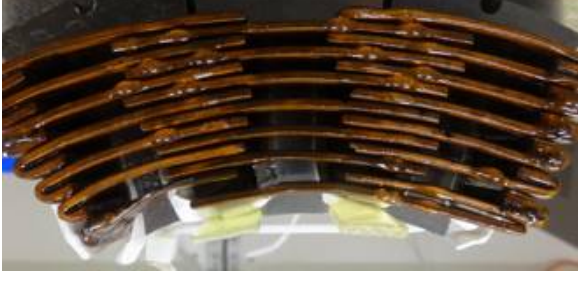
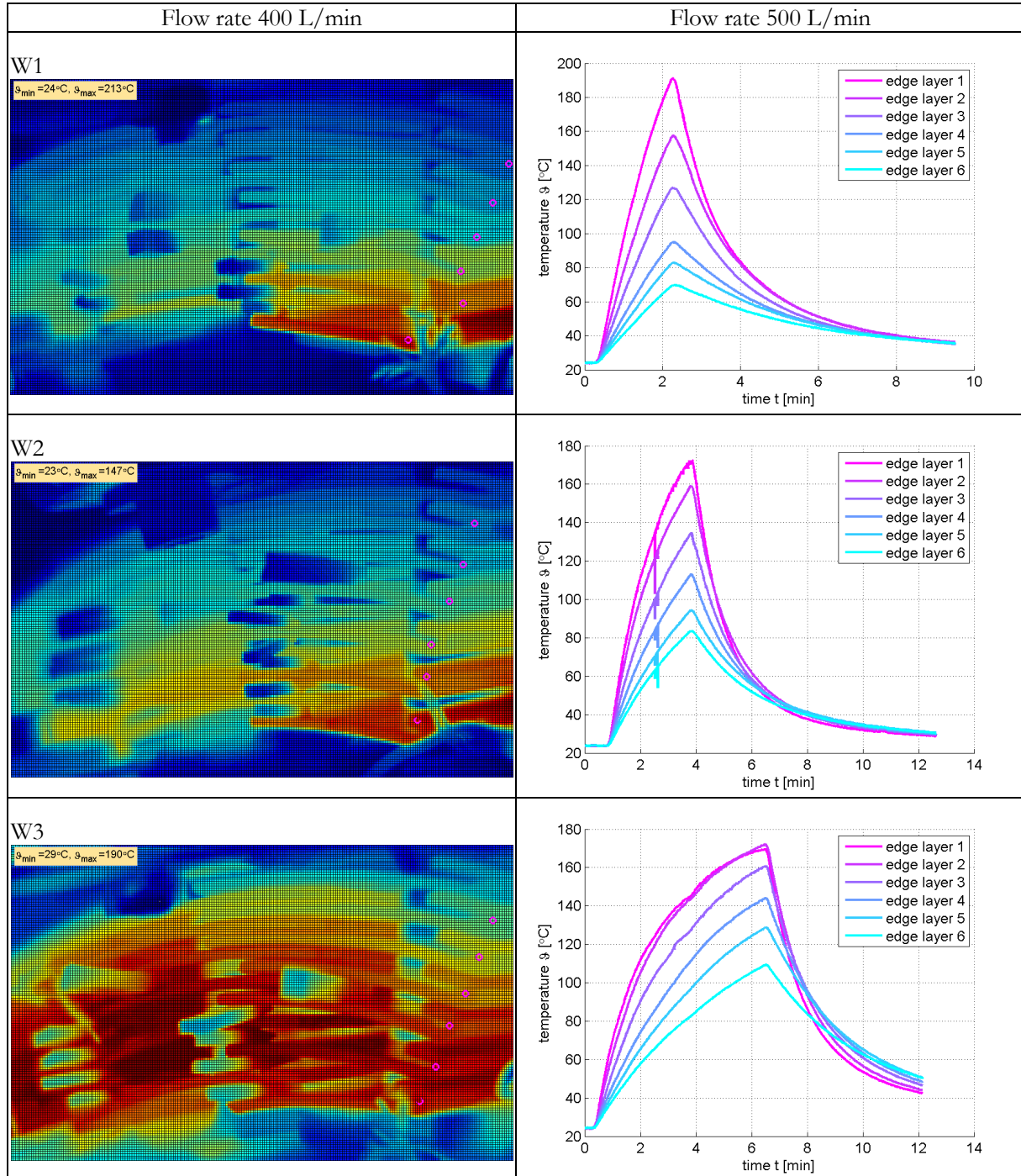
Outlet – Terminal-End	Inlet – Non-Terminal-End
	
	
	
	
	

Table 6.1 shows the outlet and the inlet side of the stator segments. Each row in this table corresponds to one stator segment that hoses the corresponding winding from W1 to W6 unless W5 that is in Figure 1.7.

All the winding segments are arranged so that the cooling channels are wider closer to the air-gap (inner turns) where more cooling is needed due to the smaller cross section of the winding and the expected hot spot regions. The windings are tested at constant current where the temperature dependent voltage drop is compensated by step wise action of the auto transformer in the primary side of the supply transformer.

Table 6.2 Infrared image at the maximum heating point before the current is disconnected





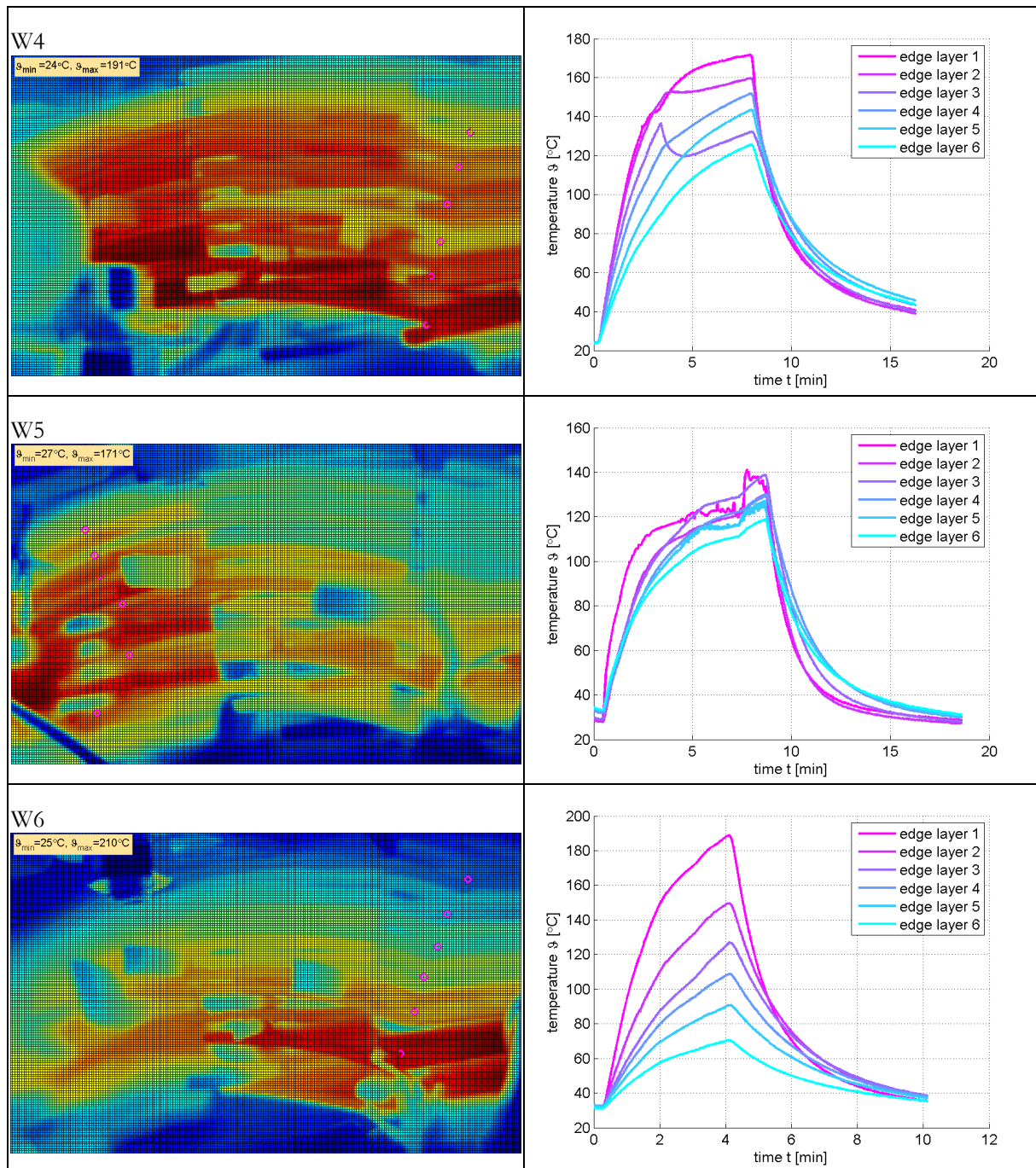


Table 6.2 shows the temperature image of the stator segments straight before the load current of 300 A is disconnected. Each row in this table corresponds to one stator segment with winding from W1 to W6. The temperature records are collected from the IR image and the collection points are marked with a pink circle on the IR image.

The primary purposes of the H-tests are evaluating the forced cooling capability of a directly cooled machine windings and experimenting on possible improvements to control the hotspot temperature by a small structural changes. Secondly the experimental work gives good insight for further development of the measurement methods, supplementary arrangements of the test system and not least better understanding on heat transfer in the winding structures.

The experiments indicate that the stator segments have rather different peak current capability for the selected hot spot temperature and coolant flow rate. This is rather natural as the discrepancy between the winding geometries and cooling ducts can easily result overheated and non cooled regions. In addition to the IR image the test sample - winding segment in a stator segment has a number of thermocouples

attached to the potentially overheated regions. Figure 6.13 gives rather good overview of the test where the supply of electric current and coolant flow, heating time and temperature development during heating and cooling is presented. The thermograph analysis and IR image processing could give good possibility on heat transfer analysis and the heating and cooling intensity in different regions. As it is right now only the maximum temperature of the available temperature sensors are presented. The maximum temperature is usually at the inner turn. Here is no additional heating efficiency analysis based on supplied active electric power versus the extracted heating power of the temperature rise in the coolant.

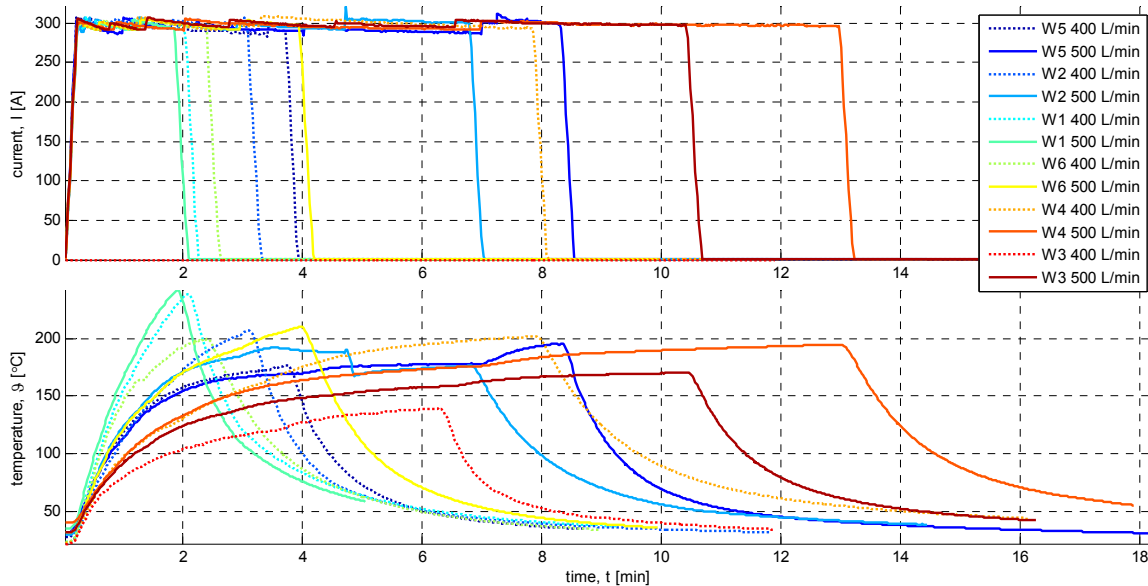


Figure 6.13 Supply current and selected temperature curve that reaches to the highest temperature during the test

Out of these thermal experiments the most potential windings are selected that allows building the machine in a limited amount of time. The time restriction set aside 3 windings out of 6 in order to advance the prototyping. W2, W4 and W5 is selected for continuation due to

- winding hotspot geometry,
- ability to mount the winding segment,
- actual cooling capability

#### 6.4 Mountability

The mechanical assembling on how the winding segments accommodate insulation and core segments and how the stator segments are mounted together is the main subject for M-tests. The core segments have tendency to have a lower yoke radius due to manufacturing tolerances of the segments due to laser cutting and stacking but also due to the machined surfaces of the stator yoke.

#### 6.5 Roto-pulse

A short rotation pulse is given to the rotor shaft in order to record the induced voltage waveforms with an oscilloscope. At first hand the waveforms are observed for evaluating the three phase symmetry and attenuation speed due to internal power losses. This data can be numerically analyzed for acquainting more information about the machine.

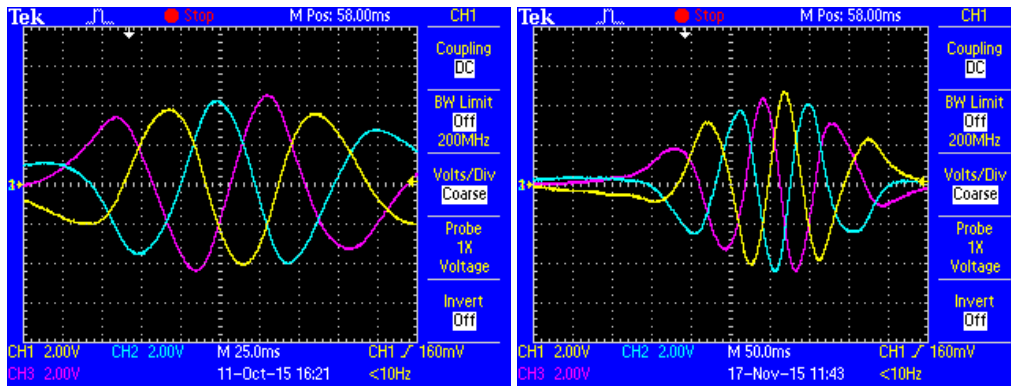


Figure 6.14 Recorded induced voltage waveforms during rotation pulse before machine tests (left) and after tests (right)

## 7 Machine tests

The list of experiments are made after the test machine is rigged to test bench

- No load emf @ 100, 1000, 2000 rpm
- No load power losses & winding temperatures 100-2300 rpm & 1000-6000 rpm
- On load tests at low speed @ 100 rpm,  $U_{dc}=600V$
- Short-circuit tests @ 2.5-3.5krpm &  $1.0m^3/min$  and 3.5-4.5krpm &  $1.5m^3/min$

Machine tests are the main focus on speed, torque and cooling capabilities rather than power capability

### 7.1 Machine test set-up

The experimentation speed is given and maintained by the rotating prime mover and the applied torque is measured by torque transducer. This applied torque is caused by power losses, accelerating torque or braking torque of the test machine. So the primary interest is to follow current, torque, speed, coolant flow and the temperature development of the different tests.

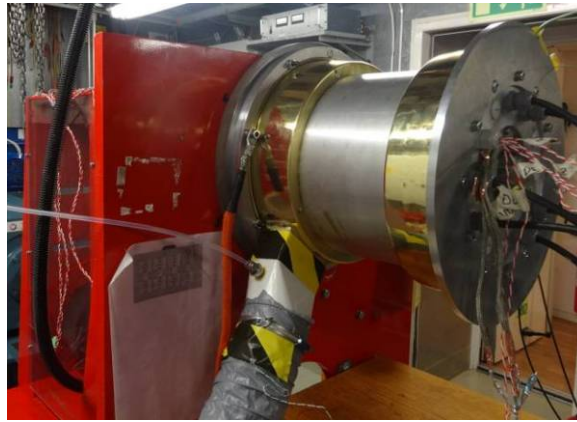


Figure 7.1 Test machine rigged onto the test bench

The coolant flow is not regulated rather than set to particular level. The pressure sensor does not match the measurement range and therefore there is no more efforts applying on flow analysis.

Precision power analyzer is used to acquaint the electric power flow from the three phase converter to machine or backwards. The only drawback is that not all important data is recorded over the course of experiment and this either cause difficulties on carrying out comprehensible discussion, conclusions and experimental confirmations.

The temperature measurement of the closed system becomes a challenge where the wide range of temperatures is expected and a very few of them are measured. Therefore the locations of the temperature sensors are vital not only for the consistent general conclusions but also for safety when testing the limits for the prototype machine.

#### Temperature sensors

There are 2 sensors per coil that are placed on the conductor that has the smallest cross-section area and approximately 20 mm from the edge of the stator tooth. There are 3 sensors used to measure the outlet temperature, 1 for inlet temperature, 1 for room temperature and 1 is placed into the housing hole that is used to measure the yoke temperature. Table 7.1 lists all the sensors, their location and data stream name that are later plotted as the outcomes of the experiments. Figure 7.2 visualizes the location for some of the temperature sensors.

Table 7.1 List of temperature sensors that data is presented later

Sensor	W2NDE	W2DE	W4NDE	W4DE	W5NDE	W5DE	AMB	core	out1	out2
Object	Winding 2	Winding 2	Winding 4	Winding 4	Winding 5	Winding 5	room	case/core	outlet	outlet
Location	NDE	NDE	NDE	NDE	NDE	NDE		Figure 7.2	Figure 7.2	Figure 7.2
data	actMT1	actMT1	WND-01	WND-02	WND-03	WND-04	AMB	TC-INV1	WND-06	TC-EM1

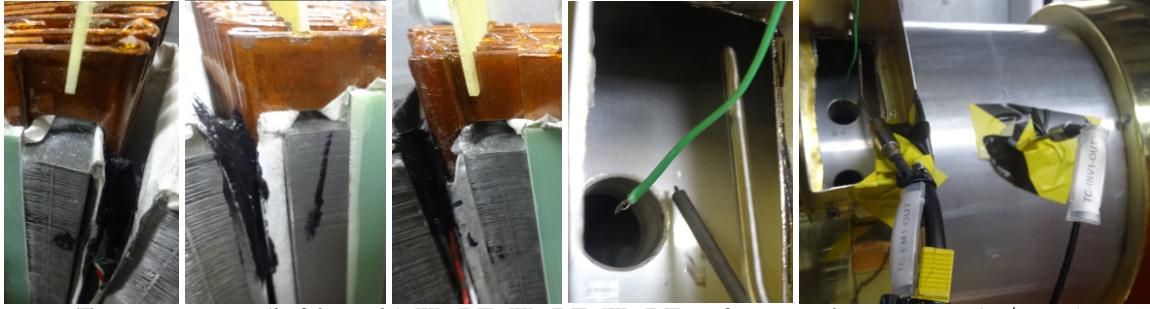


Figure 7.2 Temperature sensors (fro left to right): W2-DE, W4-DE, W5-DE, outlet sensors after experiments (22/10-15) and sensor placed behind the stator core.

## 7.2 No-load open circuit tests

Back emf is measured at 0.1, 1 & 2 krpm and these waveforms are integrated in order to obtain the magnetic flux linkage (Figure 7.3). The peak flux linkage  $\Psi_m$  per phase is **59.8**, **59.9** & **59.6 mVs** and this agrees well with FEM calculations (Figure 3.7) where the peak value of the flux linkage **59.3 mVs** for the machine with 3 winding segments out of 6. The comparison of flux linkage values shows insignificant flux linkage reduction due to speed and point out symmetric 3-phase system with low THD (Table 7.2).

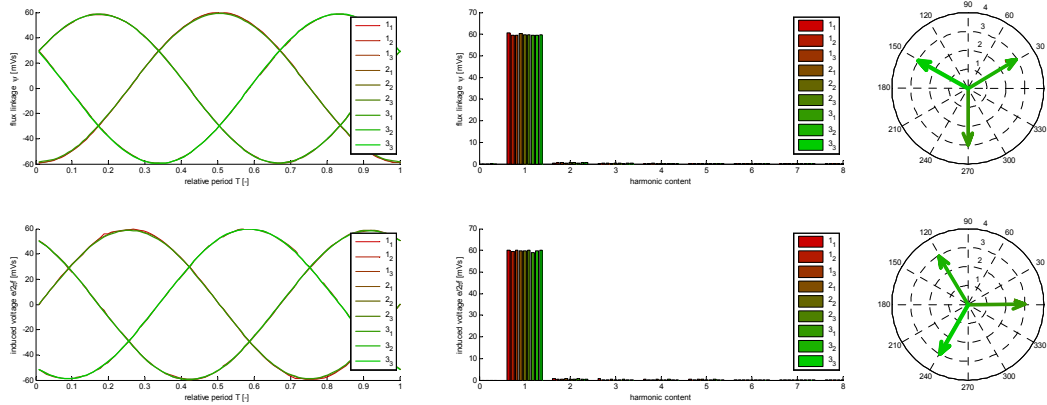


Figure 7.3 Measured induced voltage waveforms (upper left), spectrum (upper middle) and phasors (upper right) divided by rotation speed at 100, 1000 and 2000 rpm. Lower graphs are presenting the corresponding flux linkage that is integrated from the measured induced voltages.

Table 7.2 Analysis of induced voltage waveforms.

speed-phase	$\Psi_m$ mVs	$\Psi_{eff}$ mVs	$\Psi_{thd}$ %	$E_m$ mVs	$E_{eff}$ mVs	$E_{thd}$ %	f,Hz
1-1	60.53	42.38	0.0	59.93	41.96	0.0	13.6
1-2	59.39	41.58	0.0	59.62	41.75	0.0	13.6
1-3	59.55	41.69	0.0	60.18	42.14	0.0	13.6
2-1	60.30	42.22	0.0	59.72	41.82	0.0	133.3
2-2	59.66	41.78	0.0	59.89	41.93	0.0	133.3
2-3	59.69	41.80	0.0	59.95	41.98	0.0	133.3
3-1	59.59	41.72	0.0	59.00	41.32	0.0	267.0
3-2	59.48	41.65	0.0	59.65	41.76	0.0	267.0
3-3	59.87	41.92	0.0	60.06	42.05	0.0	267.0

The no load losses of the prototype machine is measured over two different speed range. The torque-speed and power-speed diagrams are shown in Figure 7.4. Figure 7.5 shows the temperature records of these two tests. There are two selected references and their theoretical model based confirmations

- Speed 1500 rpm results 543.3 W power loss ( $P_{core}=176.8W$ ,  $P_{win}=68.1W$ ,  $P_{pr1}=42W$ )
- Speed 3000 rpm results 1671 W power loss ( $P_{core}=385.6W$ ,  $P_{win}=290.4W$ ,  $P_{pr1}=129.2W$ )

The comparison of the measured power losses in the core is considerably larger than the expected. The estimation covers only core losses, the induced losses in the short-circuited surfaces of the stator segments, and the induced losses in the windings due to rotation. The power loss estimation does not cover induced losses in the stator housing or in the core due to misalignment of laminations between the different segments. The influence of the global surface short circuit on the tooth surface of the lateral core segments is not considered either. Apart from that the electromagnetic losses in the rotor, mechanical losses in the bearings and air-drag are not included in the power loss analysis.

Figure 7.4 visualizes the measured operation points at torque speed and power speed plane when the rotation speed of the idling test machine is increased from  $100$  to  $2300$  rpm and thereafter from  $1000$  to  $6000$  rpm. All the measurement points in this speed range are polynomial curve fitted and the roots of the two lines are shown on the figure legend box. Figure 7.5 shows the temperature records of the no load experiments. There is only winding temperature available from the data logs.

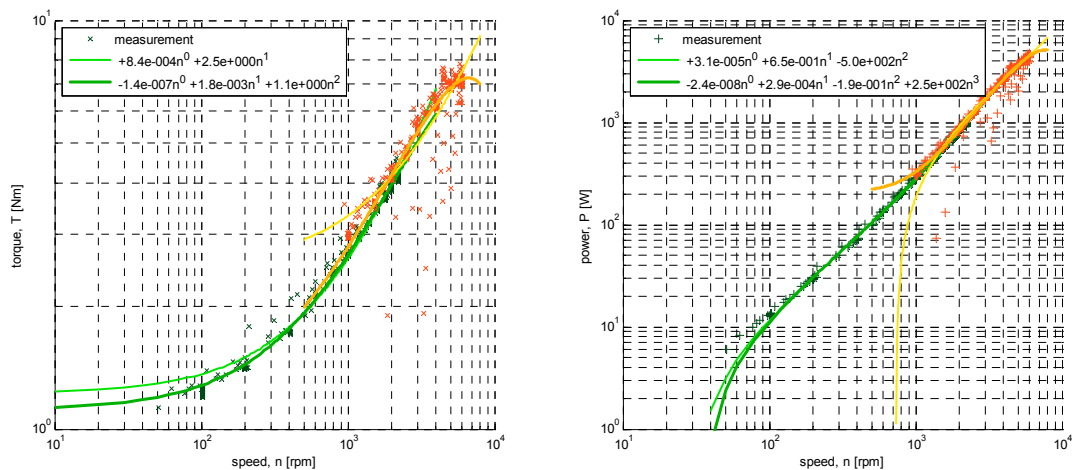


Figure 7.4 Internal load torque as a function of speed (left) and no-load power losses as a function of speed (right)

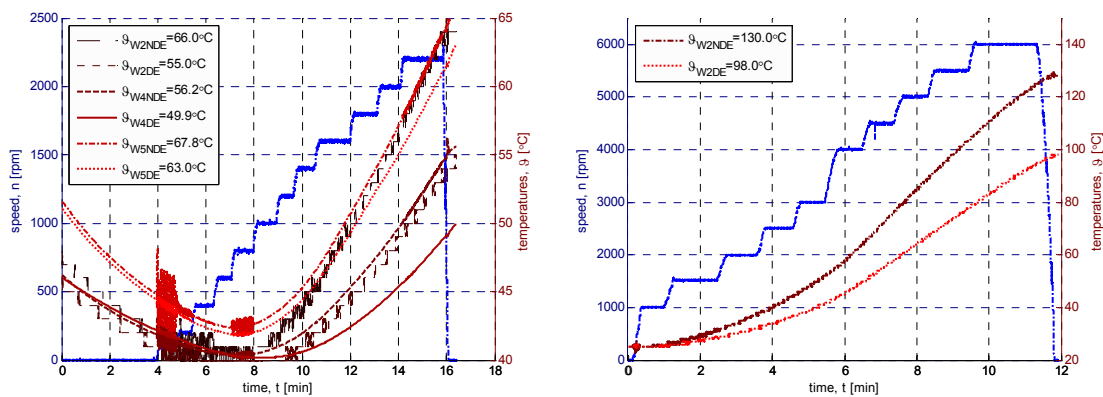


Figure 7.5 Temperature development during the no-load tests

### 7.3 On-load tests

The test machine is fed from the inverter with  $U_{dc}=600V$  and the load machine maintains the rotation speed  $100$  rpm. The air-coolant flow is set to  $1500$  L/min. The applied current is kept orthogonal to the field. The magnitude of the current is increased gradually until the failure is detected from the inverter control. Figure 7.6 shows the time functions of torque and voltages of four different test cycles. The same experiments are plotted as a function of stator current when focusing on torque to current ratio and low speed efficiency (Figure 7.7). Table 7.3 presents the calculated values of the torque to current ratio for 14 mm wide teeth and electromagnetic (source) torque only excluding the internal torque loss. Figure 7.8 and Figure 7.9 present the temperature records of the experiments.

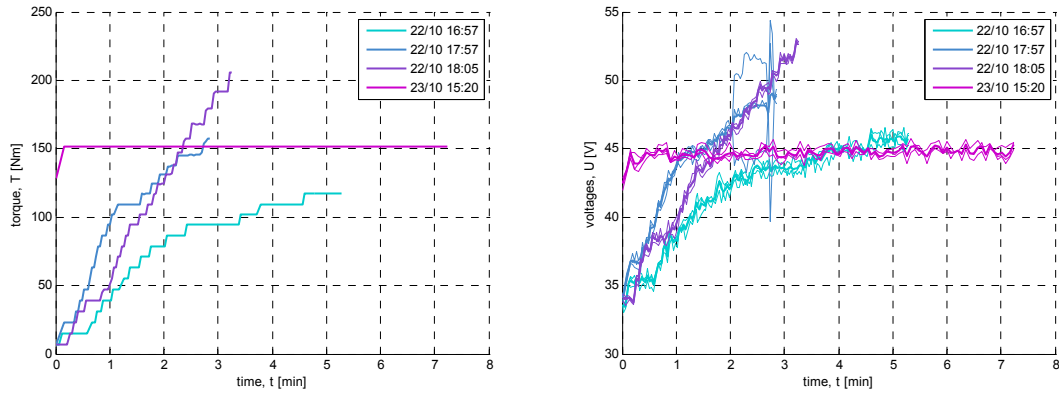


Figure 7.6 Machine torque (left) and voltages (right) at on-load tests

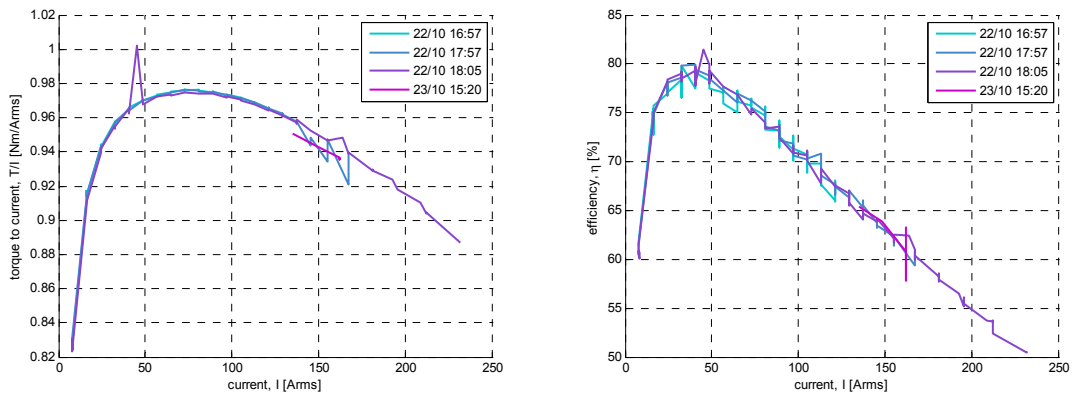


Figure 7.7 Torque to current ratio (left) and machine efficiency (right)

Table 7.3 Calculated torque to current relationship

Stator current Irms, [A]	141	282	424
Electromagnetic torque (no losses) Tem, [Nm]	140	244	304
Torque to current ratio, T/I, [Nm/A]	0.99	0.86	0.71

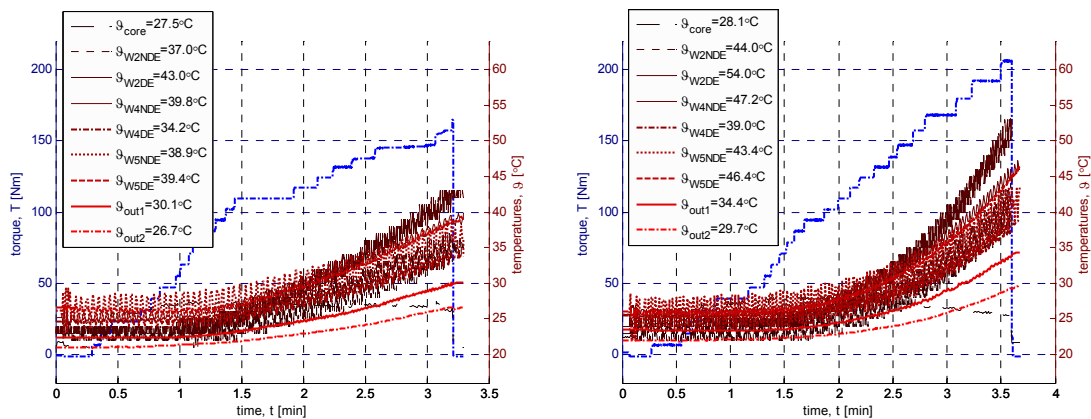


Figure 7.8 Temperature logs of load tests 22/10-17:57 (left) and 22/10-18:05 (right)

The inlet temperature of the load tests is 20.4°C and ambient temperature 21.5°C (Figure 7.8). By referring to the last measurement points of these two records the temperature rise across the inlet and the first outlet is 9.7°C and 14°C, respectively. By referring to air temperatures of 25°C and 30°C the extracted heat power at 1500 L./min becomes 288 and 409 W. The series resistance of the windings at low frequency according to impedance measurements is 30.8mΩ (Figure 6.8). The phase current of 170 and 230 A rms brings the heating power up to 890 and 1629 W. At this part of thermal transient when the winding temperature is relatively low, which is below 55°C, the directly cooled power is 3 – 4 times

smaller than the heating power. Basically the temperature difference across the winding inlet and outlet supposes to be at least 3 – 4 times larger that the heating and cooling power comes into to balance.

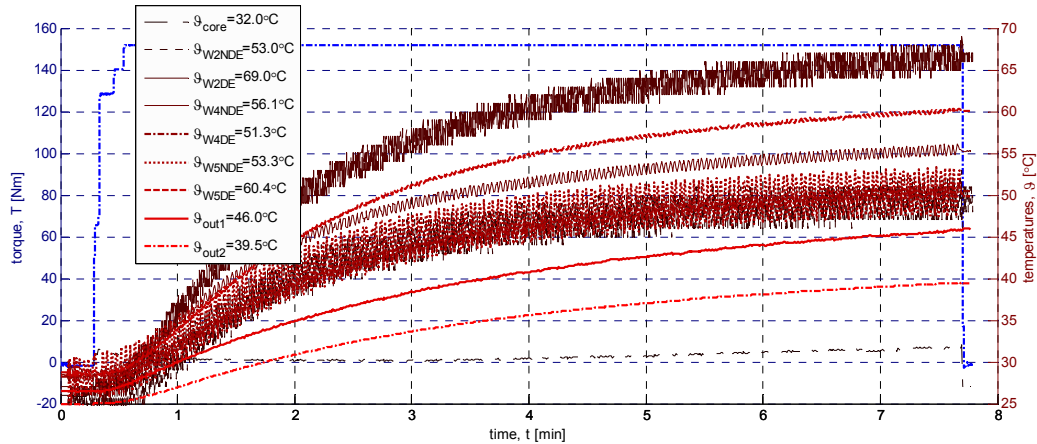


Figure 7.9 Temperature logs of load test (23/10 15:20)

The next experiment (Figure 7.9), which is made at the average inlet temperature of 21.6°C and ambient temperature 24.1°C, shows the temperature development reaching to the steady state. The increase of coolant temperature is 24.4°C which at the average coolant temperature of 35°C is able to dissipate 701 W while 150 Nm requires 160 Arms and this generates 789 W for heating power. The heating cycle is nearly 8 minutes long and it is expected that within 10-12 minutes the temperature development reaches to the steady state. The hotspot temperature of the winding remains below 70°C. The outlet temperature is below 50°C. The doubled current, which becomes nearly 300A as a peak current, requires 4 times more cooling power. The increase of temperature difference by factor of 4 could bring the outlet temperature beyond the expected 120°C. Theoretically it is expected that leak free direct-cooling, which is more than 4000 L/min for whole machine keeps the temperature rise along the channel 100°C and across the wall below 30°C so that 20°C inlet temperature keeps the hotspot temperature under 150°C. The theoretical analysis declares clearly that this rough temperature chart is not valid for overheated under-cooled winding regions where the cross-section for the current is small and also the cooling area is small. Theoretically the hotspot temperature shall not exceed 180°C at peak operation and specified cooling [8]. So far the prototype shows expected temperatures along the channel and across the channels wall at lower flow rate and leakage. Anyway the focus of the work is not to verify the amount of heat stored to coolant for a given temperature rise rather than construction analysis from functionality and safety point of view. From hot spot temperature point of view, the critical areas are known and the temperature sensors are placed near to the (hot) spot. The measurement result is expected according to calculations. Safety of the winding and winding assembly leaves the space for improvements. Sharp edges and close distances have not been detected as a problem during the prototyping diagnostics due to limited measurement range of intense alternating fields. As it is learned from the experiments the sharp edges of termination and surrounding construction has caused flashover and failure that is detected by inverter control (Figure 7.10).



Figure 7.10 Flashover winding (W2) end (NDE or TE)



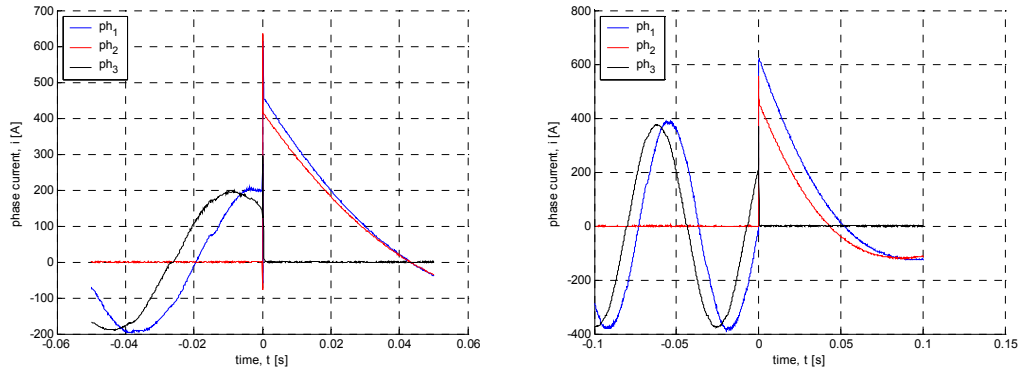


Figure 7.11 Phase current logs on W2-flashover detection

Figure 7.11 shows two measurements of the phase currents while detecting the flashover of winding W2.

### 7.4 Short-circuit tests

As the load test were limited by the partial discharge effects from the terminal to the interior construction edge of the shield (Figure 7.10) the load test were rather limited for thermal assessment. Therefore short circuit tests have been made at increased levels of rotation speed until the temperature development has reached to steady state. There are three records from the short circuit tests

- First run first half (L138) and second half (L139) (d343)
- Second run (L140) (d851)

#### First run

The initial air flow is 0 L/min. The rotation speed is brought from 0 to 1000 rpm within an half of minute. The highest change of winding temperature is from 55°C to 162°C during 7 minutes before the flow rate is increased to 1000 L/min. During next 20 minutes the hottest temperatures at non-drive end stabilize at 96-99°C. The rotation speed is changed from 1000 rpm to 1500 rpm and after 10 minutes the corresponding temperatures are 101-106.6°C and 40 minutes later 103-108.9°C.

In continuation the rotation speed is changed from 1500 rpm to 2500 rpm and from 2500 rpm to 3500 rpm. The lengths of both runs are approximately 30 minutes.

Figure 7.12 shows the temperature development during the first run and Figure 7.13 shows speed, current and repetition of temperatures as a function of time. This data comes from the other data source and is not integrated to the same graph.

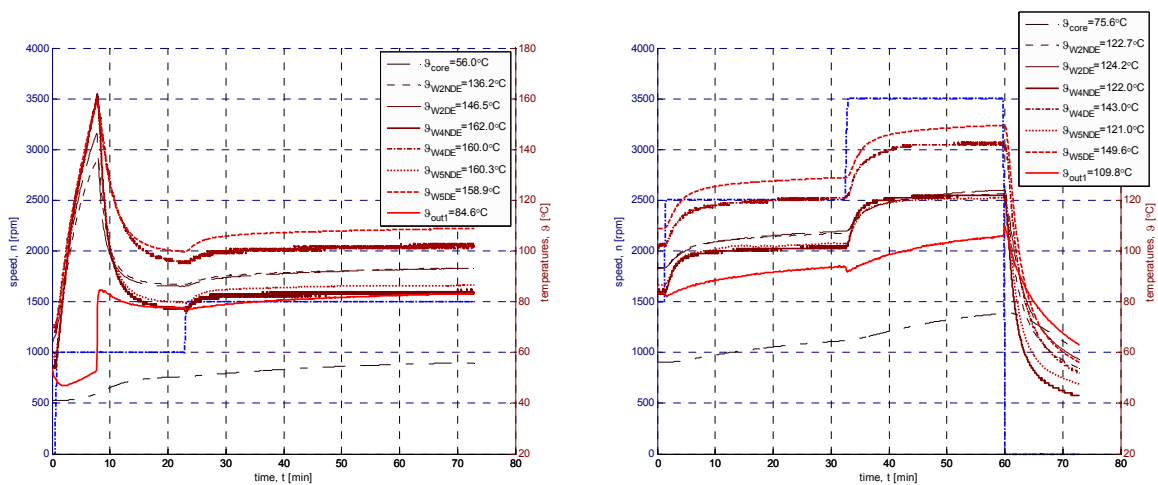


Figure 7.12 Temperature logs of load tests

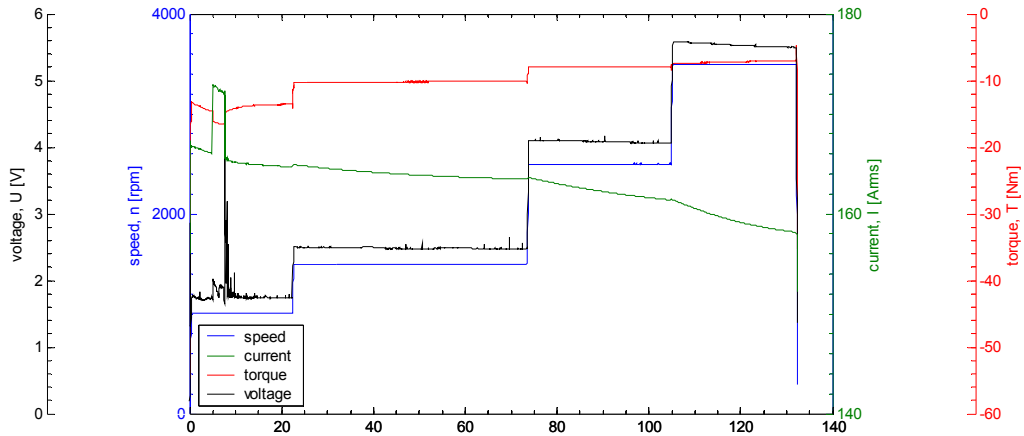


Figure 7.13 Data records from the other source showing the speed, voltage, current and torque of the first run.

### Second run

The initial air flow is 1500 L/min. The rotation speed is brought from 0 to 3500 rpm less than minute. At the 38<sup>th</sup> minute the rotation speed is changed from 3500 to 4500 rpm. After 13 minutes a rapid increase of hot spot temperature starts, which is at the 51<sup>st</sup> minute. After the 52<sup>nd</sup> minute the rotation speed is reduced to zero within few seconds. Before the speed increase from 3500 to 4500 rpm the highest measured winding temperature is 117°C. Before the failure the highest measured winding temperature is 134°C, which is at the outlet side. At the inlet side this winding temperature is 106°C. At the failure the maximum of 326°C is reached at the outlet side and 203°C at the inlet side. The hot spot temperature development is characterized by three slopes: 1) 17.7°C during 22 seconds, 2) 55°C during 25 seconds and 3) 89°C during 20 seconds at the outlet side. Relatively slow response of the third stage is measured from the inlet side: 7°C, while the first stage has considerably steeper temperature increase of 33°C over the same period.

Figure 7.14 show the temperature measurements including the event of failure. Figure 7.15 shows the measurement data from power analyzer including torque and current for the whole run and Figure 7.16 focuses more on the failure. Figure 7.17 shows the outcome of the failure – overheated outlet side of the winding.

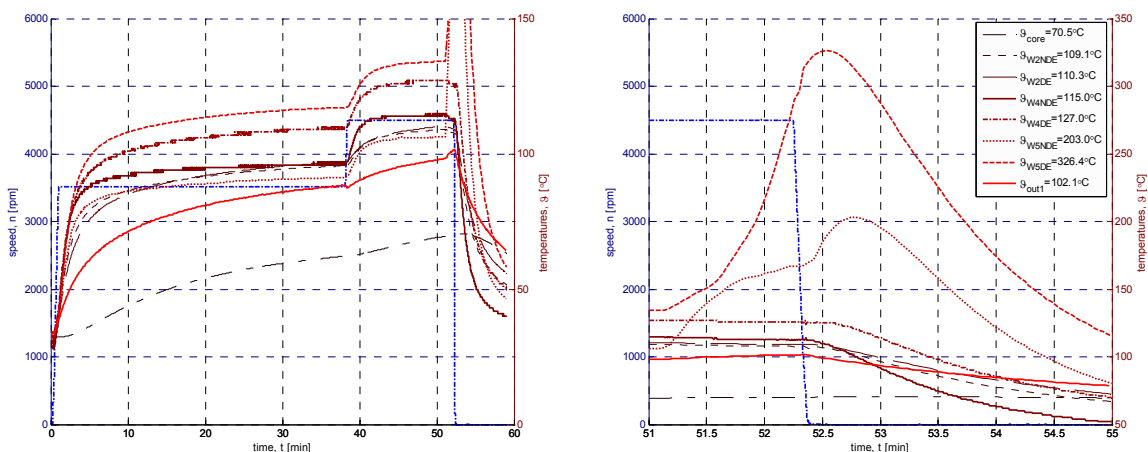


Figure 7.14 Temperature logs of load test together with detailed view on overheating

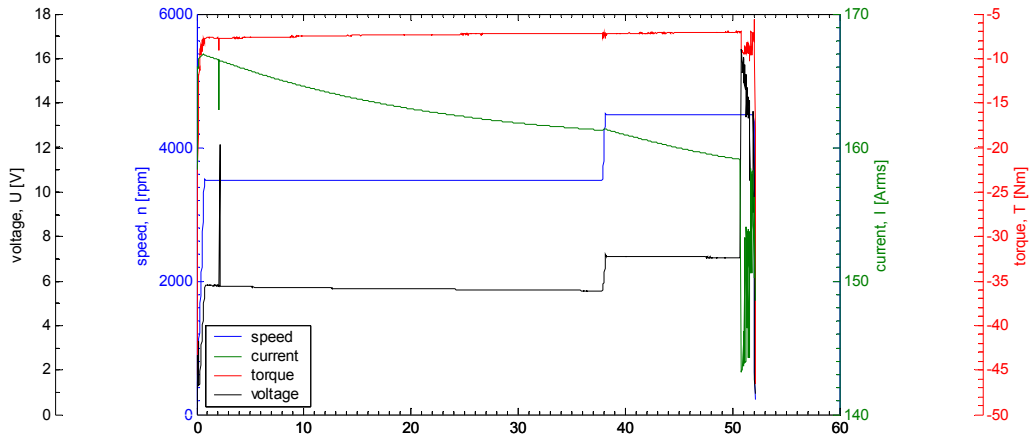


Figure 7.15 Data records from the other source showing the speed, voltage, current and torque of the second run.

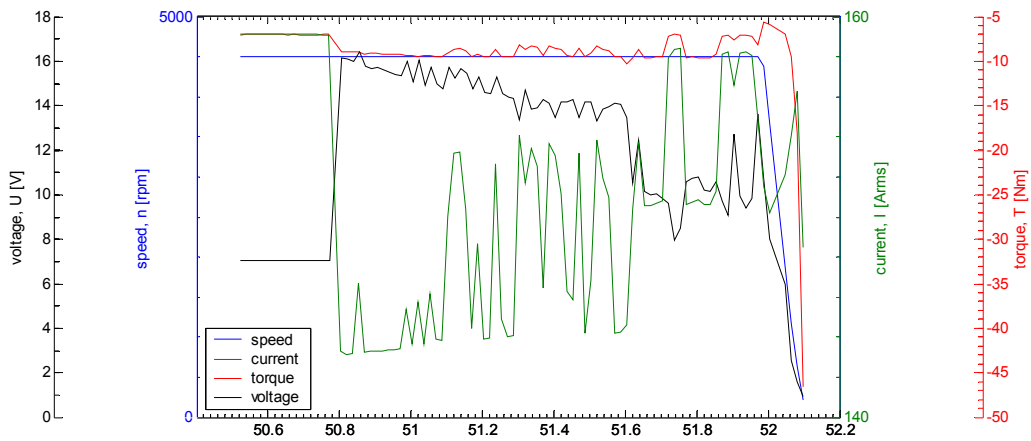


Figure 7.16 Detailed view on data records from the other source showing the speed, voltage, current and torque of the failure.

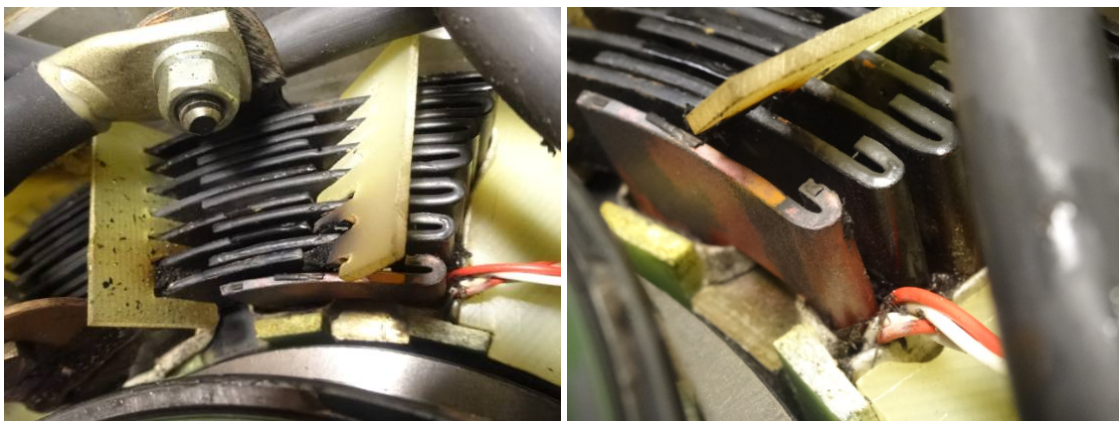


Figure 7.17 Overheated winding (W5) end (NDE or TE)

### Power loss analysis

The power losses of the short circuit tests are

- 1505 rpm, first run first half time range  $t=[25\ 70]$  min, load torque  $T=[10.24\ 10.09]$  Nm, power losses  $P=[1614\ 1590]$  W
- 2505 rpm, first run second half time range  $t=[2.5\ 31.5]$  min, load torque  $T=[7.96\ 7.87]$  Nm, power losses  $P=[2087\ 2065]$  W

- 3505 rpm, first run second half time range  $t=[34\ 59]$  min, load torque  $T=[7.38\ 6.94]$  Nm, power losses  $P=[2694\ 2547]$  W
- 3515 rpm, second run time range  $t=[3\ 37]$  min, load torque  $T=[7.67\ 7.12]$  Nm, power losses  $P=[2823\ 2621]$  W
- 4505 rpm, second run time range  $t=[38\ 50]$  min, load torque  $T=[7.20\ 6.96]$  Nm, power losses  $P=[3397\ 3283]$  W

The expected power losses in the winding (120°C) and the core of the short-circuited machine are

- 1500 rpm, losses in the winding  $P_{win}=882$  W, losses in the core  $P_{core}=117$  W
- 3000 rpm, losses in the winding  $P_{win}=1587$  W, losses in the core  $P_{core}=298$  W

Once again the comparison of the measured power losses in the core is considerably larger than the expected. The estimation covers only core losses and the induced losses in the windings due to rotation. There is just active part (200 mm) and not the actual (236 mm) of the winding included in this estimation. The power loss estimation does not cover induced losses in the stator housing, yoke gap surfaces or in the core due to misalignment of laminations between the different segments. The influence of the global surface short circuit on the tooth surface of the lateral core segments is not considered either. Apart from that the electromagnetic losses in the rotor, mechanical losses in the bearings and air-drag are not included in the power loss analysis.

## 8 Summary

The advantage of conducting sheet gives a great possibility of simple production of direct air cooled coils with high mechanical and assembling tolerances. The success of the (thermal) design and production process are based on

- The comprehensive knowledge of sheet forming; cutting, folding and bending so that the high mechanical tolerances can be guaranteed
- Right winding layout that gives manageable amount of extra power losses due to proximity and eddy current effects
- The advantage of constant thickness of conducting sheet should not be violated by introducing large variation on conductor cross-section area or cooling surface that directly dash the illusion of super cooling and replaces it with super heating
- Conducting strips of laminated windings are in series and cooling channels in parallel. The coolant flow design within the cooling channel is as vital as the cooling supply system. Once again lack of cooling is overheating.
- Last not least good electric insulation is the basics for the endurance

The objective of the work, which is the design goal for the electrical machines, is that limited space and high torque requirement leads towards more external forced cooling which is directly applied to the main heat sources of an electrical machine. Basically the electrical machines could be either more compact or/and powerful with direct cooled windings where the functionality of heat exchanger is tightly connected to the functionality and reliability that machine windings are requested. The working prototype that targets a heavy hybrid vehicle demonstrates

- The concern of excessive AC losses due to alternating leakage field in the slot or rotating field exposed from the slot opening – the solution here is correct orientation of the laminated windings and the other options are not mentioned in this document
- The apprehension of the direct cooling capability and leakage of coolant that passes by the hot regions – it is considered that the infra red imaging is the most practical way to adjust the structures and cooling flows according to the actual need. Theoretically the cooling intensity – flow speed per cooling surface is adjusted so that the outcome of the heat convection and conduction results the lowest hot spot temperature for the specified flow rate and current.
- Machine windings are tested in the range of 5-250 Arms and confirm nonlinearity of torque due to reduced tooth width. The actual limit for the current is directly not the thermal loads rather than failure due to insufficient AC insulation design.
- Thermal test has been extended to thermal steady state or failure. The course of event for the failure is not analyzed in this document.
- Expectedly high no load losses due to overloaded core, yoke gaps & zig-zag laminations, irregular LF coils etc. For example the course of the design has the range of tooth width in order to meet the manufacturing requirements  $W_{th} = \{16, 14, 13.25\}$  which influences the relative flux density in the core  $B^* = \{1, 1.14, 1.2\}$  and results considerably higher power losses in the core  $P_{core} = \{1, 1.97, 2.56\}$ . The power loss analysis is rather intriguing as a few details related to the manufacturing is included in the analysis but most of them are excluded. Also the effect that 6 teeth out of 18 are narrower – 13.25 instead of 14.0 mm.

## References

- [1] Högmark, C., Reinap, A., Frogner, K., Alaküla, M. (2012), "Laminated winding with rapid cooling capability for electrical machines". *International Conference for Inductive and Electromagnetic Components, Systems and Devices including Manufacturing and Processing (INDUCTICA 2012)*, Berlin, Germany, June 26-28, 2012.
- [2] Högmark, C., Andersson, R., Reinap, A., Alaküla, M. (2012), "Electrical Machines with Laminated Winding for Hybrid Vehicle Applications". *International Electric Drives Production Conference and Exhibition (EDPC2012)*, Nuremberg, Germany, Oct. 16-17, 2012
- [3] Andersson, R., Högmark, C., Reinap, A., Alaküla, M. (2012), "Modular Three-phase Machines with Laminated Winding for Hybrid Vehicle Applications". *International Electric Drives Production Conference and Exhibition (EDPC2012)*, Nuremberg, Germany, Oct. 16-17, 2012.
- [4] Kjellstrand R., Akujärvi V. (2013), Modeling and evaluation of laminated windings. TEIE-5311,
- [5] Conny Högmark (2013), *Moulded Electrical Machines and Laminated Windings*, TEIE-1066
- [6] Reinap, A., Marquez-Fernandez, F.J., Andersson, R., Högmark, C., Alaküla, M., Göransson, A. (2014), "Heat transfer analysis of a traction machine with directly cooled laminated windings". *4th International Electric Drives Production Conference and Exhibition (EDPC2014)*, Nuremberg, Germany, 30 Sept. - 1 Oct., 2014.
- [7] Francisco J. Marquez-Fernandez (2014), *Electric Traction Machine Design for an E-RWD Unit*, TEIE-1072
- [8] Reinap, A., Högmark, C., Frogner, K., Lundström, F., Andersson, M., Alaküla, M., Wang, L., (2015), "Electrical Machine Design with Directly Cooled Laminated Fractional Pitch Windings". *5th International Electric Drives Production Conference and Exhibition (EDPC2015)*, Nuremberg, Germany, 15-16 September, 2015
- [9] B. Sundén, Introduction to Heat Transfer. Studentlitteratur Lund, 2008.
- [10] R. Shah, "Thermal entry length solutions for the circular tube and parallel plates," Proc. 3rd National Heat Mass Transfer Conference, Indian Inst. Technology Bombay, vol. Vol. 1, no. HMT-11-75, 1975.